Doklady Physics, Vol. 50, No. 11, 2005, pp. 553–555. Translated from Doklady Akademii Nauk, Vol. 405, No. 1, 2005, pp. 39–41.

PHYSICS

Effect of Pressure on the Polymorphic Transitions in Iron

N. N. Sirota, N. A. Konoplin, and T. M. Soshnina

Presented by Academician O.A. Bannykh June 10, 2005

Received June 14, 2005

We have considered the effect of pressure on the polymorphic α–γ and γ–δ transitions in iron under the assumption that each structural modification is a Debye solid with the characteristic temperature linearly increasing with the pressure and independent of the temperature. As is known, the pressure significantly influences the polymorphism in iron. At normal pressure, iron exists in three polymorphic (allotropic) modifications. The α-Fe polymorph that is stable in the range of low temperatures below 1189 K has a bcc structure and exhibits ferromagnetic behavior below 1043 K. The γ-Fe polymorph having an fcc structure is stable in the temperature interval from 1189 to 1665 K. In the interval from 1665 K to the melting point (1809 K), the bcc δ-Fe modification isomorphic to the α-Fe modifications is stable. Both γ- and δ-Fe polymorphs are paramagnetic.

The Debye temperatures of α-, γ-, and δ-Fe. The characteristic temperature of α-Fe was calculated using the average velocity of sound in this crystal. According to the paper by Alers in monograph [1], the Debye temperature can be expressed as

$$\Theta = \frac{2}{\pi}\frac{h}{k}\left(\frac{9N}{4\pi}\right)^{1/3} V^{-1/3} c, \qquad (1)$$

where $2/\pi$ is a factor taking into account the dispersion, h is the Planck constant, k is the Boltzmann constant, N is the Avogadro number, V is the molar volume, and c is the average velocity of sound.

According to the paper by Anderson in monograph [1], the average sound velocity is given by the formula

$$c = \left[\frac{1}{3}\left(\frac{2}{v_S^3} + \frac{1}{v_l^3}\right)\right]^{-1/3}, \qquad (2)$$

where

$$v_S = \sqrt{\frac{G}{\rho}} \qquad (3)$$

is the transverse velocity of sound,

$$v_l = \sqrt{\frac{K + \frac{4}{3}G}{\rho}} \qquad (4)$$

is the longitudinal velocity of sound, K is the bulk modulus, G is the shear modulus, and ρ is the density.

The shear modulus G was calculated using formula (4) for the experimental value of v_l (determined by linear extrapolation to the normal pressure) [2], the density ρ determined for a molar volume of V_0 = 7.0938 cm^3/mol [3], and the known bulk modulus K. For v_l = 5899 m/s, ρ = 7874 kg/m^3, and K = 172 GPa [4], this formula yields G = 76.5 GPa, which agrees with the published data [1, 5]. The average sound velocity calculated using Eqs. (2)–(4) is c = 3484 m/s. The characteristic temperature of α-Fe calculated by substituting this average sound velocity into formula (1) is Θ_α = 419 K, which is close to the values reported in [6, 7].

The characteristic temperature of γ-Fe at normal pressure was taken as equal to Θ_γ = 335 K [6].

The characteristic temperature of δ-Fe was estimated using the Helmholtz free energy of this polymorph at a temperature of the γ–δ transition. In order to determine this quantity, we first calculated the Helmholtz free energy of γ-Fe at $T_{\gamma-\delta}$ = 1665 K using the corresponding characteristic temperature at normal pressure. The sum of this value and the enthalpy of the γ–δ transition ($\Delta H_{\gamma-\delta}$ = 980 J/mol, which corresponds to the average of the data reported in [8, 9]) gives the Helmholtz free energy of δ-Fe at the transition temperature and normal pressure. Using this value, the characteristic temperature of δ-Fe was estimated in the Debye approximation by assuming that the differences of heat capacities at constant pressure and constant volume, $C_p - C_V$, for γ and δ polymorphs are the same and that the $\Delta H_{\gamma-\delta}$ value corresponds to the temperature-independent part of the difference of internal energies $\Delta U^0_{\gamma-\delta}$. This calculation yields Θ_δ = 328.3 K.

Moscow State University of Applied Ecology, Moscow, Russia

1028-3358/05/5011-0553$26.00

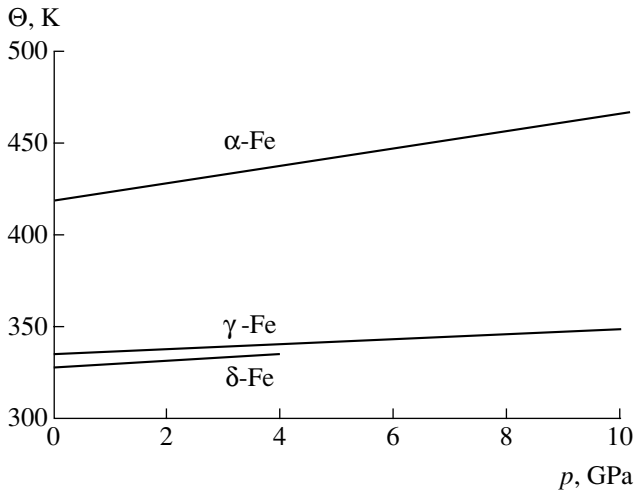

Fig. 1. Plots of the characteristic temperatures of α-, γ-, and δ-Fe polymorphs versus pressure.

Alternatively, the characteristic temperature of δ-Fe was estimated using the Lindemann method, according to which

$$\Theta = \frac{\eta}{d}\sqrt{\frac{T_m}{A}}, \qquad (5)$$

where T_m is the melting temperature; A is the atomic weight (for iron, (A = 55.847); d is the minimum interatomic distance at the melting temperature; and η is a numerical coefficient. According to [10], the lattice parameter of iron at T_m = 1807 K is α = 2.9411 Å, which yields for a bcc iron structure $d = \frac{\sqrt{3}a}{2}$ = 2.5471 Å. Adopting the value of η = 165 [11], we obtain the characteristic temperature Θ_δ = 368 K. However, no polymorphic transition is observed at this temperature (the free energy curves of γ-Fe and δ-Fe do not intersect). Assuming that the transition temperature $T_{\gamma-\delta}$ = 1665 K corresponds to Θ_δ = 328.3 K, we obtain an estimate of η = 147.

The effect of pressure on the Debye temperatures of iron polymorphs. The influence of pressure p on the characteristic temperature Θ for α-Fe was determined using the pressure dependences of the bulk modulus K and the shear modulus G. In the interval of pressures under consideration, these dependences can be approximated by linear functions as [12]

$$K = K_0 + kp, \quad G = G_0 + gp,$$

where K_0, G_0 are the values of the moduli at normal pressure and k, g are the pressure-independent coefficients. The calculations were performed using K_0 and k values corresponding to the data reported in [3, 4]. The coefficient $g = \frac{\partial G}{\partial p}$ was estimated using formula (4) for the experimentally determined values of the longitudinal sound velocity at various pressures [2], the bulk modulus K, and the density ρ. The corresponding values of ρ(p) were determined from the experimental data on the change in the molar volume of α-Fe as a function of the pressure [3]. These calculations yield g = 1.97. The calculated curve of the characteristic temperature of α-Fe versus pressure is presented in Fig. 1. The Debye temperature Θ_α exhibits linear growth with the pressure at a slope of $\frac{\partial\Theta}{\partial p}$ = 4.89 K/GPa.

Söderlind *et al.* [13] calculated the characteristic temperature of γ-Fe as a function of the molar volume. Using these data and taking into account the pressure-induced change in the molar volume of γ-Fe at 300 K [12], we obtained the Θ(p) curve depicted in Fig. 1. In the range of pressures under consideration, this dependence can also be approximated by a linear function. According to this, the Debye temperature Θ_γ exhibits linear growth with the pressure at a slope of $\frac{\partial\Theta}{\partial p}$ = 1.38 K/GPa. Thus, the slope of Θ(p) for γ-Fe is significantly lower than that for α-Fe.

Using the pressure dependences of the characteristic temperatures of α-Fe and γ-Fe, we have determined the temperatures of the α–γ polymorphic transition at various pressures. The temperature of the polymorphic transition corresponds to the point of intersection of the curves of Helmholtz free energies of the corresponding phases, including the temperature-independent part of the difference of internal energies at a given pressure. Using this definition, we have determined the temperature dependence of the Helmholtz free energy corresponding to the Debye temperature at each pressure. These curves were shifted relative to each other by a value corresponding to the difference of internal energies of α-Fe and γ-Fe at a given pressure:

$$\Delta U_{\alpha-\gamma} = \Delta U^0_{\alpha-\gamma} + p(V_\gamma - V_\alpha),$$

where $\Delta U^0_{\alpha-\gamma}$ = 5912 J/mol [8] is the difference of internal energies at normal pressure and T = 0 K. In the range of pressures under consideration, the difference of molar volumes $V_\gamma - V_\alpha$ can be considered as pressure-independent and as equal to the value of this difference at normal pressure and T = 0 K. The latter value was determined via extrapolation of the experimental temperature dependence $V(T)$ [10], which yielded $V_\gamma - V_\alpha = 0.159 \times 10^{-6}$ m^3/mol.

Figure 2 (lower curve) shows the dependence of the temperature of the α–γ polymorphic transition on the pressure, calculated as described above, in comparison with the experimentally determined values of $T_{\alpha-\gamma}$

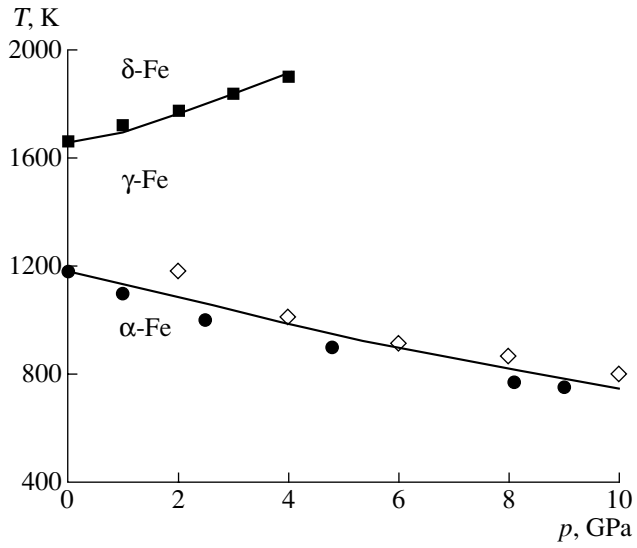

Fig. 2. Plots of the temperatures of the α–γ and γ–δ polymorphic transition in iron versus pressure. Solid curves show the results of calculations (this study) and symbols represent the experimental data: (◇) dynamic pressure [14]; (●) static pressure [14]; (■) generalized data [15].

(points). As can be seen, the theoretical and experimental data are in good agreement.

An analogous calculation of the polymorphic transition temperature as a function of the pressure was performed for the transition from γ-Fe to δ-Fe. Using the adopted pressure dependence of the characteristic temperature of the γ-Fe polymorph, we have determined the Helmholtz free energy of γ-Fe at $p = 4$ GPa. Using this value and the transition temperature $T_{\gamma-\delta} = 1900$ K and taking into account the relation

$$\Delta U_{\gamma-\delta} = \Delta U^0_{\gamma-\delta} + p(V_\delta - V_\gamma),$$

we calculated the Helmholtz free energy of δ-Fe and determined the characteristic temperature $\Theta_\delta = 335.3$ K in the Debye approximation. In these calculations, it was assumed that the difference of molar volumes of the γ-Fe and δ-Fe polymorphs is independent of the pressure in the range under consideration and is equal to the value at normal pressure and $T = 0$ K, which was estimated as $V_\delta - V_\gamma = -0.04 \times 10^{-6}$ m^3/mol [10, 12]. Then, taking into account that $\Theta_\delta = 328.3$ K at normal pressure, we obtained the $\Theta_\delta(p)$ curve depicted in Fig. 1. In the range of pressures under consideration, the Debye temperature Θ_δ exhibits linear growth at a slope of

$$\frac{\partial \Theta}{\partial p} = 1.75 \text{ K/GPa}.$$

Figure 2 (upper curve) shows a plot of the temperature of the γ–δ polymorphic transition versus pressure, calculated as described above, in comparison with the experimentally determined values of $T_{\gamma-\delta}$ (points).

The calculated curves of the α–γ and γ–δ polymorphic transitions in iron practically coincide with the experimental phase diagram and are close to the values calculated using the Clausius–Clapeyron equation.

In conclusion, we have established that the characteristic temperatures of α-, γ-, and δ-Fe polymorphs exhibit linear dependences on the pressure. We have also calculated the lines of α–γ and γ–δ phase equilibria on the *p–T* diagram, proceeding from the equilibrium conditions calculated in the Debye approximation from the values of the characteristic temperatures of α-, γ-, and δ-Fe. The results of the calculations are in good agreement with the experimental phase diagram of iron.

REFERENCES

1. *Physical Acoustics: Principles and Methods*, Ed. by W. Mason (Academic, New York, 1964), Vol. 2.
2. G. Fiquet, J. Badro, F. Guyot, *et al.*, Science **291**, 468 (2001).
3. A. P. Jephcoat, H. K. Mao, and P. M. Bell, J. Geophys. Res. **91** (5), 4677 (1986).
4. L. Stixrude, R. E. Cohen, and D. J. Singh, Phys. Rev. **50** (9), 6442 (1994).
5. *Handbook of Physical Quantities*, Ed. by I. S. Grigoriev and E. Z. Meilikhov (Énergoatomizdat, Moscow, 1991; CRC, Boca Raton, 1997).
6. R. J. Weiss and K. J. Tauer, Phys. Rev. **102** (6), 1490 (1956).
7. B. N. Brockhouse, H. E. Abou-Hetal, and E. D. Hallman, Solid State Commun. **5**, 211 (1967).
8. B. M. Mogutnov, I. A. Tomilin, and L. A. Shvartsman, *Thermodynamics of Ferricarbonic Alloys* (Metallurgiya, Moscow, 1972) [in Russian].
9. P. D. Desai, J. Phys. Chem. Ref. Data **15** (3), 967 (1986).
10. Z. S. Basinski, W. Hume-Rothery, and A. L. Sutton, Proc. R. Soc. London **229**, 459 (1955).
11. L. Kaufman, E. V. Clougherty, and R. J. Weiss, Acta Metall. **11**, 323 (1963).
12. J. M. Besson and M. Nicol, J. Geophys. Res. **95** (13), 21717 (1990).
13. P. Söderlind, J. A. Moriarty, and J. M. Wills, Phys. Rev. B **53** (21), 14063 (1996).
14. Landolt-Börnstein, *Magnetic Properties of Metals. New Series*, Ed. by H. P. J. Wijn (Springer, Berlin, 1994), Vol. 3-19il.
15. E. Yu. Tonkov, *Phase Diagrams of Elements at High Pressure* (Nauka, Moscow, 1979) [in Russian].

Translated by P. Pozdeev

Doklady Physics, Vol. 50, No. 11, 2005, pp. 556–559. Translated from Doklady Akademii Nauk, Vol. 405, No. 1, 2005, pp. 42–45.

PHYSICS

Speed of Sound in Water Near the Temperature of the Maximum Density

P. P. Sherstyankin[a], Yu. F. Tarasyuk[b], L. G. Kolotilo[c], V. G. Ivanov[a], L. N. Kuimova[a], and V. I. Babiĭ[c]

Presented by Academician K.Ya. Kondrat'ev December 27, 2004

Received January 17, 2005

The temperature T_{md} equal to 4°C, which corresponds to the maximum density of water (the temperature of the maximum density), is its anomalous property and, thereby, holds theoretical and applied interest in the investigation of other thermodynamic parameters of water, e.g., the speed of sound *C*. This problem is urgent for deep fresh reservoirs located at intermediate and high latitudes, including Baĭkal, the deepest lake in the world (depth up to 1642 m) [1].

The goal of the present study is the analysis of variations in the behavior of the speed of sound *C* near the temperature T_{md} on the basis of experimental data related to lake Baĭkal.

The method of investigation employs both theoretical and experimental approaches and exploits the Chen–Millero equation of state [2] for lake waters.

We theoretically analyze the speed of sound in terms of independent variables *T*, *S*, *P* (*T* [°C] is temperature; *S* [g kg^{-1}] is salinity; and *P* [bar] is pressure). Based on formulas taken from [3] for thermodynamic parameters of water, we arrive at the following expression for the speed of sound:

$$C = \frac{1}{\sqrt{\rho\gamma_{ad}}} = \frac{1}{\sqrt{\rho(\gamma_{isoth} - \alpha\Gamma)}} = \frac{1}{\sqrt{\rho_P - \rho\alpha\Gamma}}. \quad (1)$$

Here, ρ is the density of water, $\gamma_{ad} = \frac{1}{\rho}(\rho_P)_{ad}$ is the adiabatic-compressibility coefficient, $\gamma_{isoth} = \frac{1}{\rho}(\rho_P)_{T,S}$ is the isothermal-compressibility coefficient, ρ_P is the derivative of the water density with respect to pressure at a constant temperature *T* and salinity *S*, α is the thermal-expansion coefficient, and Γ is the adiabatic gradient. The last quantity is calculated from the expression

$$\Gamma = -\frac{T^K\rho_T}{Q_P\rho^2} = \frac{T^K\alpha}{Q_P\rho}, \quad (2)$$

where T^K is temperature expressed in absolute degrees, $\alpha = -\frac{\rho_T}{\rho}$, ρ_T is the derivative of the water density ρ with respect to temperature *T* at the constant salinity *S* and pressure *P*, and Q_P is the specific heat at the constant pressure *P*. All the parameters of formula (1) are functions of *T*, *S*, and *P*, but we do not indicate this fact for the sake of simplicity.

Formula (1) is identical to the ratio (4) of [4] for the speed of sound. However, the form of (1), which was proposed by us, makes it possible to more obviously represent the dependence of the speed of sound on the parameters α and Γ determining the adiabatic properties of water.

Using formula (1), we can analyze the variation of the speed of sound in the vicinity of the temperature of the maximum density T_{md}. We can see that, firstly, as follows from [3–5], at the temperature of the maximum density, the water density ρ has the maximum, whereas the parameters α and Γ attain the zero value. In this case, the values of α and Γ are positive or negative as $T > T_{md}$ or $T \le T_{md}$, respectively, the product $\alpha\rho\Gamma$ always exceeding zero. Thus, insofar as at T_{md} all the parameters determining the speed of sound attain their maxima and stand in the denominator of formula (1) (under the square-root sign), the value of speed of sound *C* must have the minimum (i.e., be minimal).

Assuming that T_{md} (Table 1), we consider the behavior of the speed of sound *C* near the temperature of the maximum density T_{md} for temperatures from 0 to 8°C and pressures from 0 to 180 bar. The maximum diver-

[a] *Institute of Limnology, Siberian Division, Russian Academy of Sciences, P. O. Box 4199, Irkutsk, 664033 Russia*
e-mail: ppsherst@lin.irk.ru
[b] *Laboratory for Simulating Complex Systems, Universitetskaya nab. 5, St. Petersburg, Russia*
[c] *Marine Hydrophysical Institute, National Academy of Sciences of Ukraine, Sevastopol, 99011 Ukraine*

1028-3358/05/5011-0556$26.00

Table 1. The speed of sound near the temperature of the maximum density T_{md} within the pressure range P from 0 to 180 bar at the average salinity $S = 0.096$ g kg^{-1} in Lake Baĭkal

P, bar	C, m s^{-1}								
	0°C	1°C	2°C	3°C	4°C	5°C	6°C	7°C	8°C
0.00	1402.509	1407.475	1412.330	1417.076	**1421.715**	1426.247	1430.675	1435.000	1439.222
47.47	1410.022	1415.016	1419.897	**1424.668**	1429.330	1433.884	1438.332	1442.676	1446.917
95.09	1417.613	1422.632	**1427.537**	1432.330	1437.012	1441.585	1446.052	1450.412	1454.670
141.14	1425.006	**1430.046**	1434.971	1439.782	1444.481	1449.071	1453.552	1457.928	1462.199
180.00	**1431.283**	1436.339	1441.278	1446.103	1450.815	1455.416	1459.909	1464.296	1468.577

Note: Values of $C(T_{md}, S, P)$ are indicated by bold-type numbers.

gences of values of C from the data of [3] and [6] are 0.245 m s^{-1} ($T = 3$°C, $P = 180$ bar) and 0.208 m s^{-1} ($T =$ 0–1°C, $P = 150$ bar), respectively, and do not exceed 0.20 m s^{-1} as compared to the experimental data of [7]. The use of the expression for the speed of sound in the form of (1), where the dependence of C on the coefficients of the thermal expansion α and the adiabatic gradient Γ is explicitly shown, essentially increases the potential of the investigations.

Marked features in the behavior of the speed of sound near the temperature of the maximum density within the pressure range from 0 to 180 bar are not distinguished in Table 1. However, this effect can be masked by the dependence of C on T.

We now additionally analyze the results of the application of formula (1), (2). To this end, we consider the behavior of the derivative of the function $C'_x(T, S, P)$, where the subscript x hereinafter stands for the differentiation with respect to T, S, or P in the vicinity of T_{md}. To accomplish this, we find the derivative with respect to temperature T from the speed of sound C written out in form (1). As a result, we arrive at the relationship

$$C'_T = -\frac{C^3}{2}(\rho_{TP} - \rho_T\alpha_T\Gamma - \rho\alpha_T\Gamma - \rho\alpha\Gamma_T). \quad (3)$$

At the temperature $T = T_{md}$, the last three terms equal zero, since the cofactors ρ_T, α, and Γ entering into them are close to zero. Therefore, we do not need the exact form of the derivatives for α'_T and Γ'_T. As a result, we obtain

$$C_T(T_{md}, S, P) = -\frac{C^3(T_{md}, S, P)\rho_{TP}(T_{md}, S, P)}{2}, \quad (4)$$

where $\rho_{TP} = \rho_{PT}$ is the thermal baric parameter that determines the dependence on temperature and pressure. From the analysis of formula (4) and thermal baric parameter ρ_{TP}, whose behavior as a function of temperature T and pressure P was thoroughly considered in [7–9], it follows that, in the vicinity of the point T_{md}, no singularities depending on T and P are present. This conclusion is confirmed by the values of C'_T, calculated according to formula (4) and shown in Table 2, as well as by the direct comparison of differences ΔC determined on the basis of formula (1) with a temperature step of 1°C.

As is seen from Table 1, the value of C decreases and increases with increasing temperature and pressure, respectively, which is confirmed by the data for C'_T given in Table 2.

Thus, as follows from Tables 1 and 2, evident attributes of any singularities in varying values of C as a function of T and C'_T are absent in the vicinity of the temperature of the maximum density.

We now analyze the expression standing under the radical sign in the denominator of formula (1). The product ($\rho\alpha\Gamma$) entering into formula (1) is always positive and has a minimum equal to zero at the point $T = T_{md}$ (see figure). The radicand $\rho_P - \rho\alpha\Gamma$ has a weakly pronounced maximum (see figure), which indicates the existence of a scarcely distinguishable minimum of the

Table 2. Derivative C'_T of the speed of sound with respect to temperature at the temperature of the maximum density T_{md} within the pressure range from 0 to 180 bar for the conditions in Lake Baĭkal

P, bar	S, g kg^{-1}	T_{md}, °C	α, 10^{-10} °C^{-1}	$C'_T(T_{md}, S, P)$
0.00	0.096	3.9642	3.6	4.59
47.47	0.096	3.0000	4.6	4.72
95.09	0.096	2.0000	6.6	4.85
141.14	0.096	1.0000	2.0	4.98
180.00	0.096	0.1292	8.2	5.10

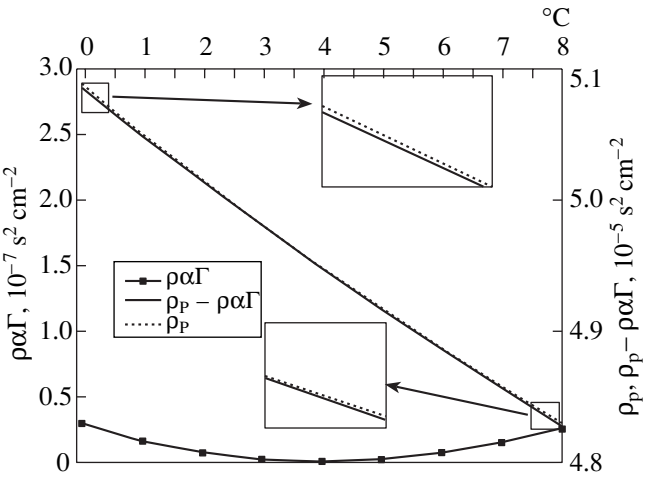

Analysis of the behavior of the terms ρ_P, $\rho_P - \rho\alpha\Gamma$, and $\rho\alpha\Gamma$, which are radicands in the denominator of formula (1) for the speed of sound in the four-degree vicinity of the temperature of the maximum density. $T_{md}(P = 0) \simeq 4$°C.

speed of sound C in the region of the temperature of the maximum density T_{md}.

At $T = T_{md}$, the speed of sound corresponding to the adiabatic regime, i.e., $C = C_{ad}$, which we usually use [see, e.g., formula (1)], becomes equal to C_{isoth} characteristic of the isothermal regime. The latter quantity is determined by the formula

$$C_{isoth} = \frac{1}{\sqrt{\rho\gamma_{isoth}}} = \frac{1}{\sqrt{\rho_P(T, S, P)}}, \quad (5)$$

where the coefficient γ_{isoth} of the isothermal compressibility stands under the quadratic-radical sign, and

$$C_{ad}(T_{md}, S, P) = C_{isoth}(T_{md}, S, P). \quad (6)$$

From the analysis of the radicand in formulas (1), (5) it follows that

$$C_{ad}(T_{md}, S, P) \geq C_{isoth}(T_{md}, S, P), \quad (7)$$

where the equality sign is realized only in the case of the validity of formula (6). In fact, if we analyze the difference between the speed of sound for the adiabatic and isothermal regimes, this difference

$$\Delta C_{ad–isoth} = C_{ad}(T_{md}, S, P) - C_{isoth}(T_{md}, S, P)$$

is zero as $T = T_{md}$.

We now consider these differences within the four-degree range in the vicinity of temperature T_{md} (see Table 3). In this table, the chosen values of pressure P (excepting the edge values) correspond to integer values of T_{md}, namely, 1, 2, and 3°C. The analysis of data given in Table 3 allows us to make the following conclusions.

(i) At $T = T_{md}$, the adiabatic regime transforms into the isothermal one.

(ii) In the adiabatic regime, values of the speed of sound are always higher than in the isothermal regime.

(iii) When the deviation of T_{md} from T is 1°C, the difference in the speed of sound attains 0.022 to 0.025 m s^{-1}, and only when this deviation is 4°C does the difference attain about 0.4 m s^{-1}. In this case, the difference increases (decreases) by approximately 10% towards lower temperatures (higher pressures).

(iv) The ratio of speeds of sound corresponding to the isothermal and adiabatic regimes has a clearly pronounced maximum.

The principal feature of the thermodynamic regime near the temperature of the maximum density T_{md} is the fact that the adiabatic properties of water are manifested almost not at all and completely disappear at $T = T_{md}$. The water medium acquires a number of unusual properties: indifferent equilibrium (or something close to it) disappears or becomes close to the point of the buoyancy-parameter disappearance (the buoyancy parameter proportional to α tends to zero); the thickness of a layer stratified by the gravity-force field is given by the expression $H = \frac{C_P}{\alpha g}$, where g is the free-fall acceleration, and tends to infinity (α tends to zero); etc.

For sea water, the method of calculating the speed of sound with allowance for the salt-ion concentration was

Table 3. Difference in the speeds of sound (C_{ad}) and (C_{isoth}) for adiabatic and isothermal regimes, respectively

P, bar	ΔC, m s^{-1}								
	0	1°C	2°C	3°C	4°C	5°C	6°C	7°C	8°C
0.00	0.4075	0.2238	0.0965	0.0229	0.0000	0.0255	0.0967	0.2115	0.3678
47.47	0.2245	0.0980	0.0241	**0.0000**	0.0233	0.0916	0.2026	0.3544	0.5450
95.09	0.0959	0.0236	**0.0000**	0.0228	0.0897	0.1985	0.3472	0.5339	0.7569
141.14	0.0231	**0.0000**	0.0223	0.0878	0.1943	0.3400	0.5230	0.7414	0.9938
180.00	0.0004	0.0166	0.0755	0.1750	0.3132	0.4883	0.6985	0.9423	1.2181

Note: For integer-valued temperatures of the maximum density, T_{md} equal to 3, 2, 1°C, the differences under study are shown by bold-type numbers.

proposed in [10]. In the case of equal water temperature and the temperature of the maximum density, the adiabatic parameter $\kappa = C_P/C_V = 1$ (C_V is the specific heat at a constant volume). The speed of sound corresponding to the adiabatic regime and defined as $C_{ad} = \sqrt{\kappa}\, C_{isoth}$ becomes equal to the speed of sound C_{isoth} corresponding to the isothermal regime, which is calculated as a function of T, S, P. The latter fact can be used for methodological purposes, e.g., for the calculation of speed of sound in the case of calibration of modern velocimeters and sensors, both existing and under development [11–15]. As was shown in [8], the statements advanced above relate both to normal atmospheric pressure ($P = 0$) and to other pressure values for which the temperature of the maximum density is attained.

Lake Baĭkal presents all the necessary conditions for realizing these investigations. Indeed, in this lake in winter depth regions regularly arise with temperatures equal to the temperature of the maximum density T_{md}, i.e., the so-called mesothermal temperature maximum (see Table 3 and the figure). In this case, the speed of sound can be calculated as a reciprocal value of the square root of the isothermal compressibility, because adiabatic effects are zero and degenerate. These results can be applied for testing hydroacoustic equipment not only in Lake Baĭkal but also under laboratory conditions or in experimental tanks. It is also of interest to carry out studies for Baĭkal thermal barriers when the temperature of the maximum density (~4°C) is established in upper water layers and occupies vast shallow waters, e.g., the mouth of the Selenga River [15].

ACKNOWLEDGMENTS

This work was supported by the Russian Foundation for Basic Research, project nos. 05-05-97242 and 05-05-64375.

REFERENCES

1. *A New Bathymetric Map of Lake Baikal, INTAS Project 99-1669 Team, October 2002*; http://allserv.ugent.be/mdbatist/intas/intas.htm.
2. P. P. Sherstyankin, V. G. Ivanov, L. N. Kuimova, *et al.*, in *Proceedings of 8th International Conference "Modern Methods and Means of Oceanology Investigations," Moscow, Russia, 2003* (Moscow, 2003), Part 1, pp. 265–273.
3. C.-T. A. Chen and F. J. Millero, Limnol. Oceanogr. **31**, 657 (1986).
4. V. M. Kamenkovich, *Fundamentals of the Ocean Dynamics* (Gidrometeoizdat, Leningrad, 1973) [in Russian].
5. H. Eklund, Science **142** (3598), 1457 (1963).
6. P. P. Sherstyankin, L. G. Kolotilo, Yu. F. Tarasyuk, *et al.*, Dokl. Akad. Nauk **386** (1), 103 (2002).
7. A. G. Chenskii *et al.*, in *Acoustic of Ocean* (Geos, Moscow, 1998), pp. 377–347 [in Russian].
8. P. P. Sherstyankin and L. N. Kuimova, Dokl. Akad. Nauk **391** (2), 254 (2003).
9. P. P. Sherstyankin, L. N. Kuimova, and V. L. Potemkin, Dokl. Akad. Nauk **375**, 107 (2000).
10. D. A. Denisov, A. V. Abramov, and E. P. Abramova, Akust. Zh. **48**, 498 (2003) [Acoust. Phys. **48**, 413 (2003)].
11. V. A. Komlyakov, *Naval Means of Sound Velocity Measuring and Modeling of Acoustic Fields in the Ocean* (Nauka, St. Petersburg, 2003) [in Russian].
12. V. A. Komlyakov, Sudostroenie, No. 5, 35 (2002).
13. V. I. Babiĭ, Sudostroenie, No. 4, 31 (2003).
14. V. I. Babiĭ, Morsk. Vestn., No. 4, 39 (2003).
15. P. P. Sherstyankin, in *Elements of Hydrometeorological Regime of Lake Baikal* (Nauka, Leningrad, 1965), pp. 29–37 [in Russian].

Translated by G. Merzon

Doklady Physics, Vol. 50, No. 11, 2005, pp. 560–564. Translated from Doklady Akademii Nauk, Vol. 405, No. 2, 2005, pp. 184–187.

PHYSICS

Meler–Fock Transformations in Problems of Wave Diffraction on Unclosed Structures in the Time Region

V. A. Doroshenko[a], V. F. Kravchenko[b], and Corresponding Member of the RAS V. I. Pustovoĭt[c]

Received June 6, 2005

INTRODUCTION

Based on concepts developed in [1, 2], we have applied for the first time the Kontorovich–Lebedev integral transformation to solve the first and second boundary value problems for Helmholtz equations with the three-dimensional unclosed biconic geometry. This has allowed us to lower the dimension of the equations and to obtain the solution of the electrodynamic problem in the frequency region [3]. In the present paper, we propose and substantiate a novel method for solving boundary value problems for the wave equation in wedge-like and conic regions. The method is based on the use of the Meler–Fock transformation [4] combined with the method of singular integral equations of pair summator equations [5]. The employment of this transformation to solving boundary value electrodynamic problems in the time region for unclosed conic structures makes it possible to find an analytical solution and to perform the qualitative analysis of their scattering properties.

FORMULATION OF THE PROBLEM

We consider the problem of wave diffraction on an unbounded thin conic structure Σ consisting of two cones Σ_1 and Σ_2 $\left(\Sigma = \bigcup_{j=1}^{2} \Sigma_j\right)$ with a common vertex and axis, opening angles $2\gamma_j$, and with N slots periodically cut along the generatrices and having the angular width d_j ($j = 1, 2$), respectively (Fig. 1). The structure period is $l = \frac{2\pi}{N}$, and d_j are the values of dihedral angles formed by the intersection of planes that contain the cone axis and slot edges. There is also a point field source located at the point $M_0(\mathbf{r}_0)$. The field generated by the source varies in accordance with a law given by the function $f(t - t_0)$ (the source is switched on at the time instant t_0). We now introduce the spherical coordinate system r, θ, φ with the origin at the vertex of the conic structure. In this system, each of the cones is determined by the equation Σ_j: $\theta = \gamma_j$. It is necessary to determine the potential $\upsilon^{(\chi)}(\mathbf{r}, t)$ that satisfies at every instant of time the following conditions:

the wave equation

$$\left(\Delta - \frac{1}{a^2}\frac{\partial^2}{\partial t^2}\right)\upsilon^{(\chi)}(\mathbf{r}, t) = -\widehat{F}^{(\chi)}(\mathbf{r}, t), \quad \mathbf{r} \notin \Sigma, \ \mathbf{r}_0, \qquad \widehat{F}^{(\chi)}(\mathbf{r}, t) = \frac{b^{(\chi)}}{r}\delta(\mathbf{r} - \mathbf{r}_0) f(t - t_0); \tag{1}$$

the initial condition

$$\upsilon^{(\chi)} \equiv 0 \equiv \frac{\partial \upsilon^{(\chi)}}{\partial t}, \quad t \le t_0; \tag{2}$$

the boundary condition

$$\frac{\partial^{\chi-1}}{\partial n^{\chi-1}}\left(\frac{\partial \upsilon^{(\chi)}}{\partial t}\right)\Big|_{\Sigma} = 0; \tag{3}$$

the bounded-energy condition

$$\iiint_V \left(\left|\frac{\partial \upsilon^{(\chi)}}{\partial t}\right|^2 + \left|\nabla \upsilon^{(\chi)}\right|^2\right) dV < \infty. \tag{4}$$

Here, the superscript $\chi = 1, 2$ determines the type of the source surface. According to [6, 7], the boundary value problem given by Eqs. (1)–(4) has a unique solution. We represent the potential $\upsilon^{(\chi)}(\mathbf{r}, t)$ as

$$\upsilon^{(\chi)}(\mathbf{r}, t) = \upsilon_0^{(\chi)}(\mathbf{r}, t) + \upsilon_1^{(\chi)}(\mathbf{r}, t),$$

[a] *Kharkov National University of Radio Electronics, Kharkov, 61166 Ukraine*

[b] *Institute of Radio Engineering and Electronics, Russian Academy of Sciences, ul. Mokhovaya 11-7, Moscow, 125009 Russia*

[c] *Central Design Bureau for Unique Instrumentation, Russian Academy of Sciences, ul. Butlerova 15, Moscow, 117342 Russia*

1028-3358/05/5011-0560$26.00

where

$$\upsilon_0^{(\chi)} = -\frac{b^{(\chi)}}{4\pi r_0 R} f\left(t - t_0 - \frac{1}{a}R\right)\eta\left(t - t_0 - \frac{1}{a}R\right).$$

The source potential $\upsilon_1^{(\chi)}(\mathbf{r}, t)$ is the desired Debye potential that corresponds to the field excited by the source, $\eta(\xi)$ is the Heaviside step function, and $R = |\mathbf{r} - \mathbf{r}_0|$.

GREEN's FUNCTION AND THE MELER–FOCK INTEGRAL TRANSFORMATIONS

We express the potential $\upsilon^{(\chi)}(\mathbf{r}, t)$ in terms of the Green's function and use it to solve the boundary value problem given by Eqs. (1)–(4):

$$\upsilon^{(\chi)}(\mathbf{r}, t) = \frac{b^{(\chi)}}{r_0}\int_0^{t-t_0} G^{(\chi)}(\mathbf{r} - \mathbf{r}_0, z) f(t - t_0 - z)dz. \quad (5)$$

The Green's function is

$$G^{(\chi)}(\mathbf{r}, t) = G_0(\mathbf{r}, t) + G_1^{(\chi)}(\mathbf{r}, t), \quad (6)$$

where

$$G_0(\mathbf{r}, t) = \frac{\delta\left[t - t_0 - \frac{R}{a}\right]}{4\pi R}$$

is the Green's function of the free space, satisfying wave equation (1) having the δ-shaped right-hand side, initial condition (2), boundary condition (3), and boundedness condition (4). We seek the potential $\upsilon_1^{(\chi)}(\mathbf{r}, t)$ in the form of (5), whereas the initial problem is reduced to finding the function $G_1^{(\chi)}(\mathbf{r}, t)$ for the complicated conic structure Σ. To this end, we use the Laplace transformation for the function $G^{(\chi)}(\mathbf{r}, t)$ with respect to the time parameter

$$G^{s,(1)} = G^{s,(1)}(\mathbf{r}) = \int_0^{+\infty} G^{(1)}(\mathbf{r}, t)e^{-st}dt, \quad \mathrm{Re}\, s > 0. \quad (7)$$

We find the image $G^{s,(1)}$ that must satisfy the following requirements:

the inhomogeneous Helmholtz equation

$$(\Delta - q^2)G^{s,(\chi)}(\mathbf{r}) = -e^{-st_0}\delta(\mathbf{r} - \mathbf{r}_0), \quad \mathbf{r} \notin \Sigma_0, \quad \mathbf{r}_0, \quad q = \frac{s}{a}; \quad (8)$$

the boundary condition

$$\frac{\partial^{\chi-1}}{\partial n^{\chi-1}}G^{s,(\chi)}\big|_\Sigma = 0; \quad (9)$$

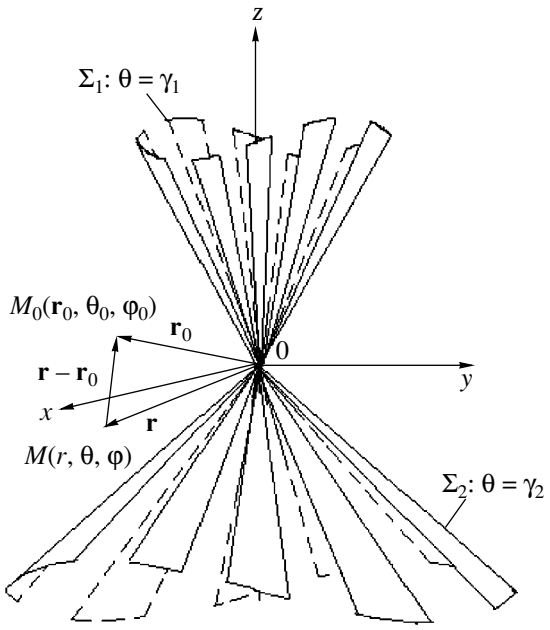

Fig. 1. Structure geometry.

the principle of the ultimate absorption;

and the bounded-energy condition.

We assume that $q > 0$. Then, we perform the analytical extension in finite formulas. In accordance with (6), we write $G^{s,(1)}$ in the form

$$G^{s,(\chi)}(\mathbf{r}) = G_0^s(\mathbf{r}) + G_1^{s,(\chi)}(\mathbf{r}),$$

where

$$G_0^s(\mathbf{r}) = \frac{e^{-(qR + st_0)}}{4\pi R} = \frac{2}{\pi^2}\int_0^{+\infty} \tau\sinh\pi\tau\widehat{G}_0^s\frac{K_{i\tau}(qr)}{\sqrt{r}}d\tau,$$

$$\widehat{G}_0^s = \sum_{m=-\infty}^{+\infty} \widehat{\alpha}_{m\tau}^s\widehat{U}_{m\tau}^{(0)}e^{im\varphi},$$

$$U_{m\tau}^{(0)}(\theta, \theta_0) = \begin{cases} P_{-1/2+i\tau}^m(\cos\theta)P_{-1/2+i\tau}^m(-\cos\theta_0), \\ \theta < \theta_0 \\ P_{-1/2+i\tau}^m(-\cos\theta)P_{-1/2+i\tau}^m(\cos\theta_0), \\ \theta_0 < \theta, \end{cases} \quad (10)$$

$$\widehat{\alpha}_{m\tau}^s = \frac{(-1)^m}{4\cosh\pi\tau}\frac{K_{i\tau}(qr_0)}{\sqrt{r_0}}\frac{\Gamma\left(\frac{1}{2} - m + i\tau\right)}{\Gamma\left(\frac{1}{2} + m + i\tau\right)}e^{-i(st_0 + m\varphi_0)}.$$

Here, $K_{i\tau}(qr)$ is the modified Bessel function of the second kind; $P^m_{-1/2+i\tau}(\cos\theta)$ is the associated Legendre function of the first kind; and $\Gamma(z)$ is the gamma function. To solve problem (8), (9), we exploit the integral Kontorovich–Lebedev representation:

$$\hat{g}(\tau) = \int_0^{+\infty} g(r)\frac{K_{i\tau}(qr)}{\sqrt{r}}dr, \tag{11}$$

$$g(r) = \frac{2}{\pi^2}\int_0^{+\infty} \tau\sinh\pi\tau\hat{g}(\tau)\frac{K_{i\tau}(qr)}{\sqrt{r}}d\tau. \tag{12}$$

We now represent $G_1^{s,(1)}(\mathbf{r})$ in the form of (12). In this case, we have

$$G_1^{s,(\chi)}(\mathbf{r}) = \frac{2}{\pi^2}\int_0^{+\infty} \tau\sinh\pi\tau\hat{G}_1^{s,(\chi)}\frac{K_{i\tau}(qr)}{\sqrt{r}}d\tau; \tag{13}$$

$$\begin{gathered}\hat{G}_1^{s,(1)} = \sum_{m=-\infty}^{+\infty} \hat{b}^s_{m\tau}\hat{U}^{(1)}_{m\tau}(\theta,\varphi),\\ \hat{b}^s_{m\tau} = -\hat{\alpha}^s_{m\tau}P^m_{-1/2+i\tau}(-\cos\theta_0)P^m_{-1/2+i\tau}(\cos\gamma_2),\\ \gamma_2 < \theta_0;\end{gathered} \tag{14}$$

$$\hat{U}^{(\chi)}_{m\tau} = \begin{cases} \sum\limits_{n=-\infty}^{+\infty} \hat{\alpha}^{(\chi)}_{mn}P^{m+nN}_{-1/2+i\tau}(\cos\theta)e^{i(m+nN)\varphi}, \\ 0 < \theta < \gamma_1 \\ \sum\limits_{n=-\infty}^{+\infty} [\hat{\beta}^{(\chi)}_{mn}P^{m+nN}_{-1/2+i\tau}(\cos\theta) \\ + \hat{\xi}^{(\chi)}_{mn}P^{m+nN}_{-1/2+i\tau}(-\cos\theta)]e^{i(m+nN)\varphi}, \quad \gamma_1 < \theta < \gamma_2 \\ \sum\limits_{n=-\infty}^{+\infty} \hat{\zeta}^{(\chi)}_{mn}P^{m+nN}_{-1/2+i\tau}(-\cos\theta)e^{i(m+nN)\varphi}, \\ \gamma_2 < \theta < \pi. \end{cases} \tag{15}$$

Here, $\hat{\alpha}^{(\chi)}_{mn}$, $\hat{\beta}^{(\chi)}_{mn}$, $\hat{\xi}^{(\chi)}_{mn}$, and $\hat{\zeta}^{(\chi)}_{mn}$ are unknown coefficients independent of the parameter q. Based on the results of [3, 8], one can show that the Green's function $G^{(\chi)}_\kappa(\mathbf{r}, t)$ (6) ($\kappa = 0, 1$) can be represented (in a unique manner) as the integral

$$G^{(\chi)}_\kappa(\mathbf{r}, t) = \int_0^{+\infty} \tau\tanh\pi\tau\tilde{\tilde{G}}^{(\chi)}_\kappa P_{-1/2+i\tau}(\cosh b)d\tau, \tag{16}$$

where

$$\tilde{\tilde{G}}_0 = \frac{1}{r}\eta\left(t - t_0 - \frac{r+r_0}{a}\right)\sum_{m=-\infty}^{+\infty} a_{m\tau}U^{(0)}_{m\tau}e^{im\varphi}, \tag{17}$$

$$\begin{gathered}\tilde{\tilde{G}}^{(\chi)}_1 = -\frac{1}{r}\eta\left(t - t_0 - \frac{r+r_0}{a}\right)\sum_{m=-\infty}^{+\infty} a_{m\tau}\hat{U}^{(\chi)}_{m\tau}\\ \times P^m_{-1/2+i\tau}(-\cos\theta_0)P^m_{-1/2+i\tau}(\cos\gamma_2),\end{gathered}$$

$$a_{m\tau} = \frac{1}{4\pi r_0}(-1)^m e^{-im\varphi_0}\frac{\Gamma\left(\frac{1}{2} - m + i\tau\right)}{\Gamma\left(\frac{1}{2} + m + i\tau\right)}, \tag{18}$$

$$\cosh b = \frac{a^2(t-t_0)^2 - r^2 - r_0^2}{2rr_0}, \quad b \in [0, +\infty).$$

The integral representation of type (16) is a version of the Meler–Fock integral representation [4], which can be written in the form

$$\Psi(b) = \int_0^{+\infty} \tau\tanh\pi\tau\hat{\Psi}(\tau)P_{-1/2+i\tau}(\cosh b)d\tau, \tag{19}$$

where

$$\hat{\Psi}^{(\tau)} = \int_0^{+\infty} \sinh b\Psi(b)P_{-1/2+i\tau}(\cosh b)db, \quad b \in [0, +\infty). \tag{20}$$

The Green's function $G^{(\chi)}_1(\mathbf{r}, t)$ (6) for a complicated conic structure Σ can be found by using integral transformations (19), (20), representations (17), (18), boundary condition (3), and the conjugation condition in slots. As a result, we arrive at two coupled sets of functional equations for the determination of unknown coefficients of the function $\hat{U}^{(\chi)}_{m\tau}$ (15). The form of these sets is presented in [3, 9], and their solution can be obtained employing the method of singular integral equations or the method of the Riemann–Hilbert problem [3, 5]. We present expressions describing the Debye potentials in certain particular cases of a complicated conic structure and the function $f(t - t_0)$.

(A). $f(t) = e^{i\alpha\omega t}$, $\alpha = \pm 1$, $t_0 = 0$.

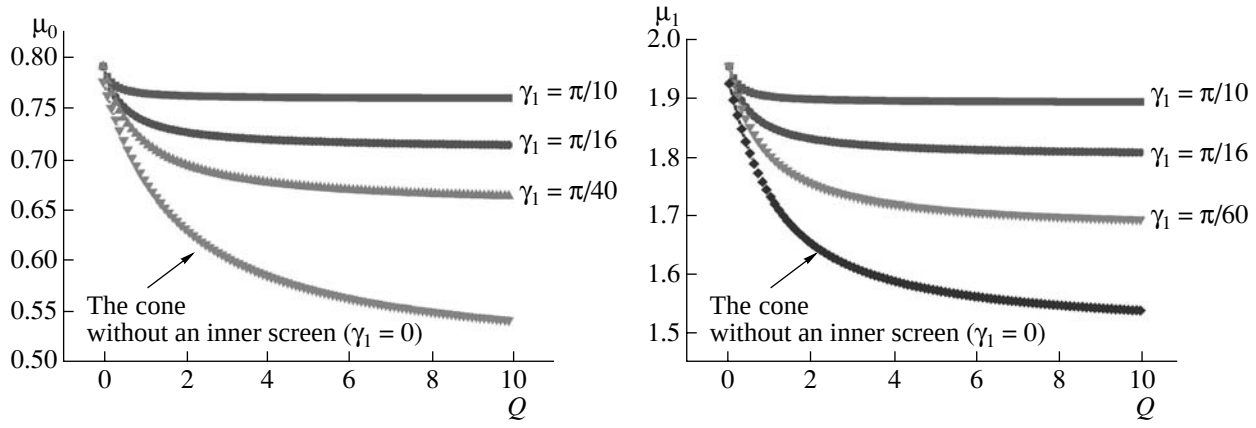

Fig. 2. Dependence of the function $\mu_n(Q, \gamma_1, \gamma_2)$ on the filling parameter Q for different angles γ_1; $\gamma_2 = \frac{\pi}{8}$.

The single cone Σ_1 with N narrow slots $\left(\chi = 2, \frac{d_1}{l} \ll 1, \theta_0 = \pi\right)$:

$$\upsilon_1^{(2)} = \upsilon_{1\text{solid}}^{(2)} + \frac{1}{-\frac{1}{N}\ln\left(\frac{1-u_1}{2}\right)}\int_0^\infty a_{i\tau}^{*(2)}\frac{K_{i\tau}(\tilde{q}r)}{\sqrt{r}}\frac{F_{i\tau}^*}{\tilde{W}_{i\tau}^{(2)}}$$

$$\times A_{i\tau}^{*(2)} P_{-1/2+i\tau}(-\cos\theta)d\tau + \frac{1}{-\frac{1}{N}\ln\left(\frac{1-u_1}{2}\right)}$$

$$\times\int_0^\infty a_{i\tau}^{*(2)}\frac{K_{i\tau}(\tilde{q}r)}{\sqrt{r}}\frac{F_{i\tau}^*}{\tilde{W}_{i\tau}^{(2)}}A_{i\tau}^{*(2)}$$

$$\times\sum_{n\neq 0}\frac{1}{1-\frac{|n|}{n}\varepsilon_{n,2}^{*(2)}V_{n-1}^{n-1}(u_1)}\frac{P_{-1/2+i\tau}^{nN}(-\cos\theta)}{\frac{d}{d\gamma_2}P_{-1/2+i\tau}^{nN}(-\cos\gamma_2)}$$

$$\times e^{inN\varphi}d\tau + O(1-u_1), \quad \gamma_1 < \theta < \pi, \qquad (21)$$

$$\tilde{W}_{i\tau}^{(2)} = F_{i\tau}^* + \frac{1}{-\frac{1}{N}\ln\left(\frac{1-u_1}{2}\right)},$$

$$F_{i\tau}^* = \frac{1}{A_{i\tau}^{*(2)} - \frac{1}{N}\sum_{p\neq 0}\frac{1}{|p|}\varepsilon_{p,2}^{*(2)}}.$$

Here, $u_1 = \cos\left(\frac{\pi d_1}{l}\right)$, $\tilde{q} = i\alpha k$, k is the wave number; $a_{i\tau}^{*(2)}$, $\varepsilon_{n,\tau}^{*(2)}$, and $A_{i\tau}^{*(2)}$ are the known coefficients; the functions $V_{n-1}^{n-1}(u_1)$ are defined in [10]; and $\upsilon_{1\text{solid}}^{(2)}$ are the potentials for the solid cone Σ_1 [11]. Representation (21) is valid far from the slots.

(B). $f(t-t_0) = \delta(t-t_0)$, $\chi = 1$, $\theta_0 = \pi$.

The conic structure Σ consists of a solid cone Σ_1 and a semitransparent cone Σ_2. The latter is determined by the existence of the limit

$$Q = \lim_{\substack{N\to+\infty \\ d_2/l\to 1}}\left[-\frac{1}{N}\ln\cos\frac{\pi d_2}{2l}\right],$$

$$\upsilon_1^{(1)} = \eta\left(t - t_0 - \frac{r+r_0}{a}\right)\frac{Q}{r}\sum_{n=0}^{+\infty}\psi_{\mu_n}(\gamma_1, \gamma_2)$$

$$\times P_{-1/2+\mu_n}(-\cos\theta)Q_{-1/2+\mu_n}(\cosh b), \quad \gamma_2 < \theta < \pi, \qquad (22)$$

$$\psi_\mu(\gamma_1, \gamma_2) = -\frac{ab^{(1)}}{\pi r_0^2}\mu\cos\pi\mu$$

$$\times\frac{\Delta_\mu(\gamma_1, \gamma_2)}{P_{-1/2+\mu}(-\cos\gamma_1)\frac{d}{d\mu}\nabla_\mu}\frac{P_{-1/2+\mu}(\cos\gamma_2)}{P_{-1/2+\mu}(-\cos\gamma_2)},$$

$$\nabla_\mu = \pi\frac{P_{-1/2+\mu}(-\cos\gamma_2)}{P_{-1/2+\mu}(-\cos\gamma_1)}\Delta_\mu^{(1),0}(\pi-\gamma_1, \pi-\gamma_2) \qquad (23)$$

$$+ 2Q\cos\pi\mu, \quad \nabla_{\mu_n} = 0,$$

where $Q_{-1/2+\mu}(\cosh b)$ is the Legendre function of the second kind. Representation (22) is obtained from (16) as a result of the expansion of the integral (after the passage in (16) to integration over the imaginary axis $\mu = i\tau$) into a series in terms of residues of the integrand in its simple poles $\mu_n(Q, \gamma_1, \gamma_2)$, in which are contained the

roots of Eq. (23). Figure 2 exhibits the values μ_0, μ_1 as functions of the filling parameter Q for $\gamma_2 = \frac{\pi}{8}$ and different angles γ_1. The sequence of values $\{\mu_n\}_{n=0}^{+\infty}$ is monotonically increasing. The least of the values μ_0 determines the field behavior near the structure vertex and the field spatial distribution in the case when the source is closely located to the vertex.

Thus, we have proposed and substantiated a method for solving boundary value problems of diffraction in the time region for complicated three-dimensional unclosed conic structures. The method constitutes a generalization of the results reported by the authors in [3, 9] as applied to solving problems of wave diffraction on unclosed perfectly conducting bicones in the frequency region. This approach can also be used in solving time-dependent problems of wave diffraction on three-dimensional impedance structures of conic geometry.

REFERENCES

1. V. A. Doroshenko and V. G. Sologub, Radiotekh. Elektron. (Moscow) **32**, 1110 (1987).
2. V. A. Doroshenko and V. F. Kravchenko, Dokl. Akad. Nauk **375** (5), 611 (2000) [Dokl. Phys. **45** (12), 659 (2000)].
3. V. A. Doroshenko and V. F. Kravchenko, Élektromagn. Volny Élektron. Sist. **8** (6), 2 (2003).
4. V. A. Fock, Dokl. Akad. Nauk SSSR **39** (7), 279 (1943).
5. V. A. Doroshenko and V. F. Kravchenko, Differ. Uravn. **39**, 1209 (2003).
6. O. A. Ladyzhenskaya, *Boundary Value Problems of Mathematical Physics* (Nauka, Moscow, 1973; Springer, New York, 1985).
7. H. Hönl, A. W. Maue, and K. Westpfahl, in *Handbuch der Physik*, Ed. by S. Flügge (Springer, Berlin, 1961; Mir, Moscow, 1964), Vol. 25, p. 218.
8. K.-K. Chan and L. B. Felsen, IEEE Trans. Antennas, Propag. **25** (6), 802 (1977).
9. V. A. Doroshenko, Usp. Sovrem. Radioélektron., No. 5, 41 (2005).
10. V. P. Shestopalov, *Methods of Solving Riemann–Hilbert Problem in the Diffraction Theory and Electromagnetic-Wave Transmission* (Izd. Kharkov Univ., Kharkov, 1971) [in Russian].
11. L. B. Felsen and N. Marcuvitz, *Radiation and Scattering of Waves* (Prentice-Hall, Englewood Cliffs, 1973; Mir, Moscow, 1978).

Translated by G. Merzon

Doklady Physics, Vol. 50, No. 11, 2005, pp. 565–569. Translated from Doklady Akademii Nauk, Vol. 405, No. 2, 2005, pp. 188–192.

PHYSICS

High-Temperature Polymorphism in Rare Earth Elements

N. N. Sirota[a], A. V. Morozov[a], I. M. Sirota[b], and T. M. Soshnina[a]

Presented by Academician V.V. Osiko July 8, 2005

Received July 8, 2005

Most rare earth (RE) elements exhibit structural polymorphic transitions from low-temperature (I) to high-temperature (II) modifications in the vicinity of the corresponding melting temperatures. Among the fourteen 4*f* elements (in which the 4*f* electron orbital is occupied), there are apparently only two (europium and thulium) that are not subject to such high-temperature structural transformations. We have considered the crystal structures, evaluated the temperature intervals of the existence of the equilibrium RE polymorphs I and II, and determined the corresponding characteristic (Debye) temperatures θ_I and θ_{II}. In addition, we have established relationships between the θ_I and θ_{II} values, on the one hand, and the temperatures T_k of the corresponding polymorphic transitions and the melting temperatures T_m, on the other hand. The enthalpies ΔH_k of the polymorphic transitions determined using the θ_I and θ_{II} values are similar to the available experimental data.

The high-temperature polymorphic transitions in RE elements exhibit interesting characteristic features. In particular, the I–II transition temperatures T_k are close to the corresponding (relatively high) melting temperatures T_m: the ratios T_k/T_m vary from 0.87 for Nd to 0.98 for Dy (Fig. 1). In all RE elements, the high-temperature phase II has a relatively narrow temperature region of the equilibrium existence. Among the "light" RE elements, the difference $T_m - T_k$ is minimum for Ce (69 K) and maximum for Sm (160 K). For the "heavy" RE elements, this difference ranges from 24 K (for Yb) and 28 K (Dy) to 162 K (Er). Accordingly, the relative difference $(T_m - T_k)/T_m$ varies with the atomic number as depicted in Fig. 2.

The temperature region of the equilibrium existence of the high-temperature phase II significantly increases in the sequence Pr, Nd, Sm, while it decreases in the sequence Gd, Tb, Dy, Ho. This variation can be considered in relation to the number of *f* electrons, which increases to seven on the passage from Ce to Eu (in which all seven branches of the *f* orbital are occupied by one electron) and then changes on the passage from Gd to Lu in accordance with Hund's rule.

Let us consider some structural characteristics of polymorphs I and II for RE elements. Most of them (except for Tm) exist at the melting temperature in the form of polymorphs II with A2 (bcc) type structures (Tm has an hcp structure of the A3 type). The structure of Lu at the melting temperature is still unclear, although it was also proposed to be of the A2 type [2].

The polymorphs I in almost all RE elements have A3 type structures, Pr and Nd have the double hexagonal structure A3; the low-temperature modifications of Ce and Yb have the A1 type fcc structures, and Sm has a rhombohedral structure. Table 1 presents data on the structural types and lattice periods of the crystal structures of the RE polymorphs I and II.

The high-temperature polymorphic I–II transition is accompanied by a relatively small change in the volume per atom, which is inconsistent with a change in the packing coefficient of identical balls upon the A2–A3 transition. The relative difference of atomic volumes of the RE polymorphs I and II amounts to ~2% for Pr and ~0.6% for Lu. Figure 3 presents a diagram of the specific volumes (per atom) for the RE polymorphs,

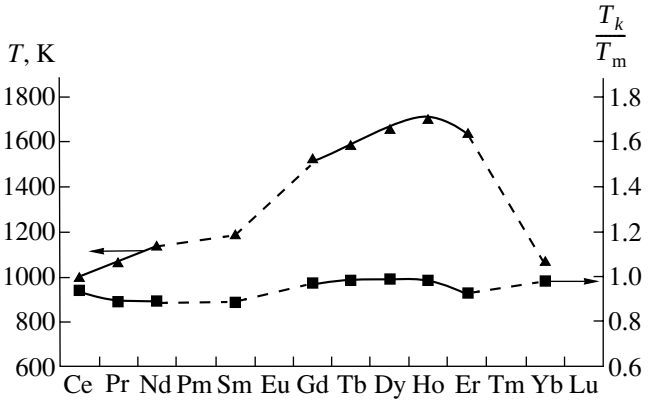

Fig. 1. Variation of the I–II polymorphic transition temperature T_k and the $\frac{T_k}{T_m}$ ratio in the sequence of rare earth elements.

[a] *Moscow State University of Applied Ecology, Moscow, Russia*

[b] *Institute of Control Sciences, Russian Academy of Sciences, ul. Profsoyuznaya 65, Moscow, 117997 Russia*

1028-3358/05/5011-0565$26.00 © 2005 Pleiades Publishing, Inc.

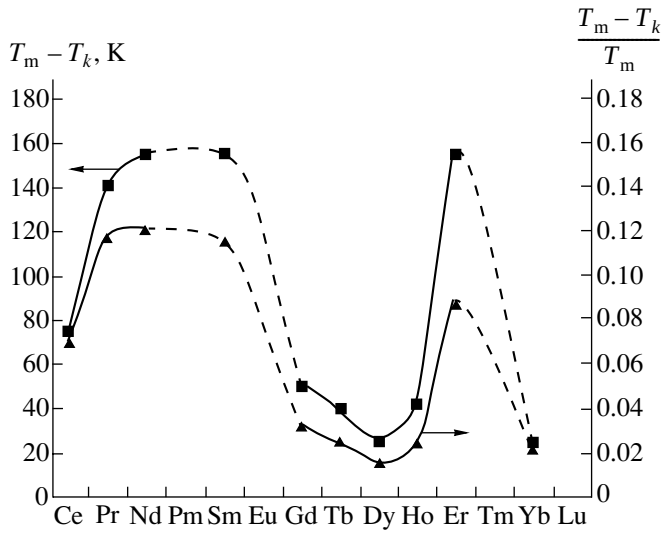

Fig. 2. Variation of the $T_m - T_k$ difference and the $\frac{T_m - T_k}{T_m}$ ratio for the I–II polymorphic transition in the sequence of rare earth elements.

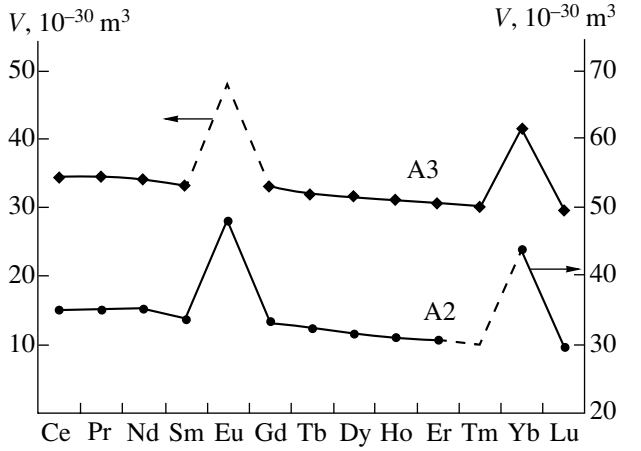

Fig. 3. Variation of the atomic volume V of polymorphs with the A2 and A3 type structures in the sequence of rare earth elements.

which shows a virtually linear general decrease in the atomic volume with increasing atomic number (nuclear charge) with a slope of

$$\frac{1}{V_{Z=59}}\frac{V_{59}-V_{71}}{Z_{59}-Z_{71}} = -1.2\times10^{-2}$$

for polymorph II and

$$\frac{1}{V_{Z=59}}\frac{V_{59}-V_{71}}{Z_{59}-Z_{71}} = -1.1\times10^{-2}$$

for polymorph I. There are small deviations from linearity for Ce, Nd, Gd, and Lu and significant deviations for Eu and Yb. For Eu and Yb, the atomic volumes are 30% greater than the values for their closest neighbors (Gd and Lu, respectively).

There is a significant difference in the volume per atom between the beginning and the end of the RE group. Indeed, this difference for Pr and Lu reaches $\frac{V_{Pr}-V_{Lu}}{V_{Pr}} \approx 16\%$ in modification II and 15% in modification I. For comparison, the change in the specific volume for La upon heating from T = 300 to 900°C is as small as ~1.5% [7]. Thus, the change in the atomic volume for La in a broad temperature range is smaller than the variation of this value in the RE sequence from Ce to Lu, where it is caused by a change the nuclear charge.

Let us consider the characteristic (Debye) temperatures θ_I and θ_{II} of the RE polymorphs I and II, respectively. As is known, the temperature of the polymorphic transition corresponds to the point of intersection of the curves of free energies of the corresponding phases. In the Debye approximation, the temperature dependences of these free energies are determined by the characteristic temperatures θ_I and θ_{II}. The condition of intersection of the free energy curves implies that $\theta_I > \theta_{II}$; that is, the Debye temperature of the low-temperature polymorph is always higher than that of the high-temperature polymorph. Published data show a considerable scatter of the characteristic temperatures experimentally determined for the low-temperature polymorphs [1, 4, 10–12], while data on the characteristic temperatures for the high-temperature polymorphs are almost entirely absent.

Table 2 presents the values of characteristic temperatures for the RE polymorphs I according to reference data [4] in comparison to the results of our calculations based on the average sound velocity $\bar{c}$ in polycrystalline samples [8]. These calculations were performed using the formula

$$\theta_I = \frac{h}{k}\left(\frac{3N_A}{4\pi V}\right)^{1/3}\bar{c}, \qquad (1)$$

where h is the Planck constant; k is the Boltzmann constant; N_A is the Avogadro number; V is the molar volume [cm^3/mol]; and $\bar{c}$ is the average velocity of sound, which is related to the longitudinal (c_l) and transverse (c_t) sound velocities by the relation

$$\bar{c} = \left(\frac{3c_l^3c_t^3}{c_t^3+2c_l^3}\right)^{1/3}. \qquad (2)$$

Alternatively, the characteristic temperatures of the RE polymorphs I and II were estimated using the Lindemann–Gilvarry method. Unlike the conventional

Table 1. The structural types, lattice parameters and their ratios*, atomic volumes V, melting temperatures T_m, and atomization energies ΔH_{at} of rare earth elements

Element	Structure	Lattice parameters, pm [3]		$\frac{c}{a}$	V, 10^{-30} m^3	T_m, K [2]	ΔH_{at}, kJ/mol [2]
		a	c				
Ce	A3'	367.3	1180.2	1.6066	34.47	1072	423.0
	A1	516.01			34.35		
	A2	412			34.97		
Pr	A3'	367.25	1183.5	1.6113	34.56	1204	355.6
	A2	413			35.22		
Nd	A3'	365.79	1179.92	1.6128	34.18	1294	327.6
	A2	413			35.22		
Sm	Rhom.	899.6, $\alpha = 23°13'$	(a = 362.1, c = 2625)	1.611	33.12	1350	206.7
	A2	407			33.71		
Eu	A2	458.2			48.10	1095	175.3
Gd	A3	363.60	578.26	1.5904	33.10	1586	397.5
	A2	405			33.22		
Tb	A3	360.10	569.36	1.5811	31.97	1629	388.7
	A2	402			32.48		
Dy	A3	359.03	564.75	1.5730	31.52	1685	290.4
	A2	398			31.52		
Ho	A3	357.73	561.58	1.5698	31.12	1747	300.8
	A2	396			31.05		
Er	A3	355.88	558.74	1.5700	30.64	1802	317.1
	A2	394			30.58		
Tm	A3	353.75	555.46	1.5702	30.10	1818	232.2
Yb	A3	387.99	638.59	1.6459	34.47	1097	152.3
	A1	548.62			41.28		
	A2	444			43.76		
Lu	A3	350.31	555.09	1.5846	29.50	1936	427.6
	A2	390.0			29.66		

* $\frac{c}{a} = \frac{c}{2a}$ (for Ce, Pr, Nd), $\frac{c}{4.5a}$ (for Sm), and $\frac{c}{a}$ otherwise.

approach, according to which θ is determined using the melting temperature, we determined θ_I for polymorph I using the temperature T_k of the I–II polymorphic transition.

According to the original Lindemann theory [5], a metal exhibits melting when the amplitude of atomic oscillations becomes equal to a certain fraction ($\frac{1}{\eta'}$) of the distance δ between the nearest neighboring atoms. Assuming that the energy ε_m of an atom oscillating with a frequency of ω and an average amplitude of a_m at the melting temperature T_m is kT_m, we obtain the following relation:

$$\varepsilon_m = \frac{1}{2} m\omega^2 a_m^2 f(z) = kT_m,$$

where $m = m_H A$, m_H is the proton mass, A is the atomic number, $\omega = 2\pi\nu$ (ν is the average frequency of atomic oscillations), $a_m \approx \frac{\delta}{\eta'}$, and $f(z)$ is a function taking into account the number of bonds of a given atom.

Table 2. The polymorphic transition temperatures T_k and enthalpies ΔH_k and the characteristic temperatures θ_I and θ_{II} of the rare earth polymorphs I and II

Element	θ_I, K [4]	θ_I^*, K	ΔH_k, J/mol [1]	T_k, K [1]	θ_I, K [formula (5)]	θ_{II}, K [formula (4)]	θ_{II}, K [formula (6)]	ΔH_k^{**}, J/mol
Ce	179	145	2932	1003	154	133	137	3841
Pr	152	144	3200	1065	157	140	139	3201
Nd	163	148	3009	1135	161	143	145	3202
Sm	169	135	3124	1190	163	145	147	3206
Eu	117					116		
Gd	182	174	3900	1535	180	155	163	4451
Tb	178	173	5000	1590	184	157	162.6	4927
Dy	183	180	3978	1657	187	160	170	4804
Ho	190	183	4689	1701	189	162	169	4787
Er	188	191		1640	185	164		3580
Tm	200							
Yb	118	96	1750	1073	135			
Lu	183					168		

* Determined using data on the velocity of sound.

** Calculated using the data on θ_I and θ_{II}.

Using the above relations and defining the characteristic temperature as $\theta = h\frac{\nu}{k}$, we obtain

$$\theta = \frac{\hbar}{\left(\frac{1}{2}m_H k f(z)\right)^{1/2}}\frac{\eta'}{\delta}\sqrt{\frac{T_m}{A}}. \quad (3)$$

Introducing the notation

$$\eta = \frac{\hbar\eta'}{\left(\frac{1}{2}m_H k f(z)\right)^{1/2}},$$

we can rewrite formula (3) as

$$\theta = \frac{\eta}{\delta}\sqrt{\frac{T_m}{A}}. \quad (4)$$

The Lindemann theory was later developed by Gilvarry [6], who suggested that the rms dynamic atomic displacement $\sqrt{\overline{u^2}}$ at the melting temperature amounts to a certain fraction of the distance δ between the nearest neighboring atoms. According to the Debye–Waller relation, $\overline{u^2}$ is a function of θ:

$$\overline{u^2} = \frac{3\hbar^2}{mk\theta}\left[\frac{\Phi(x)}{x} + \frac{1}{4}\right],$$

where $x = \frac{\theta}{T}$ and $\Phi(x) = \int_0^x \frac{x}{e^x - 1}dx$.

Then, by analogy with relation (4), we assumed that the characteristic temperature of the low-temperature polymorph I can be expressed as

$$\theta_I = \frac{\chi}{\delta}\left(\frac{T_k}{A}\right)^{1/2}, \quad (5)$$

where T_k is the temperature of the I–II polymorphic transition, δ is the distance between the nearest neighboring atoms in polymorph I, and χ is a numerical coefficient (which was taken as equal to 210). The values of the characteristic temperatures θ_I of the low-temperature RE polymorphs I calculated using formula (5) are presented in Table 2. As can be seen, the obtained θ_I values are close to the published data [4].

The characteristic temperatures of the RE polymorphs II possessing A2 type structures were calculated using their melting temperatures by formula (4) with

$\eta = 171$. The results of these calculations are also given in Table 2.

Previously, Zener [9] established a relation between the enthalpy ΔH_k of a polymorphic transition, the transition temperature T_k, and the ratio of characteristic temperatures of the low-temperature (θ_I) and high-temperature (θ_{II}) phases:

$$\frac{\theta_I}{\theta_{II}} = \exp\left(\frac{\Delta H_k}{3RT_k}\right), \quad (6)$$

where $R = 8.31$ J/(mol K). Using this relation with the characteristic temperatures θ_I calculated by formula (5) and the experimental values of ΔH_k, we determined the Debye temperatures for the high-temperature RE polymorphs II, which are presented in Table 2. As can be seen, the values obtained using the Lindemann–Gilvarry theory (formula (4)) and according to Zener (equation (6)) are quite similar.

Using the characteristic temperatures θ_I and θ_{II} calculated by formulas (4) and (5), we have estimated the enthalpies of the I–II polymorphic transitions in RE elements, together with the Helmholtz free energies, the internal energies, and the entropies of each polymorph. The enthalpy of the transition at $T = T_k$ was determined as $\Delta H_k = T_k \Delta S_k$. In these calculations, we used the tabulated values of Debye functions (Helmholtz free energy and entropy) and assumed that the differences of heat capacities at constant pressure and constant volume, $c_P - c_V$, for both high- and low-temperature polymorphs are small. Table 2 presents the experimental data and the results of calculations for the enthalpies of the I–II polymorphic transitions in RE elements. As can be seen, the calculated and experimental values are in most cases similar to each other.

The method developed in this study for the calculation of θ_I, θ_{II}, and ΔH_k values can also be useful for the analysis of polymorphism in other systems.

REFERENCES

1. *Handbook on the Physics and Chemistry of Rare Earths*, Ed. by K. A. Gschneider, Jr. and L. Eyring (North-Holland, Oxford, 1978), Vol. 1.
2. J. Emsley, *The Elements* (Clarendon, Oxford, 1989; Mir, Moscow, 1993).
3. *The Rare Earths*, Ed. by F. H. Spedding and A. H. Daane (Wiley, New York, 1961; Metallurgiya, Moscow, 1965).
4. *Handbook of Physical Quantities*, Ed. by I. S. Grigoriev and E. Z. Meilikhov (Énergoatomizdat, Moscow, 1991; CRC, Boca Raton, 1997).
5. F. A. Lindemann, Z. Phys. **11**, 609 (1910).
6. J. J. Gilvarry, Phys. Rev. **102**, 308 (1956).
7. F. H. Spedding, J. J. Hanak, and A. H. Daane, J. Less-Common Met. **3**, 110 (1961).
8. J. F. Smith, C. E. Carlson, and F. H. Spedding, J. Metals **9** (10), 1212 (1957).
9. C. Zener and S. Bilinsky, Phys. Rev. **50**, 101 (1936).
10. V. E. Zinov'ev, *Thermophysical Properties of Metals at High Temperatures* (Metallurgiya, Moscow, 1989) [in Russian].
11. E. M. Savitskiĭ and V. F. Terekhova, *Physical Metallurgy of Rare-Earth Metals* (Nauka, Moscow, 1975) [in Russian].
12. K. A. Gshneidner, Jr., *Rare Earths Alloys* (Van Nostrand, New, York, 1961; Mir, Moscow, 1965).

Translated by P. Pozdeev

Doklady Physics, Vol. 50, No. 11, 2005, pp. 570–576. Translated from Doklady Akademii Nauk, Vol. 405, No. 3, 2005, pp. 325–331.

PHYSICS

Cavitation and the Stability Region of Liquid Lead at Negative Pressures: Molecular Dynamics Study

T. T. Bazhirov, G. É. Norman, and V. V. Stegaĭlov

Presented by Academician V.E. Fortov May 3, 2005

Received May 25, 2005

Cavitation kinetics has traditionally been described in terms of classical nucleation theory (CNT) based on the thermodynamic calculation of work on the formation of a nucleus of a new phase and the solution of the kinetic equation of the nucleus size distribution [1]. The application of CNT is often complicated by the uncertainty associated with the actual accuracy of the model approximations that underlie the theory, as well as by the absence of sufficiently reliable data on the surface tension at the interface and the equation of state of a metastable liquid.

Molecular dynamics (MD) simulation makes it possible to study the process of cavitation on the microscopic level by using only a chosen potential of interatomic interaction without additional assumptions about mechanisms of the formation and growth of cavities. For example, molecular dynamics investigation of the cavitation process in a Lennard-Jones liquid showed that the appearance and growth of a localized vapor nucleus are clearly observed in a system consisting of 10 976 particles [2]. The effect of the cutoff radius of the interparticle interaction potential was analyzed in [3]. A method of calculating the homogeneous nucleation rate in a metastable phase was proposed in [4], where nucleation in a superheated crystal was considered as an example. This method is based on averaging the lifetime of the metastable phase over an ensemble of independent MD trajectories. A similar approach was used in [3] to calculate the cavitation frequency in a Lennard-Jones liquid.

Lead was chosen for investigation, because it is the basic element in promising heat carriers for a new type of power reactors with the fast initiation of DT fuel [5]. Processes associated with the loss of continuity of a heat carrier (cavitation) during the relaxation of the stresses that accompany microexplosions in a working chamber significantly affect the operation of such systems (see, e.g., [6]). To simulate the operation of the system, information on the cavitation kinetics in the heat carrier under tensile stresses is needed.

In this study, the MD method with the use of a realistic potential of interatomic interaction in Pb is applied in order to investigate the stability boundary of liquid lead and the cavitation kinetics in the range of high negative pressures at temperatures that are much less than the critical one ($T < 0.5T_{CP}$). The results of the MD calculations are compared with the predictions of the CNT.

MODEL AND THE CALCULATION METHOD

In this study, to describe the interatomic interaction, we use a many-particle potential for Pb from a family of embedded atom potentials, which was proposed in [7]. The parameters of the potential were chosen so that they corresponded to the properties of a crystalline phase of lead (binding energy, surface energy, elastic constants, phonon frequencies, thermal expansion, and melting temperature). This potential was successfully used to study the melting and crystallization of surface and clusters, as well as the vaporization of nanoparticles [8]. In this case, it was shown, for example, that the melting and vaporization temperatures (618 ± 4 and ~2050 K, respectively) are in good agreement with their experimental values for lead (600.7 and 2033 K, respectively).

In this study, we consider a system consisting of $N = 13500$ atoms in a cubic calculation cell. Three-dimensional periodic boundary conditions are used. The atomic trajectories are calculated by numerically integrating the system of classical equations of motion in a second-order finite difference scheme with a step of 1.43 fs. The instantaneous values of the temperature

Institute of High Energy Densities,
Joint Institute for High Temperatures,
Russian Academy of Sciences, Izhorskaya ul. 13/19,
Moscow, 127412 Russia

1028-3358/05/5011-0570$26.00

and pressure averaged over the calculation-cell volume are evaluated as follows:

$$T = \frac{2m}{3k_B N}\sum_{i=1}^{N}\frac{\mathbf{v}_i^2}{2}, \quad P = \frac{1}{V}\left(Nk_B T - \frac{1}{3}\sum_{i<j} r_{ij}\frac{\partial U}{\partial r_{ij}}\right), \quad (1)$$
$$r_{ij} = |\mathbf{r}_i - \mathbf{r}_j|,$$

where k_B is the Boltzmann constant; m is the atomic mass; $\mathbf{r}_i$ and $\mathbf{v}_i$ are the current coordinate and velocity of the ith atom, respectively; V is the calculation-cell volume; and $U = U(\mathbf{r}_1, \mathbf{r}_2, \ldots, \mathbf{r}_N)$ is the potential energy of the system. To set and maintain a constant temperature in the process of calculations, a scheme of thermal stabilization (thermostat) is used: additional Langevin terms—self-consistent white noise and self-consistent friction force—are introduced into the equation of motion [9]. The total effect of these terms is small as compared to the interatomic-interaction forces.

An initial atomic configuration corresponding to the liquid phase was obtained as follows. A configuration representing a crystalline atomic lattice with a given density $\rho = \frac{mN}{V}$ and velocities chosen randomly according to the Maxwell distribution corresponding to the temperature T is preliminary formed. In this study, we investigate the metastable states of the liquid for densities and temperatures at which the possibility of the solid phase existing is excluded. Therefore, when calculating the MD trajectory, the lattice is transformed in several tens of femtoseconds to the liquid state with a given temperature T, which is further maintained by the thermostat for 10 ps. The final configuration of the preliminary MD calculation is the desired initial configuration. By using the different initial velocity distributions, an ensemble of independent initial configurations corresponding to the liquid for the given ρ and T values is formed.

STABILITY BOUNDARY OF THE METASTABLE LIQUID PHASE

In this study, we consider the cavitation process in a liquid at high negative pressures corresponding to the states close to the stability boundary (spinodal). To date, experimental data for the spinodals of liquid metals (including Pb) are absent. Moreover, the general characteristics of the spinodal of the liquid phase in the range of negative pressures at low temperatures ($0 < T < 0.5T_{CP}$) have been poorly studied (see, e.g., [10]). The position of the spinodal of liquid lead can be estimated using MD calculations of the spinodal of the Lennard-Jones liquid [11] and thermodynamic similarity on the critical parameters (Fig. 1). Thus, in the temperature interval under investigation, the negative pressures corresponding to the strongly extended metastable melt of lead are preliminarily estimated.

In the framework of the MD model under consideration, the position of the spinodal is calculated using the P vs. ρ dependences along isotherms and the point $\left(\frac{\partial P}{\partial \rho}\right)_T = 0$ by extrapolation (see the insert in Fig. 1). For each density value at a fixed temperature, the MD trajectory 50 ps long is calculated. At high densities (e.g., $\rho > 9.8$ g/cm^3 at $T = 1000$ K), the degree of metastability is small, and cavitation in the system during calculation is absent. The lifetime τ of the metastable liquid decreases with density, and cavitation can occur during calculations (Fig. 2). To construct an isotherm, the pressure P is averaged over the section of the MD trajectory before the onset of the phase transition ($0 < t < \tau$). When calculating the isotherm, the minimum density is determined from the degeneracy ($\tau \longrightarrow 0$) of a similar metastable section characterized by a pronounced constant pressure. Arbitrariness in the choice of an extrapolation function (in this study, we used polynomials of degrees $n = 2$–5) results in an ambiguous determination of the spinodal point (~7 and ~3% in P and ρ, respectively).

The calculation data are somewhat higher than the preliminary estimate of the spinodal from the similarity relations (when comparing, the possible error of experimental measurements of the critical parameters of lead should be taken into account). The closeness of the calculation data and the preliminary estimate of the spinodal can testify to the universal similarity of spinodals for simple liquids at low temperatures. We emphasize the qualitative difference of the compared models of interatomic interaction: the pair Lennard-Jones potential (with the interaction radius to the third coordination spheres) and the many-particle embedded atom potential (with the interaction radius to the second coordination spheres). In addition, note that, unlike the results for the Lennard-Jones system [11], the spinodal of the Pb melt does not intersect the continuation of the melting line of lead into the range of negative pressures according to the Simon equation. This behavior indicates that crystal–liquid phase equilibrium in a wide range of metastable states is possible.

CAVITATION RATE

In the model under consideration, cavitation occurs as random homogeneous nucleation, because the surface effects and spatial inhomogeneities are absent in the presence of periodic boundary conditions. The time at which cavity formation begins depends on local fluctuations of both the velocities of the particles that form a nucleus of a new phase (cavity) and the distances between them. According to the visual estimates in the

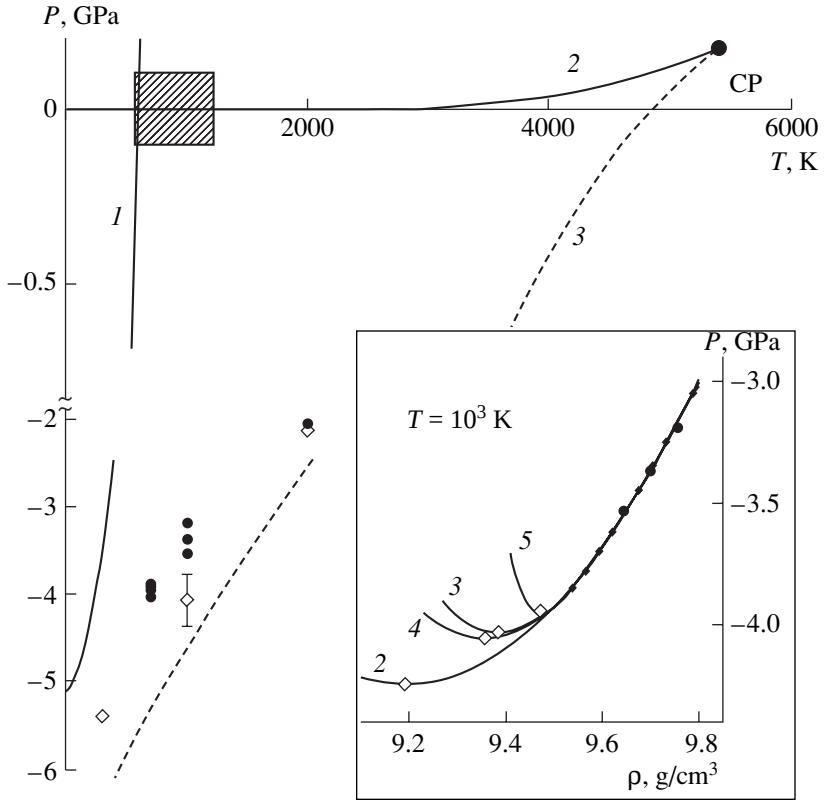

Fig. 1. *P–T* diagram of lead: (*1*) experimental melting curve and its extrapolation into the range of negative pressures according to the Simon equation $\frac{P}{P_*} = \left(\frac{T}{T_\mathrm{m}}\right)^c - 1$ ($P_* = 5.11$ GPa, $T_\mathrm{m} = 600$ K, and $c = 1.65$); (*2*) vaporization curve; and (*3*) estimate of the position of the spinodal for liquid lead by renormalizing the spinodal of the Lennard-Jones system using the parameters of the critical point CP ($T_\mathrm{CP} = 5400$ K and $P_\mathrm{CP} = 0.175$ GPa [12]). For clarity of the representation, the vertical axis of the graph is broken. Open diamonds are the spinodal points obtained in this study and circles are the states in which the cavitation frequency was calculated. The shaded area corresponds to the expected working parameters of the heat carrier in FIHIF reactors [5]. The insert shows an isotherm of liquid lead ($T = 10^3$ K). Solid lines correspond to extrapolations of (◆) the MD results by polynomials of degree 2–5. As an example, the corresponding uncertainty of the position of a point on the spinodal is shown by error bars on the *P–T* diagram.

density and temperature ranges under investigation, the size of a critical nucleus corresponds to the volume of no more than 10–100 atoms. Therefore, the periodic boundary conditions do not affect the initial stage of the cavitation process. The explosive growth of the cavity leads to a rapid unloading of the extended liquid. In this case, the effect of the periodic boundary conditions becomes essential and requires a separate study (to describe the further growth of the cavity into the range of supercritical sizes, for example, the equation of continuous medium can be used [6]).

On a particular MD trajectory, the lifetime of a homogeneous metastable liquid phase depends on the initial configuration and the initial distribution of the particle velocities, as well as on the integration step (in the case of identical initial conditions) [3, 4]. For a given thermodynamic state (ρ, *T*, and *P*), statistical averaging is performed over the ensemble *M* of independent initial microconfigurations, for each of which the corresponding lifetime τ_i ($i = 1, 2, \ldots, M$) is found. According to the model of homogeneous nucleation as a random Poisson process, the distribution of the lifetime τ_i over the ensemble of initial configurations has the form [1]

$$m(\tau) = \frac{M\Delta\tau}{\bar{\tau}}\exp\left(-\frac{\tau}{\bar{\tau}}\right), \quad \bar{\tau} = \frac{1}{M}\sum_{i=1}^{M}\tau_i, \qquad (2)$$

where $m(\tau)$ is the number of trajectories in the ensemble of the *M* trajectories on which the cavitation occurs within the time interval $(\tau, \tau + \Delta\tau)$ and $\bar{\tau}$ is the mean lifetime. Figure 3 shows the distributions obtained in the calculations. It is seen that model (2) describes rather well the cavitation process under consideration. To obtain distributions with a pronounced exponential form, a set of greater statistics ($M > 100$–200) is

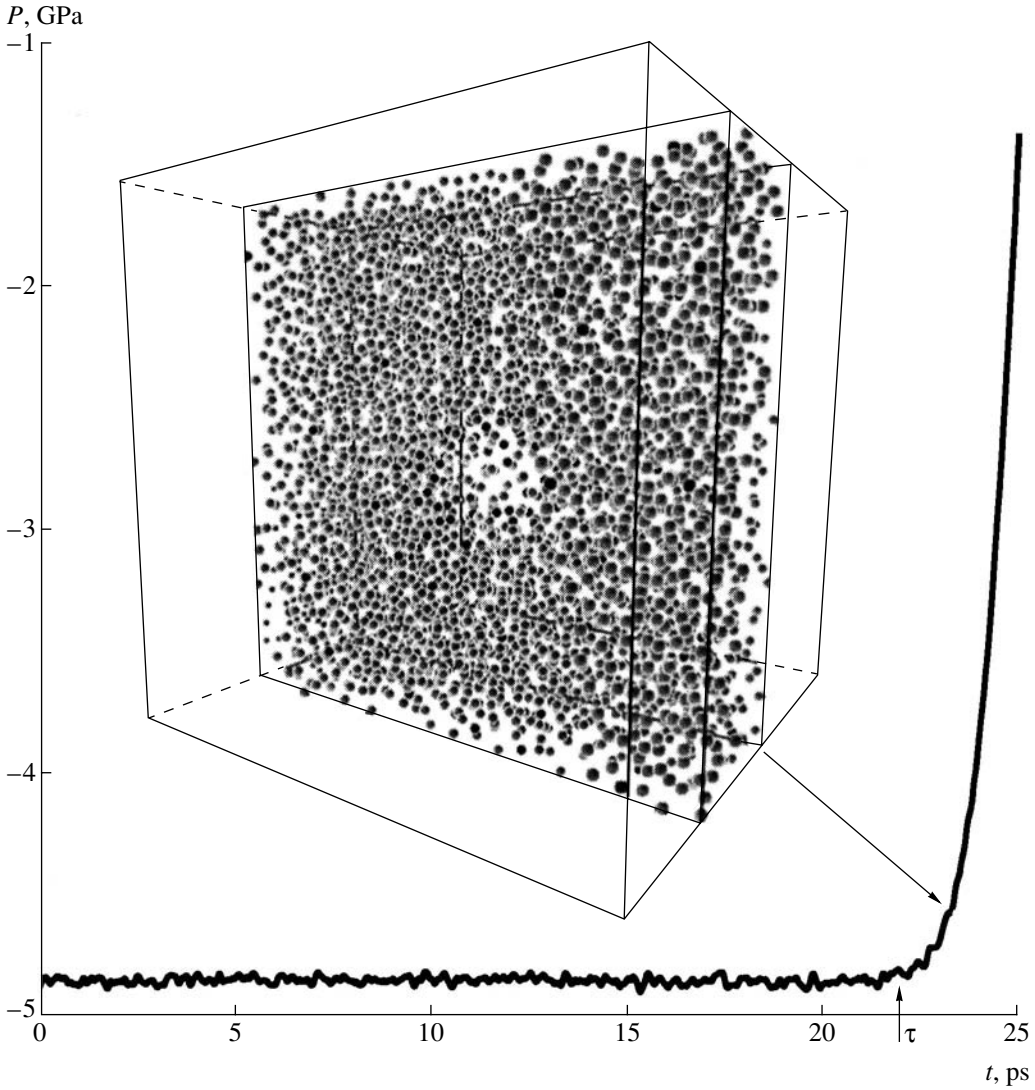

Fig. 2. Instantaneous pressure P vs. time t in the case of spontaneous decay of the extended liquid (T = 300 K). The lifetime τ of the metastable state on the given MD trajectory is shown by the arrow. A section of the structure in the calculation cell is shown. At the center of the section, a vapor nucleus is seen.

required. For the exponential distribution law, the rms error of finding $\bar{\tau}$ from M measurements is $\sigma_{\bar{\tau}} = \frac{\bar{\tau}}{\sqrt{M}}$. The rate of a spontaneous phase transformation is characterized by the average number of critical nuclei arising in unit volume in unit time, i.e., cavitation frequency J. In this study, the cavitation frequency is calculated as $J = \frac{1}{\bar{\tau}V}$. The calculation data are presented in Fig. 4.

DISCUSSION

Now, we compare the calculation data with the predictions of the CNT. We use the temperature dependence of the nucleation rate based on the Zeldovich approach [1, 13]:

$$J = \frac{\rho}{m}\sqrt{\frac{2\sigma}{\pi m}}\exp\left(-\frac{W}{k_B T}\right), \quad W = \frac{16\pi\sigma^3}{3(P-P')^2}, \qquad (3)$$

where σ is the surface tension along the vaporization curve at the temperature T, W is the work for the formation of the critical nucleus, and P' is the vapor pressure in the critical nucleus. Approximation (3) is chosen because of the simplicity of the pre-exponential factor, which contains no specific parameters characterizing the metastable liquid except σ.

When comparing Eq. (3) with the results of the MD calculations, we assume that the pressure in the system containing the critical nucleus is equal to the average pressure in the metastable section ($0 < t < \tau$), and the

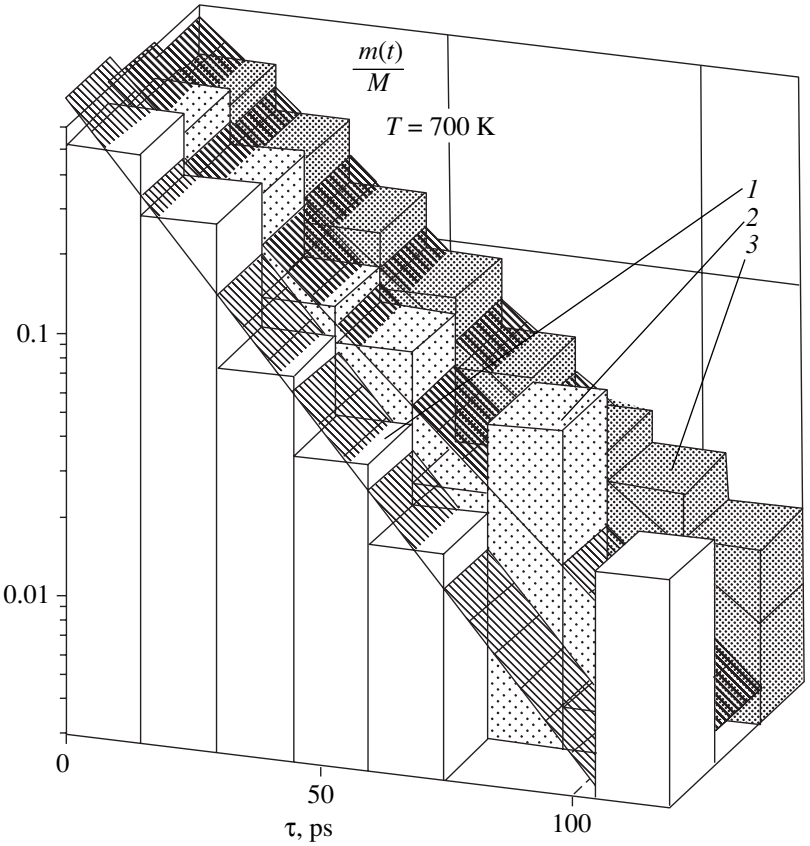

Fig. 3. Relative number $m(t)/M$ of the MD trajectories in the ensemble of M independent trajectories in which the cavitation onset time (lifetime τ_i) falls into the interval $(\tau, \tau + \Delta\tau)$. Calculations are performed for $T = 700$ K ($\Delta\tau = 15$ ps) and (*1*) $P = -3.95$ GPa, $M = 46$; (*2*) $P = -3.91$ GPa, $M = 232$; and (*3*) $P = -3.89$ GPa, $M = 142$. For comparison, dependences (2) obtained from the cavitation model considered as a random Poisson process are shown by straight lines.

vapor pressure in the critical bubble is negligible, $P' \ll P$. We used the experimental data concerning the surface tension of lead melt on the vaporization line [14]. The work for the formation of the critical nucleus and, as a consequence, the temperature and pressure dependences of the nucleation frequency depend strongly on the surface tension σ. Therefore, the spread of the experimental data is taken into account in the form of a confidence interval, $\sigma_{min} < \sigma < \sigma_{max}$, which is heuristically constructed using the uncertainty of the linear approximation of the experimental data into the range of high temperatures (see the insert in Fig. 4). Thus, for each temperature, the ranges $J(P; \sigma)$ and $\sigma_{min} < \sigma < \sigma_{max}$ are found from Eq. (3).

According to Fig. 4, the calculation data agree qualitatively with the CNT estimate, but the quantitative agreement decreases with an increase in temperature. In approach (3), the difference can be interpreted as a systematic underestimation of the work W for the formation of a critical nucleus. The discrepancy between the theoretical and calculation results can be decreased by taking into account the dependence of the surface tension on the degree of surface curvature (see, e.g., [1, 15]). In this case, the calculation result may indicate that the surface tension for critical-size bubbles is 5–10% larger than that for the flat interface. Note that a consistent comparison of the MD results with various CNT approximations must involve an independent determination of the temperature dependence of the surface tension on the liquid–gas curve in the framework of the same MD model. In spite of the reasonable agreement of the calculation data with the CNT approximation under consideration, the size of the critical nucleus is estimated in CNT as $N_n = \frac{\rho}{m}\frac{4\pi}{3}\left(\frac{2\sigma}{|P|}\right)^3 \approx$ 1 atom ($\rho/m = 2.82 \times 10^{28}$ m^{-3}, $T = 700$ K, $\sigma = 0.431$ N/m, and $P = -3.89$ GPa); i.e., the region under consideration is generally beyond the applicability limits of the macroscopic CNT approach.

In this study, cavitation has been considered only in terms of the homogeneous-nucleation processes in pure lead. The homogeneous-nucleation frequency is exponentially small far from the stability boundary of a metastable liquid, because the activation barrier of the spontaneous fluctuation formation of a cavity is high. In the practically important range of the operation parameters of power setups, cavitation in a heat carrier nec-

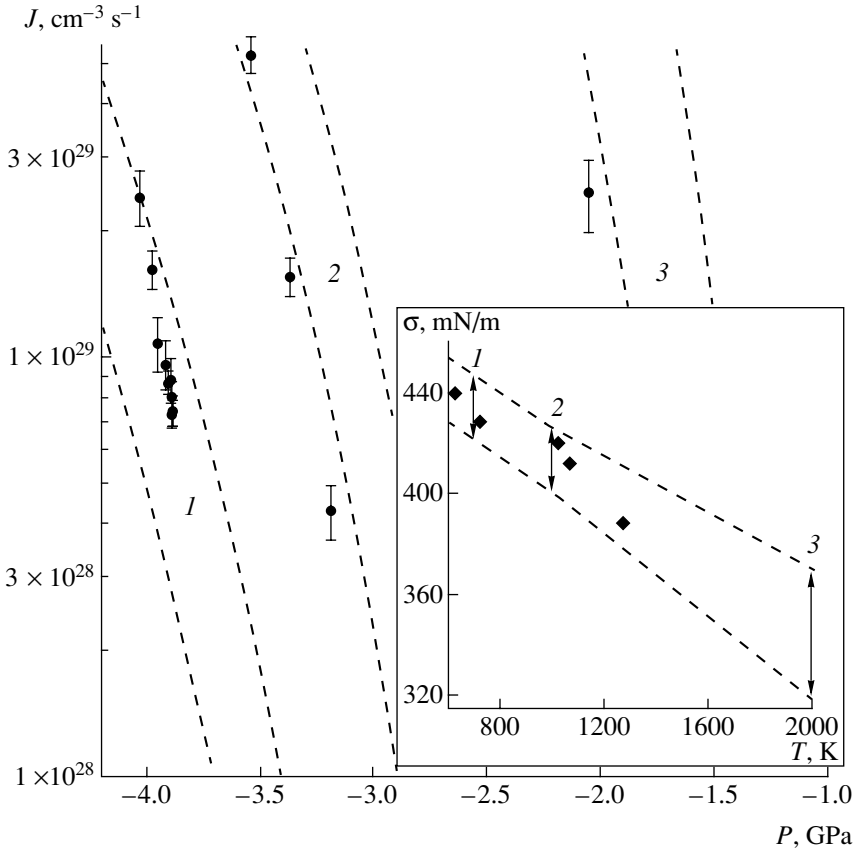

Fig. 4. Cavitation frequency J vs. pressure P along the three isotherms for T = (*1*) 700, (*2*) 1000, and (*3*) 2000 K. Calculation points are shown with error bars corresponding to the error of determining the mean lifetime. The dashed lines are the boundaries of the regions on the J–P plane, which correspond to the calculations by Eq. (3) for the above temperatures including the uncertainty of the surface tension σ for liquid lead. The insert shows the experimental σ values [14]; the dashed lines denote the region found from the error of the linear extrapolation of the experimental points; and the arrows correspond to the uncertainty of σ at fixed temperatures.

essarily occurs through the heterogeneous mechanism of nucleation on impurities and inhomogeneities (such as, e.g., lithium atoms in $Li_{17}Pb_{83}$ eutectic [5]). MD calculation of the heterogeneous cavitation rate is possible if an adequate model of interatomic interaction with impurity atoms is available.

ACKNOWLEDGMENTS

We are grateful to V.E. Fortov and S.A. Medin for their interest in this study and stimulating discussions, as well as to V.G. Baĭdakov and S.P. Protsenko, who kindly placed the data on the spinodal of the Lennard-Jones liquid at our disposal. The calculations were performed using a computer cluster presented by Deutscher Akademischer Austausch Dienst (DAAD, German Academic Exchange Service). This work was supported by the Division of Energetics, Mechanical Engineering, Mechanics, and Control Processes, Russian Academy of Sciences (program “Stability of Phase States and Critical Regimes of Heat and Mass Exchange”), the Presidium of the Russian Academy of Sciences (complex program “Thermal Physics and Mechanics of Intense Energy Actions”), and the Russian Foundation for Basic Research (project no. 04-02-17065-a). The work of V.V.S. was supported by the “Dynasty” Foundation.

REFERENCES

1. V. P. Skripov, *Metastable Liquid* (Nauka, Moscow, 1972) [in Russian].
2. T. Kinjo and M. Matsumoto, Fluid Phase Equilibria **144**, 343 (1998).
3. V. G. Baĭdakov and S. P. Protsenko, Dokl. Akad. Nauk **394** (6), 752 (2004) [Dokl. Phys. **49**, 69 (2004)].
4. G. E. Norman and V. V. Stegailov, Mol. Simul. **30**, 397 (2004).
5. S. A. Medin, Yu. N. Orlov, A. N. Parshikov, and V. M. Suslin, Preprint No. 41, IPM V. Keldysha RAN (Keldysh Institute of Applied Mathematics, Moscow, 2004).

6. A. Hassanein and I. Konkashbaev, Report No. ANL-ET-01-13, Argonne National Laboratory (2001).
7. H. S. Lim, C. K. Ong, and F. Ercolessi, Surf. Sci. **269**–**270**, 1109 (1992).
8. G. Bilalbegović and H. O. Lutz, Chem. Phys. Lett. **280**, 59 (1997).
9. A. A. Valuev, G. É. Norman, and V. Yu. Podlipchuk, in *Mathematical Simulation. Physicochemical Properties of Substances*, Ed. by A. A. Samarskiĭ and N. N. Kalitkin (Nauka, Moscow, 1989), pp. 5–40 [in Russian].
10. I. L. Iosilevskiĭ and A. Yu. Chigvintsev, http://zhurnal.ape.relarn.ru/articles/2003/003.pdf, pp. 21-34.
11. V. G. Baĭdakov and S. P. Protsenko, Dokl. Akad. Nauk **402** (6), 754 (2005) [Dokl. Phys. **50**, 303 (2005)].
12. V. Ya. Ternovoĭ, V. E. Fortov, S. V. Kvitov, and D. N. Nikolaev, *Shock Compression of Condensed Matter* (AIP, New York, 1995), Part 1, pp. 81–84.
13. M. Blander and J. L. Katz, AIChE J. **21**, 833 (1975).
14. A. P. Babichev, N. A. Babushkina, A. M. Bratkovskiĭ, *et al.*, *Physical Quantities: Handbook* (Énergoatomizdat, Moscow, 1991) [in Russian].
15. J. W. P. Schmelzer, I. Gutzow, and J. Schmelzer, J. Colloid Interface Sci. **178**, 657 (1996).

Translated by Yu. Vishnyakov

Doklady Physics, Vol. 50, No. 11, 2005, pp. 577–582. Translated from Doklady Akademii Nauk, Vol. 405, No. 3, 2005, pp. 332–337.

THEORETICAL PHYSICS

Singularities of Energy Surfaces under Non-Hermitian Perturbations

O. N. Kirillov, A. A. Mailybaev, and A. P. Seyranian

Presented by Academician S.S. Grigoryan May 20, 2005

Received May 23, 2005

In [1, 2], it was found that the energy surfaces of quantum systems can cross, forming a conic singularity, which is often called a diabolo and the apex of the cone is called the diabolic point [3]. The energy surfaces are mathematically described by the eigenvalues of real symmetric and Hermitian operators (Hamiltonians) depending on two or more parameters, and the diabolic point is characterized by a double eigenvalue corresponding to two linearly independent eigenvectors. In crystal optics, optical axes characterized by a coincidence of the refractive indices are analogs of diabolic points [4, 5]. In current problems of quantum physics, physical chemistry, crystal optics, and acoustics, it is important to know how the conic singularity of the energy surface is deformed under arbitrary complex perturbation, which describes dissipative and other nonconservative effects, with the formation of singularities corresponding to Jordan blocks [6–9].

In this work, we study singularities of the energy surfaces formed by the eigenvalues of the real symmetric and Hermitian matrices depending on parameters under arbitrary complex perturbation. Using the theory of eigenvalue bifurcations, which was developed in [10], we derive general asymptotic formulas describing the deformation of the energy surface near the conic singularity for various complex perturbations. The deformation of the eigenvalue surfaces appears to be described by the eigenvalues, eigenvectors, and derivatives of the Hamiltonian with respect to the parameters at the diabolic point. As an application, the singularities of the refractive-index surfaces in crystal optics are studied. Explicit expressions are obtained for these surfaces as functions of the properties of a crystal. Singular axes are found for crystals with weak absorption and optical activity. In terms of the components of the inverse dielectric tensor, we obtain a new condition that distinguishes crystals with prevailing absorption and with prevailing optical activity.

1. We consider the eigenvalue problem

$$\mathbf{Au} = \lambda\mathbf{u} \tag{1}$$

for an $m \times m$ Hermitian matrix $\mathbf{A}$, where λ is an eigenvalue, and $\mathbf{u}$ is an eigenvector. Such eigenvalue problems appear in reversible and irreversible physical systems without dissipation. These two cases correspond to real symmetric matrices and complex Hermitian matrices [9]. In quantum mechanics, $\mathbf{A}$, λ, and $\mathbf{u}$ correspond to the Hamiltonian, energy level, and vector of state, respectively. The matrix $\mathbf{A}$ is assumed to be a smooth function of the vector $\mathbf{p} = (p_1, p_2, \ldots, p_n)$ of n real parameters.

Let λ_0 be a double eigenvalue of the matrix $\mathbf{A}_0 = \mathbf{A}(\mathbf{p}_0)$ for a certain vector $\mathbf{p}_0$. Since $\mathbf{A}_0$ is a Hermitian matrix, the eigenvalue λ_0 is real and corresponds to two linearly independent eigenvectors $\mathbf{u}_1$ and $\mathbf{u}_2$. Thus, the point of interaction between two eigenvalues is diabolic. Let us take the normalized eigenvectors; i.e.,

$$(\mathbf{u}_1, \mathbf{u}_1) = (\mathbf{u}_2, \mathbf{u}_2) = 1, \quad (\mathbf{u}_1, \mathbf{u}_2) = 0, \tag{2}$$

where $(\mathbf{u}, \mathbf{v}) = \sum_{i=1}^{m} u_i \overline{v}_i$ is the scalar product of the vectors in C^m.

Under the perturbation of the parameters $\mathbf{p} = \mathbf{p}_0 + \Delta\mathbf{p}$, the double eigenvalue λ_0 is split into two single eigenvalues λ_+ and λ_-, which are determined by the asymptotic formula [10]

$$\lambda_\pm = \lambda_0 + \frac{\langle \mathbf{f}_{11} + \mathbf{f}_{22}, \Delta\mathbf{p}\rangle}{2} \pm \sqrt{\frac{\langle \mathbf{f}_{11} - \mathbf{f}_{22}, \Delta\mathbf{p}\rangle^2}{4} + \langle \mathbf{f}_{12}, \Delta\mathbf{p}\rangle \langle \mathbf{f}_{21}, \Delta\mathbf{p}\rangle}. \tag{3}$$

The components of the vector $\mathbf{f}_{ij} = (f_{ij}^1, f_{ij}^2, \ldots, f_{ij}^n)$ are given by the formula

$$f_{ij}^k = \left(\frac{\partial \mathbf{A}}{\partial p_k}\mathbf{u}_i, \mathbf{u}_j\right), \tag{4}$$

Institute of Mechanics, Moscow State University, Michurinskiĭ pr. 1, Moscow, 119192 Russia
e-mail: kirillov@imec.msu.ru, mailybaev@imec.msu.ru, seyran@imec.msu.ru

1028-3358/05/5011-0577$26.00

where the derivatives are calculated at the point $\mathbf{p}_0$ and $\langle \mathbf{a}, \mathbf{b} \rangle = \sum_{i=1}^{n} a_i \bar{b}_i$ is the scalar product of vectors in C^n. In Eq. (3), the terms $o(\|\Delta\mathbf{p}\|)$ and $o(\|\Delta\mathbf{p}\|^2)$ are omitted outside and inside the radicand, respectively. Since $\mathbf{A}$ is a Hermitian matrix, the eigenvalues $\mathbf{f}_{11}$ and $\mathbf{f}_{22}$ are real and vectors $\mathbf{f}_{12} = \bar{\mathbf{f}}_{21}$ are complex conjugate. The asymptotic expressions of the zeroth approximation for the eigenvectors $\mathbf{u}_\pm$ corresponding to the eigenvalues $\lambda_\pm$ have the form [10]

$$\mathbf{u}_\pm = \alpha_\pm \mathbf{u}_1 + \beta_\pm \mathbf{u}_2,$$
$$\frac{\alpha_\pm}{\beta_\pm} = \frac{\langle \mathbf{f}_{12}, \Delta\mathbf{p} \rangle}{\lambda_\pm - \lambda_0 - \langle \mathbf{f}_{11}, \Delta\mathbf{p} \rangle} = \frac{\lambda_\pm - \lambda_0 - \langle \mathbf{f}_{22}, \Delta\mathbf{p} \rangle}{\langle \mathbf{f}_{21}, \Delta\mathbf{p} \rangle}. \quad (5)$$

Let us consider an arbitrary complex perturbation of the family of matrices $\mathbf{A}(\mathbf{p}) + \Delta\mathbf{A}(\mathbf{p})$. Such perturbations appear due to nonconservative effects (such as dissipation), which violate the Hermiticity of the unperturbed problem [9]. Let us assume that the perturbation $\Delta\mathbf{A}(\mathbf{p}) \sim \varepsilon$ is small, where $\varepsilon = \|\Delta\mathbf{A}(\mathbf{p}_0)\|$ is the perturbation norm calculated at the diabolic point. The behavior of the eigenvalues $\lambda_\pm$ for small $\Delta\mathbf{p}$ and ε values is described by the asymptotic expressions [10]

$$\left(\lambda_\pm - \lambda_0 - \frac{\langle \mathbf{f}_{11} + \mathbf{f}_{22}, \Delta\mathbf{p} \rangle}{2} - \frac{\varepsilon_{11} + \varepsilon_{22}}{2}\right)^2$$
$$= \frac{(\langle \mathbf{f}_{11} - \mathbf{f}_{22}, \Delta\mathbf{p} \rangle + \varepsilon_{11} - \varepsilon_{22})^2}{4} \quad (6)$$
$$+ (\langle \mathbf{f}_{12}, \Delta\mathbf{p} \rangle + \varepsilon_{12})(\langle \mathbf{f}_{21}, \Delta\mathbf{p} \rangle + \varepsilon_{21}),$$

where

$$\varepsilon_{ij} = (\Delta\mathbf{A}(\mathbf{p}_0)\mathbf{u}_i, \mathbf{u}_j) \quad (7)$$

are small complex numbers on the order of ε. The small variation of the family of matrices provides a correction to the asymptotic expression for the eigenvectors $\mathbf{u}_\pm = \alpha_\pm^\varepsilon \mathbf{u}_1 + \beta_\pm^\varepsilon \mathbf{u}_2$, where

$$\frac{\alpha_\pm^\varepsilon}{\beta_\pm^\varepsilon} = \frac{\langle \mathbf{f}_{12}, \Delta\mathbf{p} \rangle + \varepsilon_{12}}{\lambda_\pm - \lambda_0 - \langle \mathbf{f}_{11}, \Delta\mathbf{p} \rangle - \varepsilon_{11}}$$
$$= \frac{\lambda_\pm - \lambda_0 - \langle \mathbf{f}_{22}, \Delta\mathbf{p} \rangle - \varepsilon_{22}}{\langle \mathbf{f}_{21}, \Delta\mathbf{p} \rangle + \varepsilon_{21}}. \quad (8)$$

We emphasize that $\alpha_+^\varepsilon/\beta_+^\varepsilon = \alpha_-^\varepsilon/\beta_-^\varepsilon$ at the point of the coincidence of the eigenvalues $\lambda_+ = \lambda_-$. Thus, at this point, the eigenvectors coincide, $\mathbf{u}_+ = \mathbf{u}_-$, and a Jordan block arises.

2. Let $\mathbf{A}(\mathbf{p})$ be the n-parametric family of real symmetric matrices. In this case, the vectors $\mathbf{f}_{11}$, $\mathbf{f}_{22}$, and $\mathbf{f}_{12} = \mathbf{f}_{21}$ are real and Eq. (3) assumes the form

$$\left(\lambda_\pm - \lambda_0 - \frac{\langle \mathbf{f}_{11} + \mathbf{f}_{22}, \Delta\mathbf{p} \rangle}{2}\right)^2$$
$$- \frac{\langle \mathbf{f}_{11} - \mathbf{f}_{22}, \Delta\mathbf{p} \rangle^2}{4} = \langle \mathbf{f}_{12}, \Delta\mathbf{p} \rangle^2. \quad (9)$$

This equation describes the surface consisting of two sheets $\lambda_+(\mathbf{p})$ and $\lambda_-(\mathbf{p})$ in the $(p_1, p_2, \ldots, p_n, \lambda)$ space. For the two-parametric matrix $\mathbf{A}(p_1, p_2)$, Eq. (9) determines a cone with a vertex at the point $(\mathbf{p}_0, \lambda_0)$ in the (p_1, p_2, λ) space [1, 2].

We consider the perturbation $\mathbf{A}(\mathbf{p}) + \Delta\mathbf{A}(\mathbf{p})$ of the real symmetric family $\mathbf{A}(\mathbf{p})$ near the diabolic point $\mathbf{p}_0$, where $\Delta\mathbf{A}(\mathbf{p})$ is a complex matrix with the small norm $\varepsilon = \|\Delta\mathbf{A}(\mathbf{p}_0)\|$. The splitting of the double eigenvalue λ_0 in the presence of the parameter change $\Delta\mathbf{p}$ and small complex perturbation $\Delta\mathbf{A}$ is described by Eq. (6), which assumes the form

$$\lambda_\pm = \lambda_0' + \mu \pm \sqrt{c}, \quad c = (x + \xi)^2 + (y + \eta)^2 - \zeta^2, \quad (10)$$

where

$$\lambda_0' = \lambda_0 + \frac{1}{2}\langle \mathbf{f}_{11} + \mathbf{f}_{22}, \Delta\mathbf{p} \rangle, \quad x = \frac{1}{2}\langle \mathbf{f}_{11} - \mathbf{f}_{22}, \Delta\mathbf{p} \rangle,$$
$$y = \langle \mathbf{f}_{12}, \Delta\mathbf{p} \rangle \quad (11)$$

are real and

$$\mu = \frac{1}{2}(\varepsilon_{11} + \varepsilon_{22}), \quad \xi = \frac{1}{2}(\varepsilon_{11} - \varepsilon_{22}),$$
$$\eta = \frac{1}{2}(\varepsilon_{12} + \varepsilon_{21}), \quad \zeta = \frac{1}{2}(\varepsilon_{12} - \varepsilon_{21}) \quad (12)$$

are small complex coefficients.

From Eqs. (10) and (11), we obtain the following expressions for the real and imaginary parts of the perturbed eigenvalues

$$\mathrm{Re}\lambda_\pm = \lambda_0' + \mathrm{Re}\mu \pm \sqrt{\frac{1}{2}(\mathrm{Re}c + \sqrt{\mathrm{Re}^2 c + \mathrm{Im}^2 c})}, \quad (13)$$

$$\mathrm{Im}\lambda_\pm = \mathrm{Im}\mu \pm \sqrt{\frac{1}{2}(-\mathrm{Re}c + \sqrt{\mathrm{Re}^2 c + \mathrm{Im}^2 c})}. \quad (14)$$

Equations (13) and (14) determine surfaces in the $(p_1, p_2, \ldots, p_n, \mathrm{Re}\lambda)$ and $(p_1, p_2, \ldots, p_n, \mathrm{Im}\lambda)$ spaces, respectively. Two sheets of the surface given by

Eq. (13) are joined ($\mathrm{Re}\lambda_+ = \mathrm{Re}\lambda_-$) at the points satisfying the conditions

$$\mathrm{Re}c \le 0, \quad \mathrm{Im}c = 0, \quad \mathrm{Re}\lambda_\pm = \lambda_0' + \mathrm{Re}\mu, \qquad (15)$$

and the sheets $\mathrm{Im}\lambda_+(\mathbf{p})$ and $\mathrm{Im}\lambda_-(\mathbf{p})$ are joined at the points of the set

$$\mathrm{Re}c \ge 0, \quad \mathrm{Im}c = 0, \quad \mathrm{Im}\lambda_\pm = \mathrm{Im}\mu. \qquad (16)$$

When the parameters are perturbed, the eigenvalues continue to be double under the condition $c = 0$, which provides the two equations $\mathrm{Re}c = 0$ and $\mathrm{Im}c = 0$. Depending on the sign of the quantity

$$D = \mathrm{Im}^2\zeta + \mathrm{Im}^2\eta - \mathrm{Im}^2\zeta, \qquad (17)$$

two cases can be realized. For $D > 0$, the equations $\mathrm{Re}c = 0$ and $\mathrm{Im}c = 0$ have the two solutions (x_a, y_a) and (x_b, y_b), where

$$x_{a,b} = -\mathrm{Re}\xi + \frac{\mathrm{Im}\xi\mathrm{Re}\zeta\mathrm{Im}\zeta}{\mathrm{Im}^2\xi + \mathrm{Im}^2\eta} \pm \frac{\mathrm{Im}\eta\sqrt{(\mathrm{Im}^2\xi + \mathrm{Im}^2\eta + \mathrm{Re}^2\zeta)D}}{\mathrm{Im}^2\xi + \mathrm{Im}^2\eta}, \qquad (18)$$

$$y_{a,b} = -\mathrm{Re}\eta + \frac{\mathrm{Im}\eta\mathrm{Re}\zeta\mathrm{Im}\zeta}{\mathrm{Im}^2\xi + \mathrm{Im}^2\eta} \mp \frac{\mathrm{Im}\xi\sqrt{(\mathrm{Im}^2\xi + \mathrm{Im}^2\eta + \mathrm{Re}^2\zeta)D}}{\mathrm{Im}^2\xi + \mathrm{Im}^2\eta}. \qquad (19)$$

These solutions determine the points in the parameter space at which double eigenvalues appear. For $D = 0$, the solutions coincide. For $D < 0$, the equations $\mathrm{Re}c = 0$ and $\mathrm{Im}c = 0$ have no real solutions. In this case, the eigenvalues λ_+ and λ_- are different for all $\Delta\mathbf{p}$ values.

We note that $\mathrm{Im}\xi$ and $\mathrm{Im}\eta$ are expressed in terms of the anti-Hermitian component $\Delta\mathbf{A}_N = \frac{1}{2}(\Delta\mathbf{A} - \overline{\Delta\mathbf{A}}^T)$ of the matrix $\Delta\mathbf{A}$ as

$$\mathrm{Im}\xi = \frac{(\Delta\mathbf{A}_N(\mathbf{p}_0)\mathbf{u}_1, \mathbf{u}_1) - (\Delta\mathbf{A}_N(\mathbf{p}_0)\mathbf{u}_2, \mathbf{u}_2)}{2i},$$
$$\mathrm{Im}\eta = \frac{(\Delta\mathbf{A}_N(\mathbf{p}_0)\mathbf{u}_1, \mathbf{u}_2) + (\Delta\mathbf{A}_N(\mathbf{p}_0)\mathbf{u}_2, \mathbf{u}_1)}{2i}, \qquad (20)$$

whereas $\mathrm{Im}\zeta$ is expressed in terms of the Hermitian component $\Delta\mathbf{A}_H = \frac{1}{2}(\Delta\mathbf{A} + \overline{\Delta\mathbf{A}}^T)$ as

$$\mathrm{Im}\zeta = \frac{(\Delta\mathbf{A}_H(\mathbf{p}_0)\mathbf{u}_1, \mathbf{u}_2) - (\Delta\mathbf{A}_H(\mathbf{p}_0)\mathbf{u}_2, \mathbf{u}_1)}{2i}. \qquad (21)$$

For $D > 0$, the effect of the anti-Hermitian part of perturbation $\Delta\mathbf{A}$ is stronger than that of the Hermitian part. If the Hermitian part prevails in perturbation $\Delta\mathbf{A}$, then $D < 0$. In particular, $D = -\mathrm{Im}^2\zeta < 0$ for pure Hermitian perturbation $\Delta\mathbf{A}$.

Let us assume that the vector $\mathbf{p}$ has only two components p_1 and p_2 and consider the surfaces given by Eqs. (13) and (14) for various perturbations $\Delta\mathbf{A}(\mathbf{p})$. First, we consider the case $D < 0$. Then, the eigenvalue surfaces $\mathrm{Re}\lambda_+(\mathbf{p})$ and $\mathrm{Re}\lambda_-(\mathbf{p})$ do not cross (Fig. 1a). The equation $\mathrm{Im}c = 0$ determines a straight line in the parameter plane. According to conditions (16), the sheets $\mathrm{Im}\lambda_+(\mathbf{p})$ and $\mathrm{Im}\lambda_-(\mathbf{p})$ of eigenvalue surfaces (14) cross along the straight line

$$\frac{1}{2}\mathrm{Im}c = (x + \mathrm{Re}\xi)\mathrm{Im}\xi + (y + \mathrm{Re}\eta)\mathrm{Im}\eta - \mathrm{Re}\zeta\mathrm{Im}\zeta = 0, \quad \mathrm{Im}\lambda_\pm = \mathrm{Im}\mu. \qquad (22)$$

For $D > 0$, the straight line $\mathrm{Im}c = 0$ contains the points $\mathbf{p}_a$ and $\mathbf{p}_b$, where the eigenvectors coincide. The coordinates of these points are determined from Eqs. (11), where $x = x_{a,b}$ and $y = y_{a,b}$ are given in Eqs. (18) and (19). According to Eqs. (15), the sheets of the real parts $\mathrm{Re}\lambda_+(\mathbf{p})$ and $\mathrm{Re}\lambda_-(\mathbf{p})$ of the eigenvalues are joined along the segment $[\mathbf{p}_a, \mathbf{p}_b]$ of the line

$$\frac{1}{2}\mathrm{Im}c = (x + \mathrm{Re}\xi)\mathrm{Im}\xi + (y + \mathrm{Re}\eta)\mathrm{Im}\eta - \mathrm{Re}\zeta\mathrm{Im}\zeta = 0, \quad \mathrm{Re}\lambda_\pm = \lambda_0' + \mathrm{Re}\mu. \qquad (23)$$

The singularity of the surface of the real parts of the eigenvalues described by Eq. (13) for $D > 0$ is called a "coffee filter" [8]. The deformation of the conic singularity to the coffee filter is shown in Fig. 1b. In the optics and acoustics of crystals, the segment $[\mathbf{p}_a, \mathbf{p}_b]$ is called the branch cut, and the points $\mathbf{p}_a$ and $\mathbf{p}_b$ determine "singular axes," because, according to Eq. (8), each double eigenvalue at these points corresponds to only one eigenvector [4, 5, 7].

3. The optical properties of a nonmagnetic crystal are characterized by the inverse dielectric tensor $\boldsymbol{\eta}$, which relates the electric field strength $\mathbf{E}$ and electric displacement $\mathbf{D}$ [4]

$$\mathbf{E} = \boldsymbol{\eta}\mathbf{D}. \qquad (24)$$

For a monochromatic plane wave propagating with frequency ω in the direction $\mathbf{s} = (s_1, s_2, s_3)$, $\|\mathbf{s}\| = 1$, we have

$$\mathbf{D}(\mathbf{r}, t) = \mathbf{D}(\mathbf{s})\exp i\omega\left(\frac{n(\mathbf{s})}{c}\mathbf{s}^T\mathbf{r} - t\right), \qquad (25)$$

where $n(\mathbf{s})$ is the refractive index, and $\mathbf{r}$ is the real vector of the spatial coordinates. In view of Eq. (25) for the wave and Eq. (24), Maxwell equations are transformed to the form

$$\boldsymbol{\eta}\mathbf{D}(\mathbf{s}) - \mathbf{s}\mathbf{s}^T\boldsymbol{\eta}\mathbf{D}(\mathbf{s}) = \frac{1}{n^2(\mathbf{s})}\mathbf{D}(\mathbf{s}). \qquad (26)$$

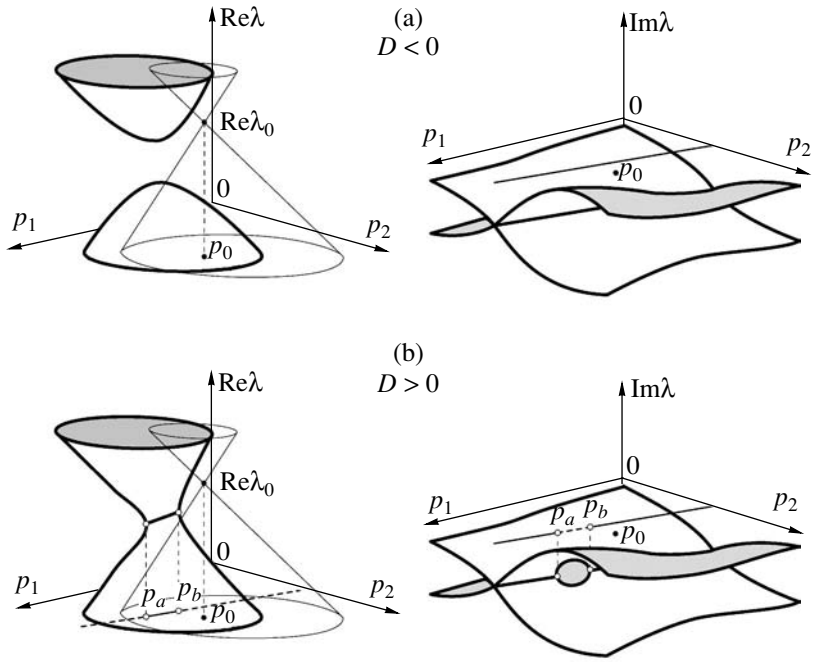

Fig. 1. Unfolding of a conic singularity under complex perturbation.

Multiplying Eq. (26) by the vector $\mathbf{s}^T$ from the left, we find that the vector $\mathbf{D}$ for a plane wave is always orthogonal to the direction vector $\mathbf{s}$; i.e., $\mathbf{s}^T\mathbf{D}(\mathbf{s}) = 0$. Using this condition, we represent Eq. (26) in the form of the eigenvalue problem

$$[(\mathbf{I} - \mathbf{s}\mathbf{s}^T)\boldsymbol{\eta}(\mathbf{I} - \mathbf{s}\mathbf{s}^T)]\mathbf{u} = \lambda\mathbf{u}, \tag{27}$$

where $\lambda = n^{-2}$, $\mathbf{u} = \mathbf{D}$, and $\mathbf{I}$ is the identity matrix. Since $\mathbf{I} - \mathbf{s}\mathbf{s}^T$ is a singular matrix, one eigenvalue is always equal to zero. We denote the other two eigenvalues as λ_+ and λ_-. These eigenvalues determine the refractive index n, and the corresponding eigenvectors determine the polarization [4].

The inverse dielectric tensor is described by the complex non-Hermitian matrix $\boldsymbol{\eta} = \boldsymbol{\eta}_{\text{transp}} + \boldsymbol{\eta}_{\text{dichroic}} + \boldsymbol{\eta}_{\text{chiral}}$. The symmetric part of the matrix $\boldsymbol{\eta}$ consists of the real matrix $\boldsymbol{\eta}_{\text{transp}}$ and imaginary matrix $\boldsymbol{\eta}_{\text{dichroic}}$ and forms the anisotropy tensor describing the birefringence of the crystal. For a transparent crystal, the anisotropy tensor is real and consists only of the matrix $\boldsymbol{\eta}_{\text{transp}}$. For a crystal with linear dichroism, this tensor is represented by a complex matrix. Choosing the coordinate axes along the principal axes of the matrix $\boldsymbol{\eta}_{\text{transp}}$, we obtain $\boldsymbol{\eta}_{\text{transp}} = \text{diag}(\eta_1, \eta_2, \eta_3)$. The matrix

$$\boldsymbol{\eta}_{\text{dichroic}} = i\begin{pmatrix} \eta_{11}^d & \eta_{12}^d & \eta_{13}^d \\ \eta_{12}^d & \eta_{22}^d & \eta_{23}^d \\ \eta_{13}^d & \eta_{23}^d & \eta_{33}^d \end{pmatrix} \tag{28}$$

describes linear dichroism (absorption). The matrix $\boldsymbol{\eta}_{\text{chiral}}$ is the antisymmetric part of $\boldsymbol{\eta}$. It is determined by the optical activity vector $\mathbf{g} = (g_1, g_2, g_3)$ of the crystal, which depends linearly on $\mathbf{s}$:

$$\boldsymbol{\eta}_{\text{chiral}} = i\begin{pmatrix} 0 & -g_3 & g_2 \\ g_3 & 0 & -g_1 \\ -g_2 & g_1 & 0 \end{pmatrix},$$
$$\mathbf{g} = \boldsymbol{\gamma}\mathbf{s} = \begin{pmatrix} \gamma_{11} & \gamma_{12} & \gamma_{13} \\ \gamma_{12} & \gamma_{22} & \gamma_{23} \\ \gamma_{13} & \gamma_{23} & \gamma_{33} \end{pmatrix}\begin{pmatrix} s_1 \\ s_2 \\ s_3 \end{pmatrix}, \tag{29}$$

where $\boldsymbol{\gamma}$ is the symmetric optical-activity tensor [4, 5].

First, we consider a transparent crystal for which $\boldsymbol{\eta}_{\text{dichroic}} = \boldsymbol{\gamma} = 0$. In this case, the matrix

$$\mathbf{A}(\mathbf{p}) = (\mathbf{I} - \mathbf{s}\mathbf{s}^T)\boldsymbol{\eta}_{\text{transp}}(\mathbf{I} - \mathbf{s}\mathbf{s}^T) \tag{30}$$

is real and symmetric and depends on the two-component vector $\mathbf{p} = (s_1, s_2)$. The third component of the vector $\mathbf{s}$ is represented as $s_3 = \pm\sqrt{1 - s_1^2 - s_2^2}$, where the cases of two different signs should be analyzed separately. In what follows, we assume that $\eta_1 > \eta_2 > \eta_3$, which corresponds to a biaxial crystal.

Nonzero eigenvalues $\lambda_\pm$ of the matrix $\mathbf{A}(\mathbf{p})$ are found in an explicit form and are identical for opposite

directions **s** and –**s**. The eigenvalues λ_+ and λ_- coincide at the points

$$\mathbf{s}_0 = (S_1, 0, S_3)^T, \quad \lambda_0 = \eta_2;$$
$$S_1 = \pm\sqrt{\frac{\eta_1 - \eta_2}{\eta_1 - \eta_3}}, \quad S_3 = \pm\sqrt{1 - S_1^2}, \tag{31}$$

which determine four diabolic points (for two signs of S_1 and S_3), the latter also being called optical axes [4, 5]. A double eigenvalue $\lambda_0 = \eta_2$ of the matrix $\mathbf{A}_0 = \mathbf{A}(\mathbf{p}_0)$, where $\mathbf{p}_0 = (S_1, 0)$, corresponds to two eigenvectors

$$\mathbf{u}_1 = (0, 1, 0)^T, \quad \mathbf{u}_2 = (S_3, 0, -S_1)^T, \tag{32}$$

which satisfy normalization conditions (2). Using Eqs. (30) and (32), we find the vectors $\mathbf{f}_{ij}$ with components (4) for the optical axes. Substituting them into Eq. (9), we obtain the following local asymptotic expressions for conic singularities in the (s_1, s_2, λ) space, which are valid for each of the four optical axes (31):

$$(\lambda - \eta_2 - (\eta_3 - \eta_1)S_1(s_1 - S_1))^2$$
$$= (\eta_3 - \eta_1)^2 S_1^2((s_1 - S_1)^2 + S_3^2 s_2^2). \tag{33}$$

Let us assume that the crystal is absorptive and optically active. In this case, one can suppose that the family of matrices given by Eq. (30) undergoes complex perturbation $\mathbf{A}(\mathbf{p}) + \Delta\mathbf{A}(\mathbf{p})$, where

$$\Delta\mathbf{A}(\mathbf{p}) = (\mathbf{I} - \mathbf{s}\mathbf{s}^T)(\boldsymbol{\eta}_{\text{dichroic}} + \boldsymbol{\eta}_{\text{chiral}})(\mathbf{I} - \mathbf{s}\mathbf{s}^T). \tag{34}$$

Let us assume that the absorption and optical activity are weak; i.e., the quantity $\varepsilon = \|\boldsymbol{\eta}_{\text{dichroic}}\| + \|\boldsymbol{\eta}_{\text{chiral}}\|$ is small. In this case, the above general asymptotic formulas can be used to describe the rearrangement of the conic singularity of the eigenvalue surface. To this end, it is only necessary to know perturbation $\Delta\boldsymbol{A}$ on the optical axis $\mathbf{s}_0$ of the transparent crystal. Substituting matrix (34), calculated on optical axis (31), into Eq. (7) and using Eq. (12), we obtain

$$\mu = \frac{i}{2}(\eta_{22}^d + \eta_{11}^d S_3^2 - 2\eta_{13}^d S_1 S_3 + \eta_{33}^d S_1^2),$$
$$\xi = \frac{i}{2}(\eta_{22}^d - \eta_{11}^d S_3^2 + 2\eta_{13}^d S_1 S_3 - \eta_{33}^d S_1^2),$$
$$\eta = i(\eta_{12}^d S_3 - \eta_{23}^d S_1), \tag{35}$$
$$\zeta = -i(\gamma_{11} S_1^2 + 2\gamma_{13} S_1 S_3 + \gamma_{33} S_3^2).$$

We note that μ, ξ, and η are imaginary and depend only on absorption and that ζ depends on the optical activity of the crystal.

Singularities in crystals with weak absorption and optical activity were studied in [5]. It was shown that the coffee filter singularity appears in crystals with prevailing absorption and that the surfaces of the real parts of eigenvalues for crystals with dominant optical activity do not cross. According to the above general results, these two cases correspond to the conditions $D > 0$ and $D < 0$, where D is given by Eq. (17).

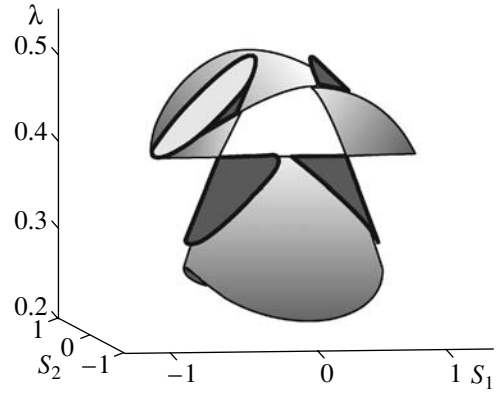

Fig. 2. Conical singularities on optic axes and their local approximations.

As a numerical example, we analyze a crystal with weak absorption and optical activity, which is described by tensors (28) and (29), where

$$\boldsymbol{\eta}_{\text{dichroic}} = \frac{i}{200}\begin{pmatrix} 3 & 2 & 0 \\ 2 & 3 & 1 \\ 0 & 1 & 3 \end{pmatrix}, \quad \gamma = \frac{1}{200}\begin{pmatrix} 3 & 1 & 2 \\ 1 & 3 & 1 \\ 2 & 1 & 3 \end{pmatrix}. \tag{36}$$

The corresponding transparent crystal is characterized by the parameters $\eta_1 = 0.5$, $\eta_2 = 0.4$, and $\eta_3 = 0.1$, and its eigenvalue surfaces with two optical axes are shown in Fig. 2 along with conical surfaces (33). Two optical axes shown in Fig. 2 have the coordinates $\mathbf{s}_0 = \left(\pm\frac{1}{2}, 0, \frac{\sqrt{3}}{2}\right)$ and correspond to the double eigenvalue $\lambda_0 = \frac{2}{5}$. Using Eqs. (36) in Eq. (35), we conclude that the condition $D = \frac{7}{160\,000}(4\sqrt{3} - 5) > 0$ is satisfied for the left optical axis $\mathbf{s}_0 = \left(-\frac{1}{2}, 0, \frac{\sqrt{3}}{2}\right)$. Therefore, the conic singularity is transformed into the coffee filter with two singular axes. The local approximation of these surfaces is given by Eqs. (13) and (14). On the right optical axis $\mathbf{s}_0 = \left(\frac{1}{2}, 0, \frac{\sqrt{3}}{2}\right)$, the condition $D = -\frac{7}{160\,000}(4\sqrt{3} + 5) < 0$ is satisfied. Thus, the real parts of eigenvalues do not coincide under a perturbation of

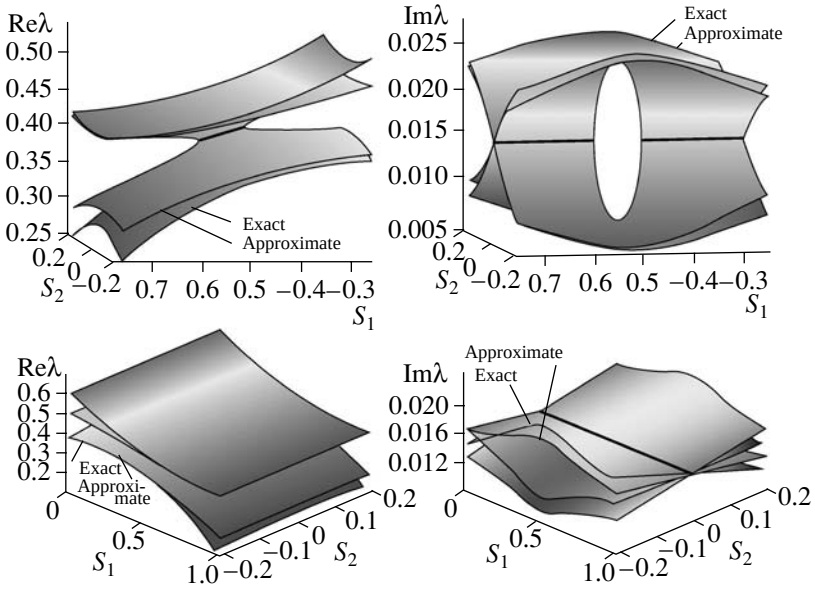

Fig. 3. Refractive-index surfaces for a crystal with weak absorption and optical activity.

the right optical axis. The approximate and exact eigenvalue surfaces are shown in Fig. 3, where it is seen that asymptotic formulas well reproduce the singularities of the refractive-index surfaces of crystals with weak absorption and optical activity.

ACKNOWLEDGMENTS

This work was supported by the Russian Foundation for Basic Research (project no. 03-01-00161) and the Basic Research and Higher Education Program, the U.S. Civilian Research and Development Foundation (grant nos. Y1-M-06-03 and Y1-MP-06-19).

REFERENCES

1. J. Von Neumann and E. P. Wigner, Z. Phys. **30**, 467 (1929).
2. E. Teller, J. Phys. Chem. **41** (1), 109 (1937).
3. M. V. Berry and M. Wilkinson, Proc. R. Soc. London, Ser. A **392**, 15 (1984).
4. L. D. Landau, E. M. Lifshitz, and L. P. Pitaevskiĭ, *Electrodynamics of Continuous Media* (Fizmatlit, Moscow, 2003; Pergamon, New York, 1984).
5. M. V. Berry and M. R. Dennis, Proc. R. Soc. London, Ser. A **459**, 1261 (2003).
6. A. Mondragon and E. Hernandez, J. Phys. A **26**, 5595 (1993).
7. A. L. Shuvalov and N. H. Scott, Acta Mech. **140**, 1 (2000).
8. F. Keck, H. J. Korsch, and S. Mossmann, J. Phys. A **36**, 2125 (2003).
9. M. V. Berry, Czech. J. Phys. **54**, 1039 (2004).
10. A. P. Seyranian, O. N. Kirillov, and A. A. Mailybaev, J. Phys. A **38**, 1723 (2005).

Translated by R. Tyapaev

Doklady Physics, Vol. 50, No. 11, 2005, pp. 583–587. Translated from Doklady Akademii Nauk, Vol. 405, No. 1, 2005, pp. 46–50.

MECHANICS

Problem of the Flow around a Jet Source

N. B. Il'inskiy and R. F. Mardanov

Presented by Academician G.G. Chernyĭ July 4, 2005

Received April 18, 2005

The problem of the steady plane-parallel flow of an ideal incompressible fluid around a point jet source, i.e., a source from which a fluid with the parameters (density and total pressure) different from the respective free-flow parameters is blown in the presence of a dead zone near the flow separation point, has been solved. The necessity of solving this problem arises in connection with the study of jet collision problems. The solution to similar problems for the case in which the parameters of the fluids in the jet and free flow are the same can be found in [1, 2]. If the parameters of the jets are different, the solution of the problem is complicated, because the complex potential function has a discontinuity at the interface between the media and a rather complex iteration process is necessary for determining this interface. The authors of [3] analyzed the problem of the collision of jets that have different Bernoulli constants and flow around a wedge with angle $\alpha\pi$, but the case of $\alpha = 1$ was excluded from the analysis, because an essential singularity arises near the flow separation point. In this case, in view of the equality condition for pressures, the angle internal to one of the jets vanishes; i.e., a return-type singular point appears at the boundary of this jet.

It is only in [4] that we find a problem in which such a singularity has not been excluded from the solution. In that work, a solution was provided to the problem of the flow of the ideal incompressible fluid around the point source from which fluid with the Bernoulli constant different from the Bernoulli constant of the external flow is blown and the flow separation point is a singular point. Integral formulas for obtaining the exact solution were derived, but the numerical realization was performed with simplifications that made it possible to simulate the flow near the flow separation point.

In this work, the problem of the flow around the jet source is also solved, but we introduce a dead zone with constant velocities at the boundary into the model of the flow near the flow separation point. The introduction of this condition enables us to overcome difficulties associated with the aforementioned singularity and to perform numerical calculations without additional simplifications. The piecewise analytic function of the complex potential and unknown interface between the media were determined by the iteration method. The conditions of the solvability of the problem are satisfied by fitting the parameters in the additional plane. A series of calculations is performed for various parameters of the problem. The results are compared with the results obtained by the method described in [4], as well as with the limiting cases, which are written in the analytical form. The calculation results are analyzed and conclusions are made.

FORMULATION OF THE PROBLEM

In the physical plane $z = x + iy$ (Fig. 1), the point source M with given rate Q is streamed by a steady plane-parallel flow of an ideal incompressible fluid with density ρ and velocity V_∞ at infinity. The coordinate origin is placed at the point M and the abscissa axis

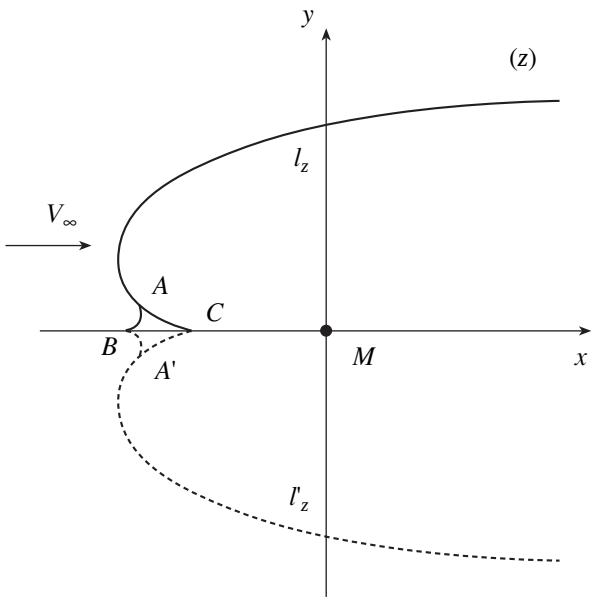

Fig. 1. Physical z plane.

Chebotarev Research Institute of Mathematics and Mechanics, Kazan State University, ul. Universitetskaya 17, Kazan, 420008 Russia
e-mail: renat.mardanov@ksu.ru

1028-3358/05/5011-0583$26.00

is directed along the free-flow velocity. A fluid is blown from the source with density ρ_j and velocity $V_{\infty j}$ in the jet at infinity, which are different from the respective parameters of the external flow. The subscript j denotes the jet parameters. In this case, the dimensionless parameter $\mu = \frac{\rho_j V_{\infty j}^2}{\rho V_\infty^2} - 1$ characterizes the energy of the blown fluid ($0 \le \mu \le \infty$). The l_z and l_z' interfaces of the media are the lines of the tangential velocity jump that is determined by the formula

$$\rho_j V_j^2 = \rho V^2 + \mu\rho V_\infty^2, \quad (1)$$

which follows from the Bernoulli integral. A dead zone (pillar) with constant velocities at the boundary is introduced into the flow model near the flow separation point. Velocity V_0 is specified in the section $A'BA$ and velocity V_{0j}, which is related to V_0 by Eq. (1), is specified in the section $A'CA$.

It is necessary to determine the shape of the l_z and l_z' interfaces of the media, as well as the shape and position of the pillar $BACA'$, and to analyze the effect of the parameter V_0 on the solution of the problem.

SOLUTION

Since the flow is symmetric, it is sufficient to consider only the upper half of the flow. Let us consider an auxiliary plane $t = \tau + i\eta$ whose upper half-plane G_t corresponds to the domain G_z of the flow in the physical plane z (upper half-plane without the pillar). The corresponding points are denoted by the same letters. For the one-to-one mapping between G_z and G_t, we assume that there exists a correspondence between the infinite points of these domains and the mapping of the point $z = 0$ to the point $t = 0$ and the point $z = z_a$ to the point $t = -1$, where z_a is the coordinate of the point A in the z plane. Let b and c be the coordinates of the points B and C in the t plane: $b < -1$ and $-1 < c < 0$, and let l_t be the image of the line l_z in the auxiliary plane.

Under the above assumptions, complex potentials of the flows exist in the external flow and jet. We consider these potentials as a single piecewise analytic function $w(z) = \varphi(x, y) + i\psi(x, y)$, which is discontinuous at the interface between the media. The complex conjugate velocity in the t plane is represented as

$$\frac{dw}{dt} = u_\infty \exp[-\Omega(t)]\frac{t+1}{t}, \quad (2)$$

where u_∞ is the velocity of the free flow in the t plane and $\Omega(t) = T(\tau, \eta) + i\Lambda(\tau, \eta)$ is a piecewise analytic function with a discontinuity on the line l_t.

For a point $\zeta(\sigma)$ on the line l_t with an arc abscissa σ measured from the point A ($\sigma \ge 0$) and the tangent slope angle $\vartheta(\sigma)$ to l_t at this point, there is the relation

$$d\zeta = \exp[i\vartheta(\sigma)]d\sigma. \quad (3)$$

Considering Eq. (2) on the line l_t and taking into account that this line is impermeable, we arrive at the relation

$$\vartheta(\sigma) = \Lambda(\sigma) - \arg\frac{\zeta+1}{\zeta}, \quad (4)$$

i.e., only $T(\sigma) = \mathrm{Re}(\Omega(\zeta))$ has a jump. Taking into account that the real axis τ is also a streamline and substituting $t = \tau$ into Eq. (2), we obtain

$$\Lambda(\tau) \equiv 0. \quad (5)$$

Let $\chi(t) = \ln\frac{dw}{dz} = S - i\theta$ be the Michell–Joukowski function. Here, $S = \ln|V|$, V is the absolute value of the velocity, and θ is the argument of the velocity in the physical z plane. We consider the function

$$\tilde{\chi}(t) = \chi(t) - \chi_0(t) + \Omega(t) = \tilde{S} + i\tilde{\theta}, \quad (6)$$

where $\chi_0(t) = S_0 + i\theta_0$ is the function with a singularity at point M. We specify $\theta_0(\tau)$ on the real axis so that $\tilde{\theta}(\tau) = -\theta(\tau) - \theta_0(\tau) \equiv 0$ for $\tau \in (-\infty, b] \cup [c, \infty)$:

Section	$(-\infty; b]$	$[b; c]$	$[c; 0]$	$[0; \infty)$
$\theta_0(\tau)$	0	$-\pi(\tau - b)/(c - b)$	$-\pi$	0

The function $\chi_0(t)$ is determined by solving the Schwarz problem for the upper half-plane and finding an arbitrary constant from the condition $\chi_0(\infty) = 0$:

$$\chi_0(t) = \frac{t-b}{c-b}\ln(t-b) - \frac{t-c}{c-b}\ln(t-c) - \ln t - 1. \quad (7)$$

Then, from Eq. (6) we obtain

$$\frac{dw}{dz} = \exp[\tilde{\chi} + \chi_0 - \Omega] \quad (8)$$

and, taking into account Eq. (2), arrive at the relation

$$\frac{dz}{dt} = \frac{dw/dt}{dw/dz} = u_\infty\frac{t+1}{t}\exp[-\tilde{\chi} - \chi_0]. \quad (9)$$

Since the left-hand side of this equality is an analytic function, the function $\tilde{\chi}(t)$ on the right-hand side is also analytic. According to Eq. (6), the jumps of the func-

tions $\chi(t)$ and $\Omega(t)$ cancel each other out. Taking into account Eq. (8), we denote the jump functions as

$$\lambda(\sigma) = T(\sigma) - T_j(\sigma) = \ln\frac{V_j(\sigma)}{V(\sigma)}, \quad (10)$$

where the velocities V and V_j are related through Eq. (1). If the function $\lambda(\sigma)$ is known, taking into account Eq. (5), we obtain the function Ω in the form

$$\Omega(t) = \Phi(t) + \overline{\Phi(\bar{t})}, \quad \Phi(t) = \frac{1}{2\pi i}\int_{l_t}\frac{\lambda(\zeta)d\zeta}{\zeta - t}. \quad (11)$$

Separating the real part in Eq. (6) for $t = \tau$, we arrive at the relation

$$\tilde{S}(\tau) = \ln|V(\tau)| - S_0(\tau) + T(\tau), \quad (12)$$

where

$$S_0(\tau) = \frac{\tau - b}{c - b}\ln|\tau - b| - \frac{\tau - c}{c - b}\ln|\tau - c| - \ln|\tau| - 1,$$

according to Eq. (7). Since $V(\tau)$ (velocity at the boundary of the pillar) is specified in the section $[b, c]$ and, therefore, the function $\tilde{S}(\tau)$ is known, whereas $\tilde{\theta}(\tau) \equiv 0$ in the remaining sections of the real axis, the function $\tilde{\chi}(t)$ is determined as the solution of the mixed problem

$$\tilde{\chi}(t) = -\frac{R(t)}{\pi}\int_b^c\frac{\tilde{S}(\tau)}{|R(\tau)|}\frac{d\tau}{\tau - t}, \quad (13)$$

where $R(t) = \sqrt{(t-b)(t-c)}$ is taken as the branch positive in the region $\tau > c$. The solvability condition

$$\tilde{S}_\infty = \frac{1}{\pi}\int_b^c\frac{\tilde{S}(\tau)}{|R(\tau)|}d\tau \quad (14)$$

for the mixed problem is used to determine the function $\tilde{S}(\tau)$ at infinity.

The shapes of the pillar boundary BAC and line l_z are determined by integrating Eq. (9) as

$$z(t) = \int_0^t\frac{dz}{dt}dt.$$

The found solution should naturally be matched with the asymptotic value

$$y_\infty = \frac{Q}{2V_{\infty j}} \quad (15)$$

of the line l_z at infinity.

SCHEME OF THE ITERATION PROCESS

The iteration process is necessary for finding unknown functions $\lambda(\sigma)$ and $\vartheta(\sigma)$. In view of Eq. (1), the functions $\lambda(\sigma)$ and $\vartheta(\sigma)$ should satisfy the conditions

$$\lambda(0) = \lambda_0 = \frac{1}{2}\ln\left[\frac{\rho}{\rho_j}\left(1 + \mu\frac{V_\infty^2}{V_0^2}\right)\right],$$

$$\lambda(\infty) = \lambda_\infty = \frac{1}{2}\ln\left[\frac{\rho}{\rho_j}(1 + \mu)\right],$$

$$\vartheta(0) = \vartheta_0 = \frac{\pi}{2}, \quad \vartheta(\infty) = \vartheta_\infty = 0.$$

As the initial approximation for them, we can take

$$\lambda^{(0)}(\sigma) = \lambda_0 + \gamma(\sigma)(\lambda_\infty - \lambda_0),$$

$$\vartheta^{(0)}(\sigma) = \vartheta_0 + \gamma(\sigma)(\vartheta_\infty - \vartheta_0),$$

where

$$\gamma(\sigma) = \frac{2}{\pi}\arctan(C\sigma), \quad C > 0.$$

The iteration procedure consists of the following steps:

(i) the line l_t is found by integrating Eq. (3);

(ii) $T(\tau) = \mathrm{Re}(\Omega(\tau))$ on the real axis and $\Omega(\zeta)$ on the line l_t are determined by Eq. (11);

(iii) solving mixed problem (13) with $\tilde{S}(\tau)$ given by Eq. (12), we determine the function $\tilde{\chi}(\zeta)$ on the line l_t;

(iv) $V(\sigma) = \left|\frac{dw}{dz}\right|_{t=\zeta}$ is found from Eq. (8) and $V_j(\sigma)$ is obtained using Eq. (1);

(v) new approximations for the functions $\lambda(\sigma)$ and $\vartheta(\sigma)$ are determined by Eqs. (10) and (4), respectively.

The iteration process should be continued until the attainment of condition

$$\max_\sigma\left|\vartheta^{(n)}(\sigma) - \vartheta^{(n-1)}(\sigma)\right| < \varepsilon,$$

$$\max_\sigma\left|\lambda^{(n)}(\sigma) - \lambda^{(n-1)}(\sigma)\right| < \varepsilon,$$

where ε is a certain small positive number.

SOLVABILITY CONDITIONS

The problem of determining the pillar shape is an inverse problem. For this reason, as in the inverse

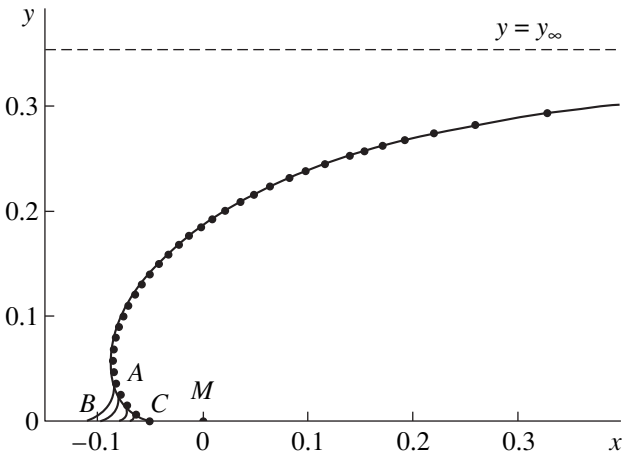

Fig. 2. Calculation results for various V_0 values.

boundary value problem of aerohydrodynamics (see, e.g., [5]), the solvability conditions should be satisfied. Considering Eq. (8) for $t \longrightarrow \infty$, we obtain the condition that the velocity determined at infinity coincides with the preset value in the form $\ln V_\infty = \tilde{S}_\infty$, where $\tilde{S}_\infty$ is determined by Eq. (14). The condition of the closeness of the pillar is found from the equation

$$\operatorname*{res}_{t\to\infty}\frac{dz}{dt} = 0$$

and has the form

$$a - 1 - \frac{1}{2}(b + c)(1 + \tilde{S}_\infty) = 0,$$

where

$$a = \frac{1}{\pi}\int_b^c \frac{\tilde{S}(\tau)\tau}{|R(\tau)|}d\tau.$$

These solvability conditions are satisfied by fitting the parameters b and c. To determine the velocity u_∞, we use the condition that the rate Q is given. Using the relation $\left.\frac{dw}{dz}\right|_{z\to 0} \sim \frac{Q}{2\pi z}$ and Eqs. (8) and (9), we arrive at the relation $Q = 2\pi u_\infty \exp[-T(0)]$ between Q and u_∞.

Thus, in addition to the internal iteration process for determining the functions $\lambda(\sigma)$ and $\vartheta(\sigma)$, we organize the external iteration process for finding the parameters b, c, and u_∞ on the basis of the Newton method for solving systems of nonlinear equations.

LIMITING CASES

To test the resulting numerical–analytical solution, it is convenient to use the limiting cases of the problem under consideration, in which the solutions are obtained in the analytical form.

Case μ = 0. This is the case of the flow of the ideal incompressible fluid around the usual point source. The complex potential for such a flow has the form

$$w(z) = V_\infty z + \frac{Q}{2\pi}\ln z + C_1.$$

From this formula, it is easy to obtain the following equation for determining the line l_z:

$$z(\delta) = -\frac{Q\delta e^{-i\delta}}{2\pi V_\infty \sin\delta},$$

where the parameter δ ranges from 0 to π. The coordinate of the flow separation point A has the form $z_a = -\frac{Q}{2\pi V_\infty}$.

Case μ = ∞. In this case, the velocity V_j at the boundary of the jet is a certain arbitrary constant V_1. This problem is easily solved by the velocity hodograph method (see, e.g., [1]). The resulting formula for determining the line l_z has the form

$$z(s) = z_a + \frac{Q}{\pi V_1}\left[\frac{1}{1 + i\sqrt{s}} + \ln(1 + i\sqrt{s}) - 1\right],$$

where the parameter s ranges from 0 to ∞ and $z_a = \frac{(1 - 2\ln 2)Q}{2\pi V_1}$ is the coordinate of the flow separation point A. We emphasize that the ratio $\frac{Q}{2V_1}$ in this case is the asymptotic value y_∞ of the jet boundary at infinity.

CALCULATION RESULTS

We perform calculations with the parameters $V_\infty = \rho = \rho_j = 1$. In the first series of calculations, we analyze the dependence of the solution on the velocity V_0, which is a parameter of the problem. Figure 2 shows the shape of the pillar and interface between the media for $Q = 1$, $\mu = 1$, and $V_0 = 0.1$, 0.05, 0.01, and 0.001. The size of the pillar decreases with the velocity V_0, but the shape of the section AC, which is streamed by the jet from the source, remains almost unchanged. The shape of the line l_z is also almost independent of V_0. It can be assumed with great certainty that the interface between the media that is obtained by solving the problem without the introduction of the dead zone is close to the line l_z, which is obtained above and is unified with the section AC of the pillar. For comparison, points show the shape of the interface between the media, as found by

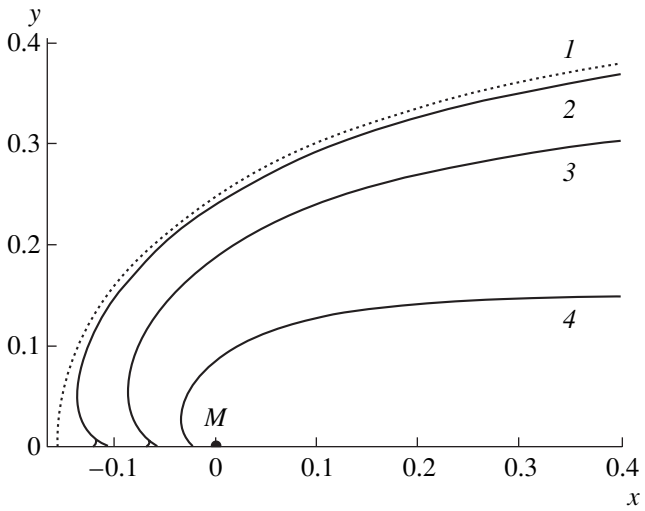

Fig. 3. Calculation results for $Q = 1$ and $\mu = (1)$ 0, (2) 0.1, (3) 1, and (4) 10.

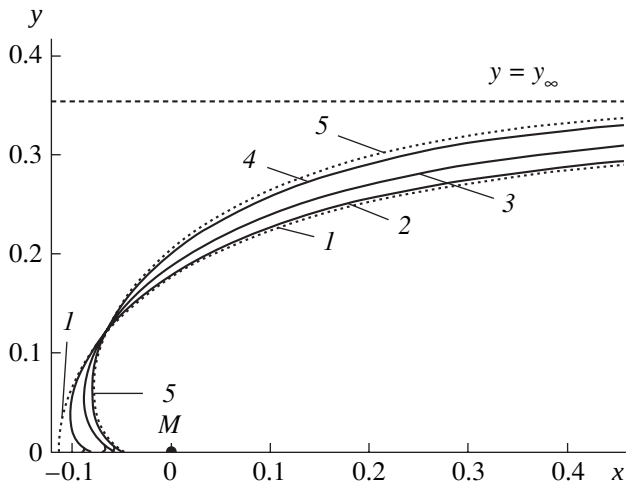

Fig. 4. Calculation results for $y_\infty = \text{const}$ and $\mu = (1)$ 0, (2) 0.1, (3) 1, (4) 10, and (5) ∞.

the method described in [4]. The good agreement of the results indicates that the proposed method with the pillar is efficient and that the assumptions made in [4] are justified.

The second series of calculations was performed to analyze the effect of the parameter μ. Figure 3 shows the calculation results for $Q = 1$, $V_0 = 0.001$, and $\mu = (2)$ 0.1, (3) 1, and (4) 10 and (1) for the limiting case $\mu = 0$. As is seen in this figure, the shape of the line l_z for $\mu = 0.1$ agrees well with the case $\mu = 0$.

In the third series of calculations, both μ and Q were varied and the rate Q was chosen so that, taking Eq. (15) into account, the lines l_z for various μ values have the common asymptotic value $y_\infty = \dfrac{1}{\sqrt{8}}$ at infinity (this value corresponds to the case of $Q = 1$ and $\mu = 1$). Figure 4 shows the shape of the interface between the media for $\mu = (2)$ 0.1, (3) 1, and (4) 10 and for the limiting cases $\mu = (1)$ 0 and (5) ∞. As is seen in this figure, the cases $\mu = 0.1$ and 10 agree well with the limiting cases $\mu = 0$ and ∞, respectively.

In addition, according to the calculation results, the line l_z approaches the asymptotic value more rapidly as μ increases. Moreover, we arrive at a seemingly paradoxical conclusion: as the jet energy increases, the flow separation point approaches the source. It is worth noting that, at a given asymptotic value at infinity, all interfaces between the media for different μ values intersect at one point.

ACKNOWLEDGMENTS

This work was supported by the Russian State Program "R&D in the Basic Directions of Science and Engineering" for 2002–2006 (project no. RI-112/001/465) and by the Academy of Sciences of the Republic of Tatarstan.

REFERENCES

1. M. I. Gurevich, *Theory of Jets in Ideal Fluids* (Nauka, Moscow, 1979) [in Russian].
2. G. Birkhoff and E. Zarantonello, *Jets, Wakes, and Cavities* (Academic, New York, 1957; Mir, Moscow, 1964).
3. Z. N. Validova and O. M. Kiselev, in *Proceedings of Seminars on Boundary Value Problems, Kazan, Russia, 1991* (Kazan. Univ., Kazan, 1991), No. 26, pp. 79–95.
4. V. M. Shurygin, *Aerodynamics of Bodies with Jets* (Mashinostroenie, Moscow, 1977) [in Russian].
5. A. M. Elizarov, N. B. Il'inskiy, and A. V. Potashev, *Mathematical Methods of Airfoil Design: Inverse Boundary Value Problems of Aerohydrodynamics* (Nauka, Moscow, 1994; Academie, Berlin, 1997).

Translated by R. Tyapaev

Doklady Physics, Vol. 50, No. 11, 2005, pp. 588–592. Translated from Doklady Akademii Nauk, Vol. 405, No. 1, 2005, pp. 51–55.

MECHANICS

On the Equations of Motion of a Spherical Pendulum with a Fluctuating Support

A. G. Petrov

Presented by Academician V.F. Zhuravlev April 28, 2005

Received April 29, 2005

The motion of a spherical pendulum under an arbitrary three-dimensional periodic vibration of the support is considered. A new system of differential equations for the radius vector of the pendulum is suggested. Unlike the equations for the spherical coordinates, the proposed system has no singular points and makes it possible to describe the motion of the pendulum under arbitrary vibrations by numerical methods or by methods of averaging in the case of high-frequency vibrations.

STATEMENT OF THE PROBLEM

Consider a spherical pendulum, namely, a material point of mass m suspended by a weightless inextensible cord of length l. The pendulum support has the radius vector $\mathbf{r}_0(x_1, x_2, x_3)$ and moves according to a prescribed law. At the opposite end of the cord, which has the radius vector $\mathbf{r}$, the material point is suspended. This material point is subject to an applied force $\mathbf{F}$ and the cord tension $\mathbf{T}$ (see figure). Then, under the action of tension $\mathbf{T}$ and applied force $\mathbf{F}$, the radius vector $\mathbf{R} = \mathbf{r} - \mathbf{r}_0$ traces out a trajectory on the sphere $|\mathbf{R}| = l$.

The problem under consideration has been investigated for a long time. The possibility of stabilizing the mathematical pendulum at the apex with the help of vertical vibrations of the support was first studied by Stephenson [1].

The oscillation of a pendulum with vertical and horizontal vibrations was investigated independently and in more detail by Bogolyubov and Kapitsa [2–4]. Asymptotical solutions to the problem of the oscillation of a planar pendulum for arbitrary vibrations are presented in papers [5, 6].

Paper [7] contains an examination of axially symmetric oscillations of a spherical pendulum with a vertically vibrating support. In papers [8, 9], for high-frequency vibrations of the support, determination of the stable periodic solutions is reduced to minimizing a function of the spherical coordinates. An additional degree of freedom significantly complicates the analysis of the system. Below, we suggest new approaches, which make the examination of the oscillation of a spherical pendulum by the numerical and asymptotic methods much easier. The periodic solution is constructed for arbitrary high-frequency vibrations.

LAGRANGE EQUATIONS AND HAMILTON EQUATIONS

For this purpose, either the Lagrange equations or the Hamilton equations are most convenient. The spherical pendulum has two degrees of freedom, namely, θ, the angle of deviation of the pendulum measured from the lower equilibrium position, and φ, the azimuth angle measured from the x-axis. The support $\mathbf{r}_0(x_1, x_2, x_3)$ is forced to vibrate periodically in all three directions, namely, in the horizontal directions x_1 and x_2

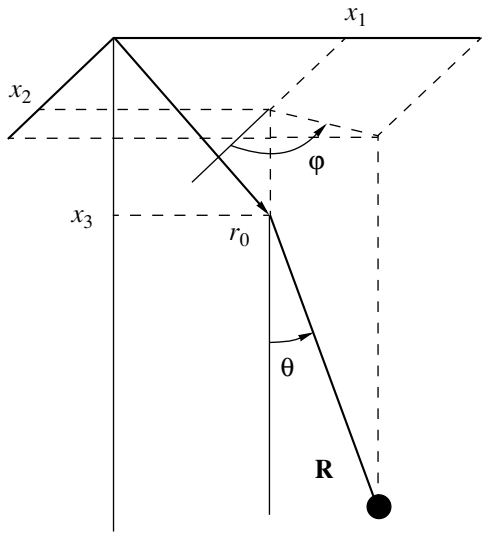

Figure.

Institute for Problems in Mechanics, Russian Academy of Sciences, pr. Vernadskogo 101, Moscow, 117526 Russia

1028-3358/05/5011-0588$26.00

and in the vertical direction x_3. The Lagrange function has the form [10]

$$L = \frac{ml^2}{2}\left[\left(\frac{d\theta}{dt}\right)^2 + \left(\sin\theta\frac{d\varphi}{dt}\right)^2\right] + l\cos\theta(F_3 - m\ddot{x}_3) + l\sin\theta((F_1 - m\ddot{x}_1)\cos\varphi + (F_2 - m\ddot{x}_2)\sin\varphi).$$

The location of the material point of the pendulum can be determined from the Lagrange equations

$$\frac{d}{dt}\frac{\partial L}{\partial\dot{\theta}} - \frac{\partial L}{\partial\theta} = 0, \quad \frac{d}{dt}\frac{\partial L}{\partial\dot{\varphi}} - \frac{\partial L}{\partial\varphi} = 0. \tag{1}$$

Equations (1) are written for two independent variables θ and φ and can be easily solved with respect to the higher derivatives $\ddot{\theta}$ and $\ddot{\varphi}$. It is also convenient to write the Hamilton form of Eqs. (1):

$$\dot{\theta} = \frac{\partial H}{\partial p_\theta}, \quad \dot{p}_\theta = -\frac{\partial H}{\partial\theta}, \quad \dot{\varphi} = \frac{\partial H}{\partial p_\varphi}, \quad \dot{p}_\varphi = -\frac{\partial H}{\partial\varphi}, \tag{2}$$

$$H = \frac{p_\theta^2}{2ml^2} + \frac{p_\varphi^2}{2ml^2\sin^2\theta} - l\cos\theta(F_3 - m\ddot{x}_3) - l\sin\theta((F_1 - m\ddot{x}_1)\cos\varphi + (F_2 - m\ddot{x}_2)\sin\varphi).$$

The Hamilton equations are particularly efficient for the study of the oscillations of a pendulum with a high-frequency vibrating support by asymptotic methods.

CONSTRUCTION OF THE PERIODIC SOLUTION BY THE METHOD OF INVARIANT NORMALIZATION OF THE HAMILTONIAN

In paper [7], axially symmetric oscillations of a spherical pendulum with a vertical support were studied by the method of the Birkhoff normal form. To determine the stable periodic solutions in that particular case, it was necessary to expand the Hamiltonian in perturbations of the coordinates up to the fourth order inclusive and to find the fourth-order Birkhoff normal form. Moreover, the change of variables and the periodic solution itself are not presented in that paper due to the cumbersome calculations.

Here, we provide a solution to the general problem of finding the periodic solutions and determining their stability in the case of arbitrary three-dimensional vibrations of the support under gravity ($F_1 = F_2 = 0$, $F_3 = mg$). We use the method of invariant normalization [11, 12]. To provide for the same accuracy of result, we need only one quadrature of simple trigonometric functions, which is easy to find without the use of analytical programming computer systems. Reduce the Hamiltonian (2) to the dimensionless form $H(\theta, \varphi, u, v) = H_0 + \Phi$, where u and v are impulses corresponding to the coordinates θ and φ.

The unperturbed part H_0 of the Hamiltonian is the energy of the inertial forces of vibration; the other terms make up the perturbation:

$$H_0 = W_{t't'}, \quad \Phi = \varepsilon\left(\frac{1}{2}u^2 + \frac{v^2}{2\sin^2\theta} - \cos\theta\right),$$
$$\varepsilon = \sqrt{\frac{g}{l\omega^2}}, \tag{3}$$
$$W = a_3\cos\theta + \sin\theta(a_1\cos\varphi + a_2\sin\varphi),$$
$$a_i(t') = \frac{\omega x_i}{\sqrt{gl}}, \quad t' = \omega t.$$

Here, ω is the support vibration frequency and $W_{t't'}$ denotes the second derivative of function W with respect to the dimensionless time t'.

Note that the form of the unperturbed Hamiltonian is arbitrary. This trick is unusual for the classical Birkhoff method. It makes it much easier to calculate the normal form and perform the integration. We use a modification of the method of invariant normalization [13, 14]. This modification does not involve the reduction of the Hamiltonian to the autonomous form and allows for an immediate computation of the quadrature. The first step of the method consists in solving the equations of the unperturbed system $\dot{\theta} = 0$, $\dot{\varphi} = 0$, $\dot{u} = -W_{t't'\theta}$, $v = W_{t't'\varphi}$, where the subscripts t', θ, and φ denote differentiation with respect to these variables.

The solution to the unperturbed system has the form

$$\theta = \theta_0, \quad \varphi = \varphi_0, \quad u = u_0 - W_{t'\theta}, \quad v = v_0 - W_{t'\varphi}.$$

The quadrature

$$\varepsilon\int_{t_0}^{t}\left[\frac{1}{2}(u - W_{t'\theta})^2 + \frac{(v - W_{t'\varphi})^2}{2\sin^2\theta_0} - \cos\theta_0\right]dt = (t - t_0)\bar{\Phi}(t_0, \theta_0, \varphi_0, u_0, v_0) + \Psi(t_0, \theta_0, \varphi_0, u_0, v_0) + f(t) \tag{4}$$

gives us the normal form

$$\bar{\Phi}(t_0, \theta_0, \varphi_0, u_0, v_0) = \varepsilon\left(\frac{1}{2}u_0^2 + \frac{v_0^2}{2\sin^2\theta_0} + U(\theta_0, \varphi_0)\right),$$
$$U(\theta_0, \varphi_0) = \frac{1}{2}\langle W_{t'\theta}^2\rangle + \frac{\langle W_{t'\varphi}^2\rangle}{2\sin^2\theta_0} - \cos\theta_0, \tag{5}$$
$$\langle f\rangle = \frac{1}{T}\int_0^T f(t)dt.$$

Expression $U(\theta_0, \varphi_0)$ coincides with the one obtained in papers [8, 9] by the method of Poincaré mappings in the parametric form. The minimum point θ_0, φ_0 of function

$U(\theta_0, \varphi_0)$ corresponds to the stable periodic solution. The periodic solution has the form

$$\theta = \theta_0 - \Psi_u + O(\varepsilon^2), \quad \varphi = \varphi_0 - \Psi_v + O(\varepsilon^2). \quad (6)$$

It can be seen from quadrature (4) that function Ψ is linear in u and v. The coefficients of the linear form are

$$\Psi_u = \varepsilon W_\theta(t', \theta_0, \varphi_0), \quad \Psi_v = \frac{\varepsilon}{\sin^2\theta} W_\varphi(t', \theta_0, \varphi_0). \quad (7)$$

Formulas (3), (6), and (7) determine the periodic trajectory up to small ε^2. With regard for the relation $\varepsilon a_i = \frac{x_i}{l}$, the trajectory equation can be written in dimensional variables:

$$\theta = \theta_0 - \frac{1}{l}[-x_3(t)\sin\theta_0 + (x_1(t)\cos\varphi_0 + x_2(t)\sin\varphi_0)\cos\theta_0], \quad (8)$$

$$\varphi = \varphi_0 - \frac{1}{l\sin\theta_0}(-x_1(t)\sin\varphi_0 + x_2(t)\cos\varphi_0).$$

EQUATIONS FOR THE RADIUS VECTOR AND THE ANGULAR MOMENTUM

Equation systems (1) and (2) have an essential drawback; namely, the spherical coordinates θ and φ are not defined at the sphere poles $\theta = 0$ and π. In this connection, when studying the pendulum oscillations in the neighborhood of the singular points, geometric difficulties are often faced, as they are hard to avoid. Below, we suggest a new system of differential equations in the radius vector **R** and the angular momentum **K**, which is explicitly solvable for the derivatives, and the constraint equation follows from this system as its integral. The idea of deducing this system of equations can be attributed to V.F. Zhuravlev.

The law of motion of the material point can be found from the variation equation for the angular momentum $\mathbf{K}(K_1, K_2, K_3)$ with respect to the support and the condition of inextensibility of the cord

$$\frac{d\mathbf{K}}{dt} = \mathbf{R}\times(\mathbf{F} - m\ddot{\mathbf{r}}_0), \quad \mathbf{K} = m\mathbf{R}\times\dot{\mathbf{R}}, \quad \mathbf{R}^2 = l^2. \quad (9)$$

The cord tension does not appear in the system of equations, because it has zero momentum about the origin. Being unresolved with respect to the derivatives $\dot{\mathbf{R}}$, Eqs. (9) in variables **K** and **R** are not convenient for the purpose of integration. Moreover, the determinant of the system of equations for $\dot{\mathbf{R}}$ is equal to zero. Nevertheless, this system can be uniquely solved. Indeed, taking the vector product of **R** with the second equation in (9), we obtain the equality $\mathbf{R}\times\mathbf{K} = m\mathbf{R}\times(\mathbf{R}\times\dot{\mathbf{R}})$, which can be rearranged by the rule $\mathbf{a}\times(\mathbf{b}\times\mathbf{c}) = \mathbf{b}(\mathbf{ac}) - \mathbf{c}(\mathbf{ab})$ to give

$$\mathbf{R}\times\mathbf{K} = m\mathbf{R}(\mathbf{R}\dot{\mathbf{R}}) - m\dot{\mathbf{R}}(\mathbf{RR}).$$

The third constraint equation in (9) implies that $(\mathbf{R}\dot{\mathbf{R}}) = 0$ and $(\mathbf{RR}) = l^2$. This gives us $\mathbf{R}\times\mathbf{K} = -ml^2\dot{\mathbf{R}}$. Together with the variation equation for the angular momentum, this equation makes up the system

$$\dot{\mathbf{K}} = \mathbf{R}\times(\mathbf{F} - m\ddot{\mathbf{r}}_0), \quad \dot{\mathbf{R}} = -\frac{1}{ml^2}\mathbf{R}\times\mathbf{K} \quad (10)$$

with the initial conditions $\mathbf{R}(0) = \mathbf{R}_0$, $\dot{\mathbf{R}}(0) = \dot{\mathbf{R}}_0$, and $\mathbf{K}(0) = m\mathbf{R}_0\times\dot{\mathbf{R}}$.

System (10) is equivalent to the initial system of equations. There is no need to write an additional constraint equation, since it is readily apparent as the integral of the system $(\mathbf{RR}) = (\mathbf{R}_0\mathbf{R}_0) = l^2$. Equation system (10) is more convenient for numerical integration than is the system of equations for the spherical coordinates of the pendulum, whose poles are singular points.

EQUATIONS FOR THE RADIUS VECTOR

One can exclude the angular momentum **K** from equation system (10) and obtain an equation in the radius vector **R** alone. To do this, differentiate the second equation in (10) with respect to time and express **K** and $\dot{\mathbf{K}}$ in terms of **R** and $\dot{\mathbf{R}}$:

$$\ddot{\mathbf{R}} = -\frac{1}{l^2}\dot{\mathbf{R}}\times(\mathbf{R}\times\dot{\mathbf{R}}) - \frac{1}{ml^2}\mathbf{R}\times(\mathbf{R}\times(\mathbf{F} - m\ddot{\mathbf{r}}_0)).$$

Expanding the vector triple product, we obtain

$$\ddot{\mathbf{R}} = -\frac{\mathbf{R}}{l^2}(\dot{\mathbf{R}}\dot{\mathbf{R}}) + \frac{1}{m}(\mathbf{F} - m\ddot{\mathbf{r}}_0) - \frac{1}{ml^2}\mathbf{R}(\mathbf{R}(\mathbf{F} - m\ddot{\mathbf{r}}_0)). \quad (11)$$

REACTION FORCE AT THE SUPPORT. WORK OF THE REACTION AT THE SUPPORT

The reaction force $\mathbf{F}_0$ at the support can be found from the Newton law

$$\mathbf{F}_0 = m(\ddot{\mathbf{r}}_0 + \ddot{\mathbf{R}}) - \mathbf{F}. \quad (12)$$

With due account of Eq. (11), the reaction force can be brought into the form

$$\mathbf{F}_0 = -\frac{\mathbf{R}}{l^2}[m(\dot{\mathbf{R}})^2 + \mathbf{R}(\mathbf{F} - m\ddot{\mathbf{r}}_0)],$$

whence it is seen that the reaction force is directed along the cord.

Assume that the support moves according to the periodic law $\mathbf{r}_0(t+T) = \mathbf{r}_0(t)$, where T is the period. Let us find the average power N of the reaction force at the support:

$$N = \langle \mathbf{F}_0 \dot{\mathbf{r}}_0 \rangle = \frac{1}{T}\int_0^T \mathbf{F}_0 \dot{\mathbf{r}}_0 dt.$$

Since $\langle \ddot{\mathbf{r}}_0 \dot{\mathbf{r}}_0 \rangle = 0$, expression (12) gives us

$$N = m\langle \ddot{\mathbf{R}} \dot{\mathbf{r}}_0 \rangle - \langle \mathbf{F} \dot{\mathbf{r}}_0 \rangle. \tag{13}$$

If the force $\mathbf{F}$ acting on the mass has a potential (for example, the gravitational force), then $\mathbf{F}\dot{\mathbf{r}}_0$ is equal to the variation of the potential energy of the mass and, for a periodic motion, $\langle \mathbf{F}\dot{\mathbf{r}}_0 \rangle = 0$, whereas, if the mass is subject to frictional forces, which depend on the velocity, then the value $\langle -\mathbf{F}\dot{\mathbf{r}}_0 \rangle$ is strictly positive and is equal to the dissipation of energy. The first term in the expression for the power can be conveniently transformed by means of integration by parts:

$$m\langle \ddot{\mathbf{R}} \dot{\mathbf{r}}_0 \rangle = -m\langle \dot{\mathbf{R}} \ddot{\mathbf{r}}_0 \rangle.$$

Substituting $\dot{\mathbf{R}}$ from Eq. (10) into the right-hand side, we obtain

$$m\langle \ddot{\mathbf{R}} \dot{\mathbf{r}}_0 \rangle = \frac{1}{l^2}\langle (\mathbf{R}\mathbf{K}\ddot{\mathbf{r}}_0) \rangle,$$

where the parenthesized expression denotes the triple product of three vectors. It is equal to the determinant of the matrix composed of the row vectors $\mathbf{R}$, $\mathbf{K}$, and $\ddot{\mathbf{r}}_0$.

SYSTEM OF EQUATIONS FOR THE COMPONENTS

Rewrite the obtained system of vector equations (10) in the components R_1, R_2,, and R_3 of the radius vector and of the angular momentum:

$$\dot{R}_1 = \frac{1}{ml^2}(-R_2K_3 + R_3K_2),$$

$$\dot{R}_2 = \frac{1}{ml^2}(-R_3K_1 + R_1K_3),$$

$$\dot{R}_3 = \frac{1}{ml^2}(-R_1K_2 + R_2K_1),$$

$$\dot{K}_1 = (-R_2(m\ddot{x}_3 - F_3) + R_3(m\ddot{x}_2 - F_2)),$$

$$\dot{K}_2 = (-R_3(m\ddot{x}_1 - F_1) + R_1(m\ddot{x}_3 - F_3)),$$

$$\dot{K}_3 = (-R_1(m\ddot{x}_2 - F_2) + R_2(m\ddot{x}_1 - F_1)).$$

Without regard for the frictional forces acting on the pendulum, the average power N at the support can be expressed in terms of the determinant

$$N = \left\langle \frac{1}{l^2} \begin{vmatrix} R_1 & R_2 & R_3 \\ K_1 & K_2 & K_3 \\ \ddot{x}_1 & \ddot{x}_2 & \ddot{x}_3 \end{vmatrix} \right\rangle.$$

PERIODIC SOLUTION IN THE CARTESIAN COORDINATES

Up to the small parameter ε, the periodic point $\mathbf{R}_0(t+T) = \mathbf{R}_0(t)$ can be found via a minimization of function $U(\theta, \varphi)$ (5) and it corresponds to the periodic solution (8). However, the minimization condition is not applicable in the neighborhood of the poles. Let us show the way to overcome this problem with the use of Eq. (11). We seek the periodic solution to Eq. (11) in the form

$$\mathbf{R} = \mathbf{R}_0 + \boldsymbol{\rho} + O(\boldsymbol{\rho}^2), \quad (\mathbf{R}_0, \boldsymbol{\rho}) = 0. \tag{14}$$

Substituting this expression into Eq. (11), up to small quantities of order $\boldsymbol{\rho}^2$, we obtain the linear equation

$$\ddot{\boldsymbol{\rho}} - \frac{\rho}{l}(\ddot{\mathbf{r}}_0 - \mathbf{g})_n = -(\ddot{\mathbf{r}}_0 - \mathbf{g})_\tau,$$
$$\mathbf{s}_n = \frac{(\mathbf{s}, \mathbf{R}_0)}{l}, \quad \mathbf{s}_\tau = \mathbf{s} - \frac{(\mathbf{s}, \mathbf{R}_0)\mathbf{R}_0}{l^2}, \tag{15}$$

where the subscript n denotes the projection of vector $\mathbf{s}$ onto the normal to the sphere $|\mathbf{R}| = l$ at point $\mathbf{R}_0$ and the subscript τ denotes its projection on the plane tangent to the sphere $|\mathbf{R}| = l$ at point $\mathbf{R}_0$. Taking into account the negligibility of the ratio $\frac{g}{|\ddot{\mathbf{r}}_0|} \sim \varepsilon$, we write the equation up to small quantities of order ε^2, namely, $\ddot{\boldsymbol{\rho}} = -\ddot{\mathbf{r}}_{0\tau}$. Hence follows the solution

$$\boldsymbol{\rho} = -\mathbf{r}_{0\tau} = -\mathbf{r}_0 + \frac{(\mathbf{r}_0\mathbf{R}_0)\mathbf{R}_0}{l^2} + O(\varepsilon^2). \tag{16}$$

If we express the Cartesian components $\mathbf{r}_0(x_1, x_2, x_3)$ in terms of the spherical coordinates, then solution (16) will coincide with (8). However, solution (16) would have no singular points. The solution has a simple physical meaning; namely, the mass $\mathbf{R} = \mathbf{R}_0 + \boldsymbol{\rho}$ traces out a trajectory on the sphere that is symmetrical to the projection of the trajectory of the support onto the plane tangent to the sphere $|\mathbf{R}| = l$ at point $\mathbf{R}_0$. As for the radius vector $\mathbf{r}_0 + \mathbf{R}_0 + \boldsymbol{\rho} = \mathbf{R}_0$ of the mass of the pendulum, its projection onto this plane is a fixed point. This means that, in the absolute system of coordinates,

the mass of the pendulum moves only in parallel to the pendulum cord.

EFFECTIVE POTENTIAL ENERGY

It follows from the theorem on the superposition of solutions to the normal form of equations [12] that, at the minimum point of function $U(\theta, \phi)$ [see Eq. (5)], the periodic solution is stable. In the Cartesian system of coordinates, with due account taken of the dimensional factor mgl, the function $U_{\text{eff}} = mglU(\theta, \phi)$ has the form

$$U_{\text{eff}} = \frac{m}{2}\langle \dot{\mathbf{r}}_{0\tau}^2 \rangle - m\langle \mathbf{gR} \rangle, \quad \mathbf{r}_{0\tau}^2 = (\mathbf{r}_0\mathbf{r}_0) - \frac{(\mathbf{r}_0\mathbf{R})^2}{l^2},$$

where $\mathbf{r}_{0\tau}$ is the projection of the support velocity onto the plane tangent to the sphere.

Thus, the effective potential energy U_{eff} under vibration is equal to the sum of the values of the kinetic and potential energies averaged over the period.

ACKNOWLEDGMENTS

I am grateful to V.F. Zhuravlev for discussions of the results and to D.M. Klimov for his attention to the work. This work was supported by the Russian Foundation for Basic Research, project no. 05-01-004303.

REFERENCES

1. A. Stephenson, Mem. Proc. Manchester Lit. Philos. Soc. **52** (8), 1 (1908).
2. N. N. Bogolyubov, Tr. Inst. Stroit. Mekh. Akad. Nauk USSR, No. 14, 9 (1950).
3. P. L. Kapitsa, Zh. Éksp. Teor. Fiz. **21** (5), 588 (1951).
4. P. L. Kapitsa, Usp. Fiz. Nauk **44** (1), 7 (1951).
5. V. N. Bogaevskiĭ and A. Ya. Povzner, *Algebraic Methods in Nonlinear Perturbation Theory* (Nauka, Moscow, 1987) [in Russian].
6. L. D. Akulenko, Prikl. Mat. Mekh. **58** (3), 23 (1994).
7. A. P. Markeev, Prikl. Mat. Mekh. **63** (2), 213 (1999).
8. A. G. Petrov, Dokl. Akad. Nauk **368** (4), 481 (1999) [Dokl. Phys. **44** (8), 698 (1999)].
9. A. G. Petrov, Mekh. Tverd. Tela, No. 3, 19 (2001).
10. L. D. Landau and E. M. Lifshitz, *General Physics*. Vol. 1: *Mechanics* (Nauka, Moscow, 1965; Pergamon, Oxford, 1967).
11. V. F. Zhuravlev, *Fundamentals of Theoretical Mechanics* (Nauka, Moscow, 1997) [in Russian].
12. V. F. Zhuravlev, Prikl. Mat. Mekh. **66** (3), 256 (2002).
13. A. G. Petrov, Dokl. Akad. Nauk **386** (4), 343 (2002) [Dokl. Phys. **47** (10), 742 (2002)].
14. A. G. Petrov, Prikl. Mat. Mekh. **68** (3), 402 (2004).

Translated by A. Pankrat'ev

Doklady Physics, Vol. 50, No. 11, 2005, pp. 593–597. Translated from Doklady Akademii Nauk, Vol. 405, No. 1, 2005, pp. 56–60.

MECHANICS

On the Motion of a Body Containing a Movable Internal Mass

Academician F. L. Chernous'ko

Received June 22, 2005

It is known that a body can move on a horizontal plane due to internal oscillatory motions in the presence of the forces of dry friction between the body and the plane. In this study, we consider a very simple mechanical model of such a motion realized as a result of the specific periodic relative motions of a material point inside the body.

The internal motion parameters providing for a maximum average velocity of the system as a whole are determined.

1. Consider an absolutely rigid body of mass M that can move along a horizontal line. Inside the body, there is a movable mass m that also moves horizontally (Fig. 1). In what follows, for the sake of brevity, the body of mass M and the internal mass will be referred to as body M and mass m, respectively. Denote the absolute coordinate of body M by x, its velocity by v, the displacement of mass m relative to body M by ξ, and the velocity and acceleration of mass m relative to body M by u and w, respectively.

Write the kinematic equations of the motion of mass m relative to body M in the form

$$\dot{\xi} = u, \quad \dot{u} = w. \tag{1}$$

Body M is exposed to the force of dry friction; the friction coefficients may be different for the onward (f_+) and backward (f_-) motion of the body.

We introduce the notation

$$a_+ = f_+ g, \quad a_- = f_- g, \quad c = \frac{a_+}{a_-}, \qquad \mu = m(M+m)^{-1} < 1, \tag{2}$$

where g is the acceleration of gravity, and write the equations of the absolute motion of body M in the form

$$\begin{aligned} \dot{v} &= -\mu w - a_+ \quad \text{for} \quad v > 0, \\ \dot{v} &= -\mu w + a_- \quad \text{for} \quad v < 0, \\ v &= 0 \quad \text{for} \quad -a_+ \le \mu w \le a_-. \end{aligned} \tag{3}$$

We consider periodic motions of mass m relative to body M within a bounded displacement range $0 \le \xi(t) \le L$, where $L > 0$ is a given parameter.

Moreover, we impose the conditions $\xi(0) = \xi(T) = 0$ and $u(0) = u(t) = 0$, where T is the motion period, and require that the value $\xi(\theta) = L$ be reached at a certain $\theta \in (0, T)$. We restrict ourselves to the consideration of two classes of periodic relative motions of mass m, which will be called two-phase and three-phase.

In the two-phase motion, the relative velocity $u(t)$ is piecewise-constant and the period includes two intervals of constant velocity.

In the three-phase motion, the relative acceleration $w(t)$ is piecewise-constant and the period includes three intervals of constant acceleration.

It can be shown that, under the periodicity conditions imposed, the two-phase and three-phase motions under consideration exhibit the least possible number of intervals of constant velocity and constant acceleration, respectively.

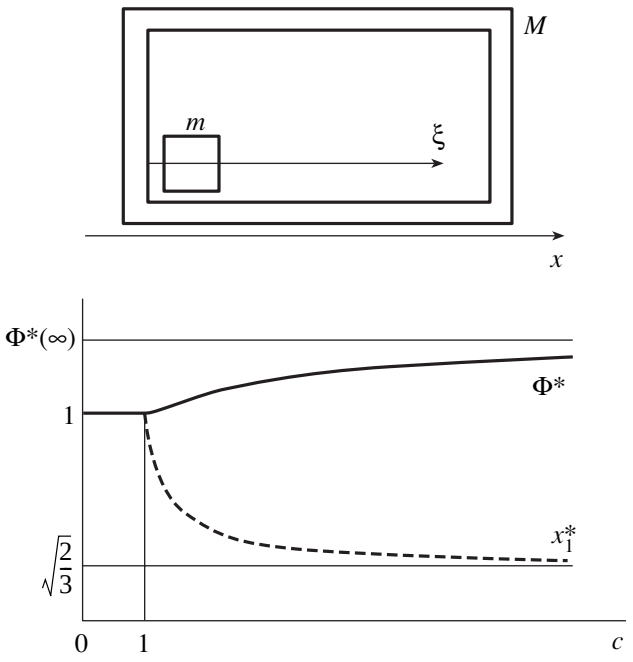

Fig. 1. Mechanical model and functions $x_1^*(c)$ and $\Phi^*(c)$.

Institute for Problems in Mechanics,
pr. Vernadskogo 101, Moscow, 119526 Russia
e-mail: chern@ipmnet.ru

1028-3358/05/5011-0593$26.00

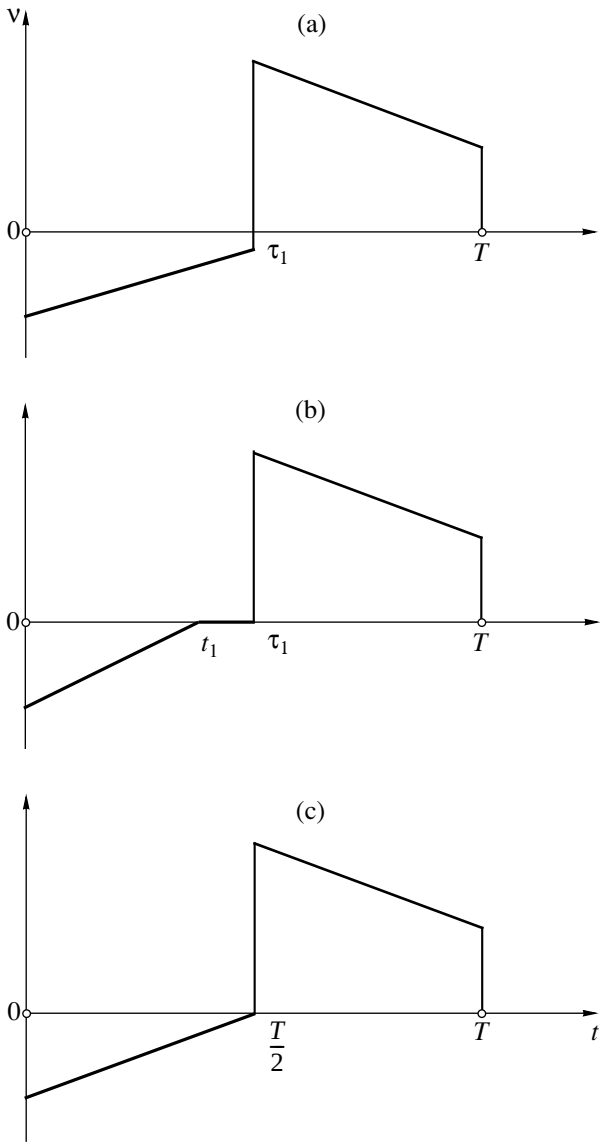

Fig. 2. Two-phase motion.

Denoting the interval duration by τ_i, for the two-phase motion, we have

$$\begin{aligned} u(t) &= u_1 \quad \text{for} \quad t \in (0, \tau_1), \\ u(t) &= -u_2 \quad \text{for} \quad t \in (\tau_1, T), \quad T = \tau_1 + \tau_2, \end{aligned} \tag{4}$$

where u_1 and u_2 are positive constants. Under the conditions imposed, the two-phase motion is determined by two parameters, u_1 and u_2, which are subject to the following constraint:

$$0 < u_i \le U, \quad i = 1, 2. \tag{5}$$

Here, U is the highest permissible velocity. Using Eq. (1) and two periodicity conditions, we can express the other parameters in terms of u_1 and u_2 as follows:

$$\tau_1 = \theta = \frac{L}{u_1}, \quad \tau_2 = \frac{L}{u_2}, \quad T = L(u_1^{-1} + u_2^{-1}). \tag{6}$$

For the three-phase motion, we have

$$\begin{aligned} w(t) &= w_1 \quad \text{for} \quad t \in (0, \tau_1), \\ w(t) &= -w_2 \quad \text{for} \quad t \in (\tau_1, \tau_1 + \tau_2), \\ w(t) &= w_3 \quad \text{for} \quad t \in (\tau_1 + \tau_2, T), \quad T = \tau_1 + \tau_2 + \tau_3. \end{aligned} \tag{7}$$

The parameters w_i are subject to the constraint

$$0 < w_i \le W, \quad i = 1, 2, 3, \tag{8}$$

where W is the highest permissible acceleration. By virtue of Eqs. (1) and the periodicity conditions, the other parameters can be expressed in terms of w_i as follows:

$$\begin{aligned} \tau_1 &= \left[\frac{2w_2L}{w_1(w_1 + w_2)}\right]^{1/2}, \quad \tau_3 = \left[\frac{2w_2L}{w_3(w_2 + w_3)}\right]^{1/2}, \\ \tau_2 &= \left(\frac{2L}{w_2}\right)^{1/2}\left[\left(\frac{w_1}{w_1 + w_2}\right)^{1/2} + \left(\frac{w_2}{w_2 + w_3}\right)^{1/2}\right], \\ T &= \left(\frac{2L}{w_2}\right)^{1/2}\left[\left(\frac{w_1 + w_2}{w_1}\right)^{1/2} + \left(\frac{w_2 + w_3}{w_3}\right)^{1/2}\right]. \end{aligned} \tag{9}$$

Substituting the laws of motion (4) and (7) into Eqs. (1) and (3) and using the imposed periodicity conditions together with Eqs. (6) and (9), we study the possible motions of body M. Determine the motions from the classes under consideration such that

(1) the velocity of body M varies periodically;

(2) the conditions $v(0) = v(T) = 0$ are fulfilled; and

(3) the average velocity of body M, which is equal to $V = \dfrac{x(T)}{T}$, is maximal.

We present the results obtained for the two-phase and three-phase motions.

2. The analysis shows that, for the two-phase motion (4), the maximal average velocity can be realized in one of the two regimes presented in Fig. 2. In regime a, there is no interval in which body M is at rest and velocity $v(t)$ varies by the law

$$v(t) = -\mu u_1 + a_- t \quad \text{for} \quad t \in (0, \tau_1),$$

$$v(t) = \mu u_2 + a_-\tau_1 - a_+(t - \tau_1) \quad \text{for} \quad t \in (\tau_1, T).$$

In regime *b*, there is a rest interval (t_1, τ_1) and

$$v(t) = -\mu u_1 + a_- t \quad \text{for} \quad t \in (0, t_1), \quad t_1 < \tau_1,$$

$$v(t) = 0 \quad \text{for} \quad t \in (t_1, \tau_1),$$

$$v(t) = \mu(u_1 + u_2) - a_+(t - \tau_1) \quad \text{for} \quad t \in (\tau_1, T).$$

We pass to dimensionless parameters according to the formulas

$$u_0 = \left(\frac{La_-}{\mu}\right)^{1/2}, \quad u_i = u_0 x_i, \quad i = 1, 2,$$
$$U = u_0 X, \quad V = 0.5\mu u_0 \Phi, \quad c = \frac{a_+}{a_-}. \tag{10}$$

First, consider the case in which there is no upper bound (5), that is, $X \longrightarrow \infty$. In this case, the maximal average velocity is attained at $c \le 1$ in regime *a* and at $c > 1$ in regime *b*. Here, for the optimal motion, we have

$$x_1 = 1, \quad x_2 = c, \quad \Phi = 1 \quad \text{for} \quad c \le 1,$$
$$x_1 = x_1^*(c), \quad x_2 = \frac{c}{x_1^*(c)}, \tag{11}$$
$$\Phi = \Phi(x_1^*(x)) = \Phi^*(c) \quad \text{for} \quad c > 1.$$

Here, the following notation is introduced:

$$x_1^*(c) = \left\{\frac{c}{2}(c-1)^{-1}[1 - 3c + (9c^2 + 2c - 7)^{1/2}]\right\}^{1/2}, \tag{12}$$

$$\Phi(x) = [2c + x^2(1-c)]x(c + x^2)^{-1}.$$

The dependences $x_1^*(c)$ and $\Phi^*(c)$ are plotted in Fig. 1. Let us emphasize some properties of these functions.

As c varies from 1 to ∞, function $x_1^*(c)$ decreases monotonically from 1 to $\left(\frac{2}{3}\right)^{1/2} = 0.816$, while function $\Phi^*(c)$ increases monotonically from 1 to $\frac{4}{3}\left(\frac{2}{3}\right)^{1/2} = 1.089$. Thus, the advantage in velocity of the optimal regime *b* over regime *a* is not greater than 9%.

In the simplest case of the isotropic dry friction, when $a_+ = a_- = a$, we have $c = 1$ and, in accordance with Eqs. (10) and (11), we obtain

$$x_1 = x_2 = 1, \quad u_1 = u_2 = u_0 = \left(\frac{La}{\mu}\right)^{1/2},$$

$$\tau_1 = \tau_2 = \tau_0 = \left(\frac{\mu L}{a}\right)^{1/2},$$

$$T = 2\tau_0, \quad V = 0.5(\mu La)^{1/2}.$$

This case is presented in Fig. 2c.

In the presence of constraint (5), the two-phase motion under consideration can be realized only when

$$X \ge \max(c^{1/2}, c). \tag{13}$$

The optimal motion is determined by the relations

$$x_1 = X, \quad x_2 = \frac{c}{X}, \quad \Phi = \Phi(X) \quad \text{for} \quad c^{1/2} \le X < 1,$$

$$x_1 = 1, \quad x_2 = c, \quad \Phi = 1 \quad \text{for} \quad c \le 1, \quad X \ge 1,$$

$$x_1 = \frac{c}{X}, \quad x_2 = X, \quad \Phi = \Phi\left(\frac{c}{X}\right)$$
$$\text{for} \quad 1 < c \le X < \frac{c}{x_1^*(c)}, \tag{14}$$

$$x_1 = x_1^*(c), \quad x_2 = \frac{c}{x_1^*(c)}, \quad \Phi = \Phi^*(c)$$
$$\text{for} \quad \frac{c}{x_1^*(c)} \le X.$$

Here, notation given by Eqs. (11) and (12) is used.

Four cases (14) are associated with domains *1–4* in Fig. 3a. The boundaries of these domains are the straight lines $c = 1$, $X = 1$, and $X = c$ and the curves $X = c^{1/2}$ and $X = \frac{c}{x_1^*(c)}$ marked by letters *K* and *N*, respectively. Regime *a* is realized in domain *2*, while, in the other domains, regime *b* is realized. The passage to the original dimensional parameters in Eq. (14) can be carried out according to formulas (10).

3. An analysis of the three-phase motion (7) leads to two possible regimes for the motion of body *M*; they are denoted by *a* and *b* and are presented in Figs. 4a and 4b. In regime *a*, there is an interval of the backward motion of body *M*, in which $v < 0$, whereas such intervals are absent in regime *b*. It is shown that the maximal average velocity is always realized in regime *b*, in which

$$v(t) = 0 \quad \text{for} \quad t \in [0, \tau_1],$$

$$v(t) = (\mu w_2 - a_+)(t - \tau_1) \quad \text{for} \quad t \in [\tau_1, \tau_1 + \tau_2],$$

$$v(t) = (\mu w_2 - a_+)\tau_2 - (\mu w_3 + a_+)(t - \tau_1 - \tau_2)$$
$$\text{for} \quad t \in [\tau_1 + \tau_2, t_2],$$

$$v(t) = 0 \quad \text{for} \quad t \in [t_2, T], \quad t_2 \in [\tau_1 + \tau_2, T].$$

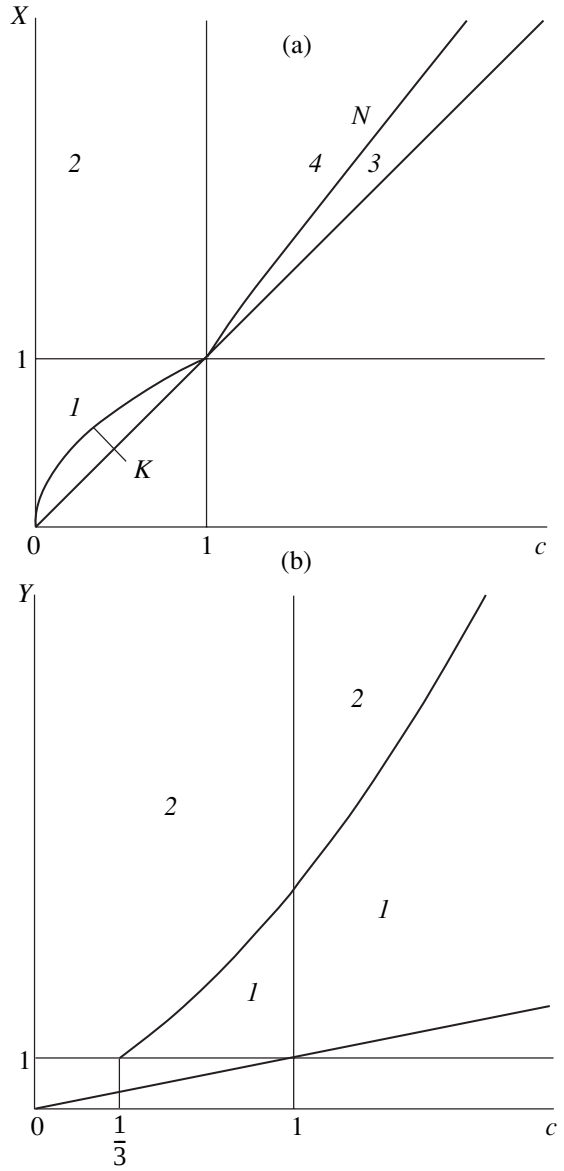

Fig. 3. Domains of optimal two-phase (a) and three-phase (b) motions.

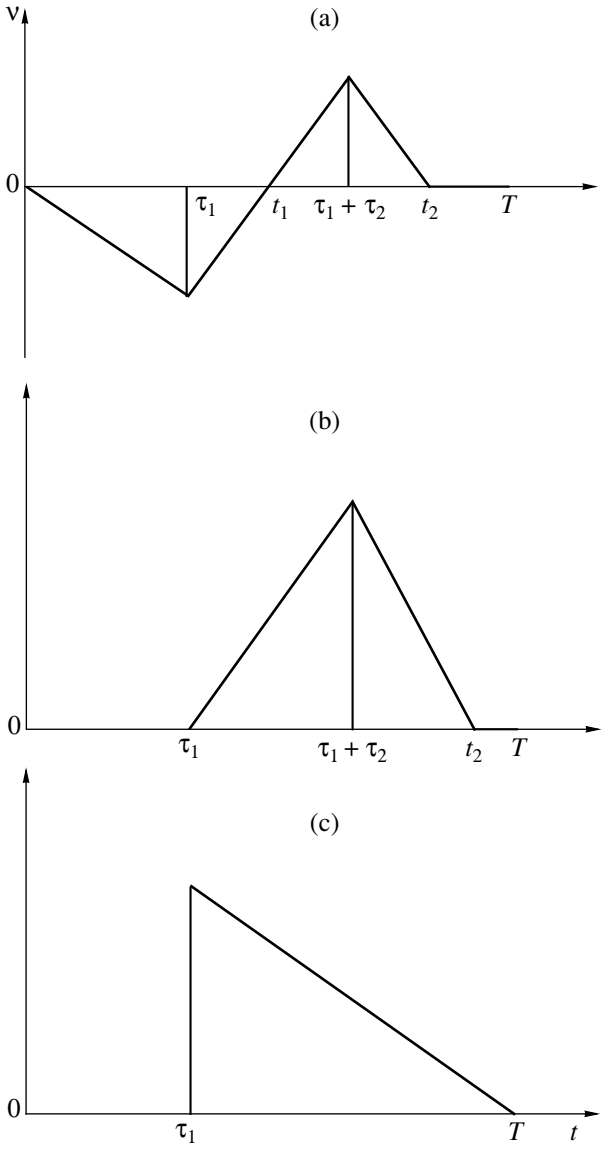

Fig. 4. Three-phase motion.

We pass to dimensionless parameters according to the formulas

$$y_i = \frac{\mu w_i}{a_-}, \quad i = 1, 2, 3, \quad W = \frac{a_-}{\mu} Y, \qquad V = \left(\frac{\mu L a_-}{2}\right)^{1/2} F \tag{15}$$

and, first, determine the optimal values of the parameters in the absence of the upper bound in (8), that is, as $Y \longrightarrow \infty$. We obtain

$$y_1 = 1, \quad y_2 = \infty, \quad y_3 = c^2, \quad F = 1. \tag{16}$$

In accordance with Eqs. (15) and (9), motion (16) undergoes a velocity jump $\Delta v = \left(\frac{2\mu L}{a_-}\right)^{1/2} (a_+ + a_-)$ at instant $t = \tau_1$. We have

$$\tau_1 = \left(\frac{2\mu L}{a_-}\right)^{1/2}, \quad \tau_2 = 0, \quad \tau_3 = \frac{(2\mu L a_-)^{1/2}}{a_+}, \qquad t_2 = \tau_1 + \tau_3 = T. \tag{17}$$

There is no rest interval for body M at the end of the period. The velocity diagram of body M in the optimal regime in the absence of the upper bound for the acceleration ($Y \longrightarrow \infty$) is presented in Fig. 4c.

In the case of the isotropic dry friction $a_+ = a_- = a$, in accordance with formulas (15)–(17), we have

$$w_1 = w_3 = \frac{a}{\mu}, \quad w_2 = \infty, \quad \tau_1 = \tau_3 = \left(\frac{2\mu L}{a}\right)^{1/2}, \quad \tau_2 = 0,$$

$$\Delta v = 2(2\mu La)^{1/2}, \quad V = \left(\frac{\mu La}{2}\right)^{1/2}.$$

In the presence of constraint (8), the three-phase regime of motion is realizable under the condition

$$Y > \max(1, c). \tag{18}$$

The optimal motion is determined by the relations

$$y_1 = 1, \quad y_2 = Y, \quad y_3 = 1, \quad F = \frac{2(Y-c)}{(c+1)Y^{1/2}(Y+1)^{1/2}}$$

$$\text{for } \max(1, c) < Y \le Y^*,$$

$$y_1 = 1, \quad y_2 = Y, \quad y_3 = \frac{c^2(Y+1)}{Y - c(c+2)}, \tag{19}$$

$$F = \left(\frac{Y}{Y+1}\right)^{1/2} \text{ for } Y > \max(1, Y^*),$$

where the following notation is introduced:

$$Y^*(c) = c[1 + c + (2 + 2c + c^2)^{1/2}]. \tag{20}$$

The first case in (19) corresponds to the presence of a nonzero rest interval at the end of the period: here, $t_2 < T$ (see Fig. 4b). In the second case of (19), the rest interval at the end of the period is absent, as is demonstrated in Fig. 4c, and $t_2 = T$.

Figure 3b shows the c,Y-plane. The domains that correspond to the two cases (19) are marked by numbers *1* and *2*, respectively. The figure depicts the lines $c = 1$, $Y = 1$, and $Y = c$, as well as the curve $Y = Y^*(c)$.

In the case of the isotropic dry friction $a_+ = a_- = a$, Eqs. (19) and (20) take the form

$$y_1 = 1, \quad y_2 = Y, \quad y_3 = 1,$$

$$F = \frac{Y-1}{Y^{1/2}(Y+1)^{1/2}} \text{ for } 1 < Y \le 2 + \sqrt{5}, \tag{21}$$

$$y_1 = 1, \quad y_2 = Y, \quad y_3 = \frac{Y+1}{Y-3}, \quad F = \left(\frac{Y}{Y+1}\right)^{1/2}$$

for $Y > 2 + \sqrt{5}$.

In solutions (19)–(21), the passage to the dimensional variables can be carried out according to formulas (15) and (9).

4. Thus, the optimal two-phase and three-phase motions in the presence of the anisotropic dry friction are completely constructed both in the absence and in the presence of constraints on the relative velocity (5) and relative acceleration (8) of mass m.

Note some peculiar features of the obtained optimal motions. In the absence of constraints (5), the average velocity of the two-phase motion is, in accordance with Eqs. (10) and (11), $V \sim \frac{(\mu La_-)^{1/2}}{2}$. In the absence of constraints (8), the average velocity of the three-phase motion is, in accordance with Eqs. (15) and (16), $V = \left(\frac{\mu La_-}{2}\right)^{1/2}$. In both cases, the velocity of body M is bounded for any permissible (including the case of infinitely high) velocities and accelerations of the relative motion of mass m. For the cases of two-phase and three-phase motions, the values of the maximum velocities differ only in the coefficients.

In spite of the considerable difference between the original assumptions made for the two-phase and three-phase regimes, there is a great deal of similarity between the corresponding optimal regimes.

In the presence of a restriction on the velocity (acceleration) of mass m, the two-phase (three-phase) motion is possible only under conditions (13) and (18) for the two-phase and three-phase motions, respectively, that is, at a fairly high level of these constraints. As $X \longrightarrow \infty$ or $Y \longrightarrow \infty$, the corresponding optimal motions (14) and (19) transform into motions (11) and (16) corresponding to the absence of these constraints.

The displacement principle considered in this study may be of interest for certain types of mobile robots.

ACKNOWLEDGMENTS

This work was supported by the Russian Foundation for Basic Research, project nos. 05-01-00647, 04-01-04002, and by the Council of the President of the Russian Federation for the Support of Young Scientists and Leading Scientific Schools (project no. NSh-1627.2003.1).

Translated by M. Lebedev

Doklady Physics, Vol. 50, No. 11, 2005, pp. 598–600. Translated from Doklady Akademii Nauk, Vol. 405, No. 2, 2005, pp. 193–195.

MECHANICS

Stationary Solitary Three-Dimensional Waves on a Vertically Flowing Fluid Film

Corresponding Member of the RAS S. V. Alekseenko, V. A. Antipin, V. V. Guzanov, D. M. Markovich, and S. M. Kharlamov

Received June 24, 2005

Three-dimensional waves appear at the final stage of the evolving wave regime of a fluid-film flow [1]. At this stage, for values of the Reynolds number of the film flow that are sufficiently low (Re < 100), the wave regime manifests itself as a soliton gas. The film surface is covered by numerous horseshoe-shaped waves, which propagate over a thin residual layer, randomly interacting with each other and explicitly demonstrating a nonlinear character of motion. Here, $\mathrm{Re} = \frac{q}{\nu}$, where q is the specific fluid-flow rate and ν is the kinematic viscosity. There is no mathematical description of these wave regimes in the literature.

A theoretical solution describing a time-independent (stationary) solitary nonlinear wave similar in its shape to waves observed in experiments is obtained in [2] for the case of Re ~ 1. In [3], an equation is analyzed that generalizes the equations used in [2] for the case of intermediate Reynolds numbers. Several branches of time-independent solutions are found. The solution obtained in [2] is related to one of these branches. The other solutions correspond to solitary multi-humped waves. In addition, the experimental determination of characteristics for determinate three-dimensional waves is hampered by their chaotic interaction with each other. Therefore, the problem of the existence of stationary solitary three-dimensional waves continued to be an open one until quite recently. The significant technical difficulties accompanying the investigation of natural three-dimensional waves are also associated with the slow rate of processes of evolution: the long-term nonlinear evolution of two-dimensional waves (or waves close in terms of shape to two-dimensional ones) precedes the appearance of a developed wave regime. It is for this reason that the operating-segment length of an experimental setup must be of a sufficiently large size. The length may be considerably reduced provided that we promote the decay of regular two-dimensional waves using an external action. However, even in this case, the interaction between produced three-dimensional waves strongly affects their characteristics.

An alternative method for the generation of solitary three-dimensional waves, which makes it possible to study regularities of their development on the basis of a compact experimental setup, consists in wave excitation by a point source. This source should be used in the initial segment of the film flow, where the level of natural perturbations is low, and the film can be considered as smooth. This approach was employed in [4]; however, time-independent horseshoe-shaped waves were not observed.

In this study, using a point excitation source under the condition of small Reynolds numbers 2.0 < Re < 5.0, we have managed to observe for the first time the formation of stationary three-dimensional solitary waves. The values of the Reynolds numbers are close to those of the residual layer for a developed wave film flow.

Our experiments were carried out on a vertical plate made of an optic glass and having a width of 200 mm and a length of 300 mm. To form the film, we applied a slit distributor with a slit size of 0.23 mm. We have registered the wave pattern on the flowing film by the fluorescent-visualization method [5, 6]. The essence of the method consists in the fact that the instantaneous distribution of the film thickness on the plate is determined by the intensity of the fluorescence radiation emitted by a dyer dissolved in the liquid. In contrast to [5, 6], we employed Particle Image Velocimetry measuring equipment [7] that was adapted to the conditions of our experiment, which operated in the double-frame regime. This allowed us to determine not only the spatial configuration but also the instantaneous velocities of rapidly evolving waves. While registering the wave pattern, we took pictures with a visual field of 100 mm ×

Kutateladze Institute of Thermal Physics, Siberian Division, Russian Academy of Sciences, pr. Akademika Lavrent'eva 1, Novosibirsk, 630090 Russia

e-mail: aleks@itp.nsc.ru; antipin@itp.nsc.ru; guzan@gorodok.ru; dmark@itp.nsc.ru; kharlamov@itp.nsc.ru

1028-3358/05/5011-0598$26.00

100 mm in area, which has provided a spatial resolution of 0.1 mm over the entire plate surface. The excitation of three-dimensional waves was realized by the short-time impact (of duration 10–15 ms) of a thin jet of the liquid in the upper part of the wave-free zone of the film flow. It was assumed that, under certain excitation conditions, a wave could attain the stationary state for a very short time. Therefore, the wave-excitation energy (basically, variable at the expense of the ejected-fluid mass) varied over a wide range in the course of the experiment. The character of the wave evolution along the operating segment of the experimental setup was determined according to the variation of the amplitude, velocity, and characteristic longitudinal and transverse sizes of the wave. Then, the wave was considered to be stationary provided that all its indicated properties remained constant in the lower part of the wave-free zone over the length of not less than three characteristic longitudinal sizes. The liquid used in the experiments (water-alcohol solution) had the following physical characteristics. The surface tension was $\sigma = 0.03$ kg s^{-2}, the density was $\rho = 931$ kg m^{-3}, and $\nu = 2.7 \times 10^{-6}$ m^2 s^{-1}. The rhodamine 6Zh that does not belong to surface-active substances was used at a weight concentration of ~0.01% as a fluorescent dyer.

For a number of the flow regimes under study, it turned out to be possible to find the excitation conditions under which the initial perturbation, after its relatively short-term evolution, transformed into a stationary solitary wave. The stationary-wave patterns obtained experimentally are shown in Fig. 1. For Re ~ 2, the wave shape is close to that described by the theoretical solution of [2]. However, as the Reynolds number is increased up to Re = 4–5 (Figs. 1b, 1c), noticeable differences appear: the crest bend increases, the crest lateral walls significantly elongate in the longitudinal direction, and a thin groove-shaped depression arises between them. The wave characteristics presented in Fig. 1c are measured in the region of the wave interaction with growing two-dimensional natural waves, which can be observed on the left part of Fig. 1c in the form of transverse wrinkles. At the same time, as can be seen from Fig. 2, for all Reynolds numbers, the amplitudes and velocities of the registered waves remain close to their values as calculated in [2].

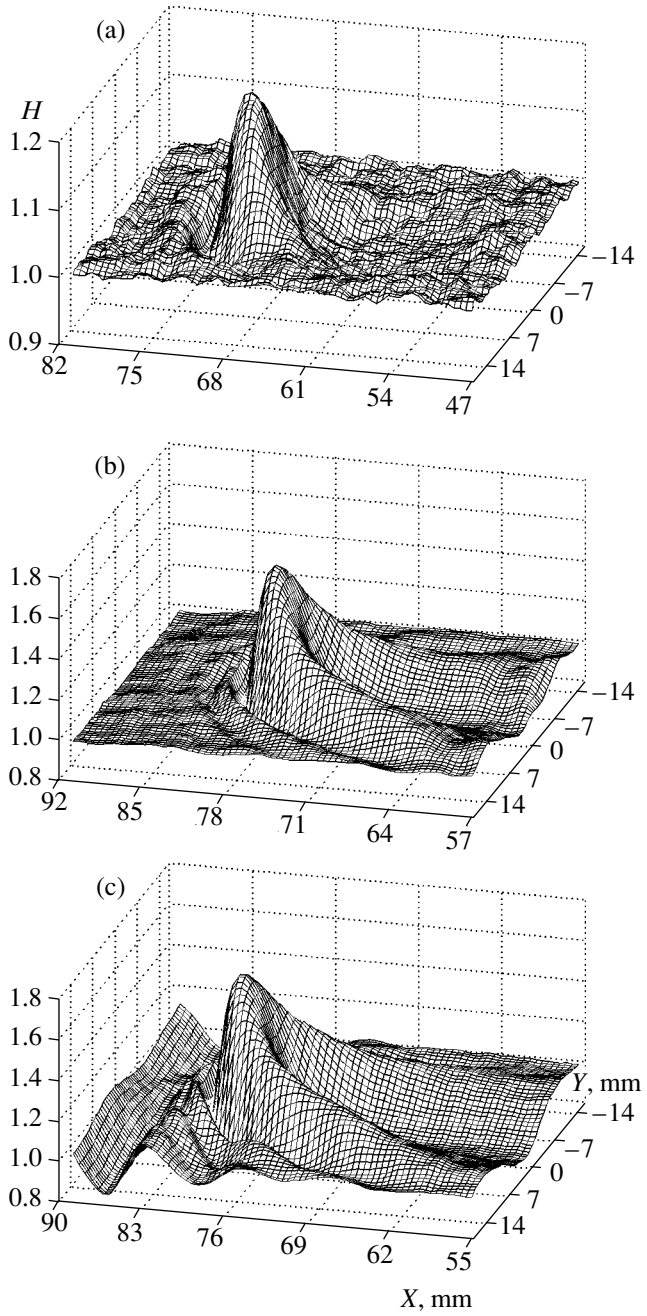

Fig. 1. Spatial shape of stationary solitary three-dimensional waves for Re = (a) 2.5, (b) 3.9, and (c) 4.8; H is the ratio of the local thickness to that of the unperturbed film, X is the distance downstream from the excitation point, and Y is the transverse coordinate.

Varying excitation conditions, we have managed to form two-humped solitary waves similar to those predicted in [3]. Contrary to single-humped waves, slowly evolving waves of this type were observed at distances that exceeded by several times those characterizing the attainment of the stationary regime by single-humped waves. In addition, the two-humped waves are less stable as compared to single-humped waves. In the case of fixed excitation conditions, the long-term and smooth evolution of these waves equiprobably results either in the rapid merging of humps or in the formation of a stationary two-humped wave. By virtue of the features indicated, the experimental study of two-humped waves represents a much more complicated problem than that of single-humped waves. One of the examples of a stationary two-humped solitary wave is shown in Fig. 3.

Thus, in the present study, we have demonstrated for the first time the existence of stationary solitary three-

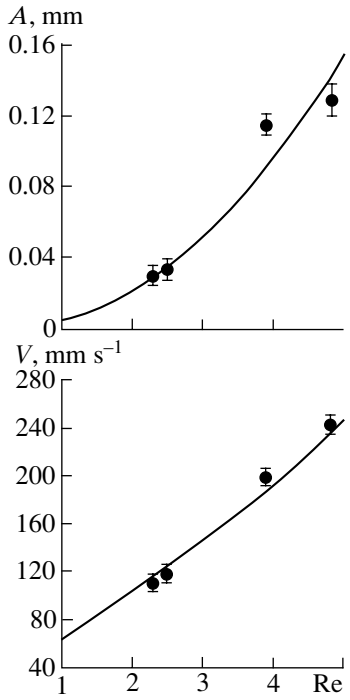

Fig. 2. Amplitude A and velocity V of stationary waves. The solid line corresponds to the calculation results of [2].

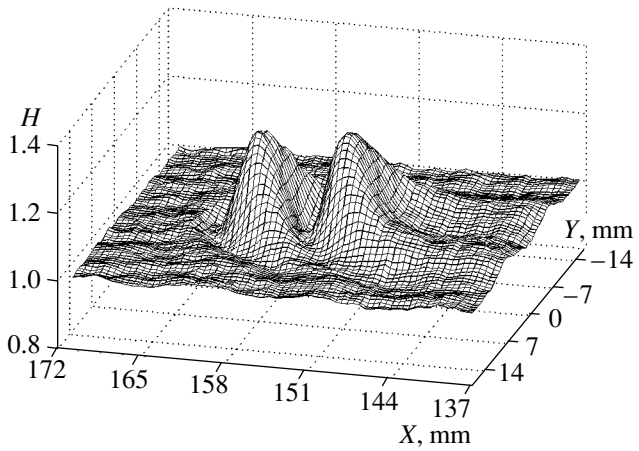

Fig. 3. Stationary two-humped solitary wave for Re = 2.2.

dimensional waves on a vertical flowing fluid film at small Reynolds numbers. Experimental data related to regularities of the propagation and spatial shape of three-dimensional perturbations are also obtained. The agreement for a number of parameters predicted by existing theories has been demonstrated.

ACKNOWLEDGMENTS

This work was supported by the Russian Foundation for Basic Research, project no. 03-02-16695a, and by the Foundation for the Assistance of Russian Science.

REFERENCES

1. S. V. Alekseenko, V. E. Nakoryakov, and B. G. Pokusaev, *Wave Flow of Fluid Films* (Nauka, Novosibirsk, 1992) [in Russian].

2. V. I. Petviashvili and O. Yu. Tsvelodub, Dokl. Akad. Nauk SSSR **238**, 1321 (1978) [Sov. Phys. Dokl. **23**, 117 (1978)].

3. H.-C. Chang and A. E. Demekhin, *Complex Wave Dynamics on Thin Films* (Elsevier, New York, 2002).

4. S. V. Alekseenko, V. A. Antipin, S. M. Kharlamov, and D. M. Markovich, in *Proceedings of 2nd International Berlin Workshop—IBW2 on Transport Phenomena with Moving Boundaries, Berlin, Germany, 2004* (VDI, Berlin, 2004), pp. 49–61.

5. J. Liu, J. D. Paul, and J. P. Gollub, J. Fluid Mech. **250**, 69 (1993).

6. M. Vlachogiannis and V. Bontozoglou, J. Fluid Mech. **435**, 191 (2001).

7. S. V. Alekseenko, A. V. Bil'skiĭ, and D. M. Markovich, Prib. Tekh. Éksp., No. 5, 145 (2004) [Instrum. Exp. Tech. **47** (5), 703 (2004)].

Translated by G. Merzon

Doklady Physics, Vol. 50, No. 11, 2005, pp. 601–604. Translated from Doklady Akademii Nauk, Vol. 405, No. 2, 2005, pp. 196–198.

MECHANICS

On the Propagation of Elastic Surface Waves in the Cosserat Medium

M. A. Kulesh, Academician V. P. Matveenko, and I. N. Shardakov

Received March 23, 2005

INTRODUCTION

In this paper, we analyze the problem on the propagation of elastic surface waves in the Cosserat medium (the half-space case). The strain state is characterized by an independent displacement vector and rotation vector, the stress tensor and the moment-stress tensor being asymmetric [1, 2]. In contrast to certain well-known studies [3–6], we seek the solutions for equations of motion in the form of wave packets determined by an arbitrary-shape Fourier spectrum. The solution found consists of two independent parts: one of them describes the Rayleigh wave, whereas the other corresponds to the transverse wave that attenuates as the depth is increased. For both wave types, the analytical solutions are written out in terms of displacements. It is especially worth noting that, in contrast to the Rayleigh wave, the solution obtained for a transverse surface wave has no analogs in the classical elasticity theory. As numerical illustrations, we compare the solutions for transverse and Rayleigh waves.

FORMULATION OF THE PROBLEM

We consider a half-space with its surface free of loads for the case in which mass forces and moments are absent. To describe the elastic Cosserat medium, we exploit the following relationships [1]:

$$\begin{aligned}(2\mu + \lambda)\mathrm{graddiv}\mathbf{u} - (\mu + \alpha)\mathrm{curlcurl}\mathbf{u}\\ + 2\alpha\mathrm{curl}\boldsymbol{\omega} = \varepsilon\ddot{\mathbf{u}},\\ (2\gamma + \beta)\mathrm{graddiv}\boldsymbol{\omega} - (\gamma + \varepsilon)\mathrm{curlcurl}\boldsymbol{\omega}\\ + 2\alpha\mathrm{curl}\mathbf{u} - 4\alpha\boldsymbol{\omega} = j\ddot{\boldsymbol{\omega}}.\end{aligned} \quad (1)$$

Here, $\mathbf{u}$ is the displacement vector; $\boldsymbol{\omega}$ is the rotation vector; λ, μ are the Lamé coefficients; α, β, γ, and ε are physical constants of the material in the framework of the moment elasticity theory; ρ is the density; and j is the parameter responsible for the inertia measure of the medium under the rotation. We direct the Cartesian coordinate axes x and y along the surface, whereas the z axis is aligned inward the half-space. The boundary condition takes the form

$$\begin{aligned}\sigma_{zx} = 0, \quad \sigma_{zy} = 0, \quad \sigma_{zz} = 0, \quad \mu_{zx} = 0,\\ \mu_{zy} = 0, \quad \mu_{zz} = 0.\end{aligned} \quad (2)$$

CONSTRUCTING THE SOLUTION

Let a wave propagate along the x axis. We represent the general solution of the set of Eqs. (1) in the form of the Fourier integrals, which corresponds to the representation of the solution as that bounded in the time, space, and in Fourier spaces of a wave packet of an arbitrary shape (only the real-valued parts of the corresponding components have a physical sense):

$$\begin{aligned}u_n(x, z, t) = \int_{-\infty}^{\infty} U_n(z)e^{i(kx + ft)}\hat{S}_0(f)df,\\ \omega_n(x, z, t) = \int_{-\infty}^{\infty} W_n(z)e^{i(kx + ft)}\hat{S}_0(f)df.\end{aligned} \quad (3)$$

Here, $n = \{x, y, z\}$ is the coordinate subscript; i is the imaginary unit; k is the wave number; f is the circular frequency; t is time; $U_n(z)$ and $W_n(z)$ are the depth-depending amplitude functions; and $\hat{S}_0(f)$ is the complex-valued Fourier spectrum of the source signal, which determines the wave-packet shape.

We now apply the continuous Fourier transformation to relationships (1)–(3), substitute the Fourier image of the solution into the spectral set, and thus

Institute of Mechanics of Continua, Ural Division, Russian Academy of Sciences, ul. Akademika Koroleva 1, Perm, 614013 Russia
e-mail: kma@icmm.ru; mvp@icmm.ru; shardakov@icmm.ru

1028-3358/05/5011-0601$26.00

obtain two decoupled sets of ordinary differential equations. Further, using the parameters

$$A = X_0\sqrt{\frac{\mu}{B(\gamma+\varepsilon)}}, \quad B = \frac{\alpha+\mu}{\alpha}, \quad C = \frac{\gamma-\varepsilon}{\gamma+\varepsilon},$$

$$C_1^2 = \frac{\lambda+2\mu}{\rho X_0^2 f_0^2}, \quad C_2^2 = \frac{\mu}{\rho X_0^2 f_0^2}, \quad C_3^2 = \frac{BC_2^2}{B-1},$$

$$C_4^2 = \frac{\gamma+\varepsilon}{jX_0^2 f_0^2}, \quad C_5^2 = \frac{\gamma+2\beta}{jX_0^2 f_0^2}$$

(here, X_0 is a certain characteristic size, and f_0 is the characteristic frequency), we make the sets obtained dimensionless.

The solutions to the sets obtained are expressions for the amplitude functions. After their substitution into (3), we finally arrive at

$$u_x(x,z,t) = F_0\int_{-\infty}^{\infty}\left\{-ke^{-\nu_0 z} - \frac{F_1}{k}e^{-\nu_1 z} + \frac{F_2}{k}e^{-\nu_2 z}\right\} \times e^{i(kx+ft-\pi/2)}\hat{S}_0(f)df,$$

$$u_y(x,z,t) = \frac{G_0(B-1)}{2A^2B}\int_{-\infty}^{\infty}\left\{-\frac{G_1}{k\xi_1}\left(a_1 - \frac{f^2}{C_4^2} + \frac{4A^2B}{B-1}\right)e^{-\xi_1 z} + \frac{G_2}{k\xi_2}\left(a_2 - \frac{f^2}{C_4^2} + \frac{4A^2B}{B-1}\right)e^{-\xi_2 z}\right\}e^{i(kx+ft-\pi/2)}\hat{S}_0(f)df,$$

$$u_z(x,z,t) = F_0\int_{-\infty}^{\infty}\left\{-\nu_0 e^{-\nu_0 z} - \frac{F_1}{\nu_1}e^{-\nu_1 z} + \frac{F_2}{\nu_1}e^{-\nu_2 z}\right\} \times e^{i(kx+ft)}\hat{S}_0(f)df,$$

$$\omega_x(x,z,t) = G_0\int_{-\infty}^{\infty}\left\{-ke^{-\xi_0 z} - \frac{G_1}{k}e^{-\xi_1 z} + \frac{G_2}{k}e^{-\xi_2 z}\right\} \times e^{i(kx+ft-\pi/2)}\hat{S}_0(f)df,$$

$$\omega_y(x,z,t) = \frac{F_0 B}{2}\int_{-\infty}^{\infty}\left\{-\frac{F_1}{k\nu_1}\left(a_1 - \frac{f^2}{C_3^2}\right)e^{-\nu_1 z} + \frac{F_2}{k\nu_2}\left(a_2 - \frac{f^2}{C_3^2}\right)e^{-\nu_2 z}\right\}e^{i(kx+ft-\pi/2)}\hat{S}_0(f)df,$$

$$\omega_z(x,z,t) = G_0\int_{-\infty}^{\infty}\left\{-\xi_0 e^{-\xi_0 z} - \frac{G_1}{\xi_1}e^{-\xi_1 z} + \frac{G_2}{\xi_2}e^{-\xi_2 z}\right\}e^{i(kx+ft)}\hat{S}_0(f)df.$$

Here, the exponents of the amplitude functions are determined by the expressions

$$\nu_0 = \sqrt{k^2 - \frac{f^2}{C_1^2}}, \quad \xi_0 = \sqrt{k^2 - \frac{f^2}{C_5^2} + \frac{2A^2BC_4^2}{(B-1)C_5^2}},$$

$$\nu_{1,2} = \xi_{1,2} = \sqrt{k^2 - a_{1,2}},$$

$$a_{1,2} = \frac{C_3^2 + C_4^2}{2C_3^2C_4^2}f^2 - 2A^2 \pm \sqrt{\frac{(C_3^2 - C_4^2)^2}{4C_3^4C_4^4}f^4 - \frac{2A^2(C_2^2C_3^2 - 2C_3^2C_4^2 + C_2^2C_4^2)}{C_2^2C_3^2C_4^2}f^2 + 2A^4}.$$

The real-valued constants F_m and G_m are determined from the dimensionless boundary conditions (2):

$$F_m = (-1)^m ik\nu_m\frac{D_m}{F_0}, \quad G_m = (-1)^m ik\xi_m\frac{E_m}{G_0}, \quad m = 1, 2,$$

where F_0 and G_0 are indeterminate constants and the complex-valued quantities D_m and E_m are the solutions to the homogeneous sets

$$M_1 \cdot \{D_0, D_1, D_2\}^T = 0, \quad M_2 \cdot \{E_0, E_1, E_2\}^T = 0.$$

From the condition for the solvability of these sets, we obtain the following wave equations:

(i) The equation $\det M_1 = 0$ describes the Rayleigh wave with the components u_x, u_z, ω_y, where

$$M_1 = \begin{bmatrix} 2k^2 - \frac{f^2}{C_2^2} & -2ik\nu_1 & -2ik\nu_2 \\ 2ik\nu_0 & 2k^2 - \frac{f^2}{C_2^2} & 2k^2 - \frac{f^2}{C_2^2} \\ 0 & \left(a_1 - \frac{f^2}{C_3^2}\right)\nu_1 & \left(a_2 - \frac{f^2}{C_3^2}\right)\nu_2 \end{bmatrix};$$

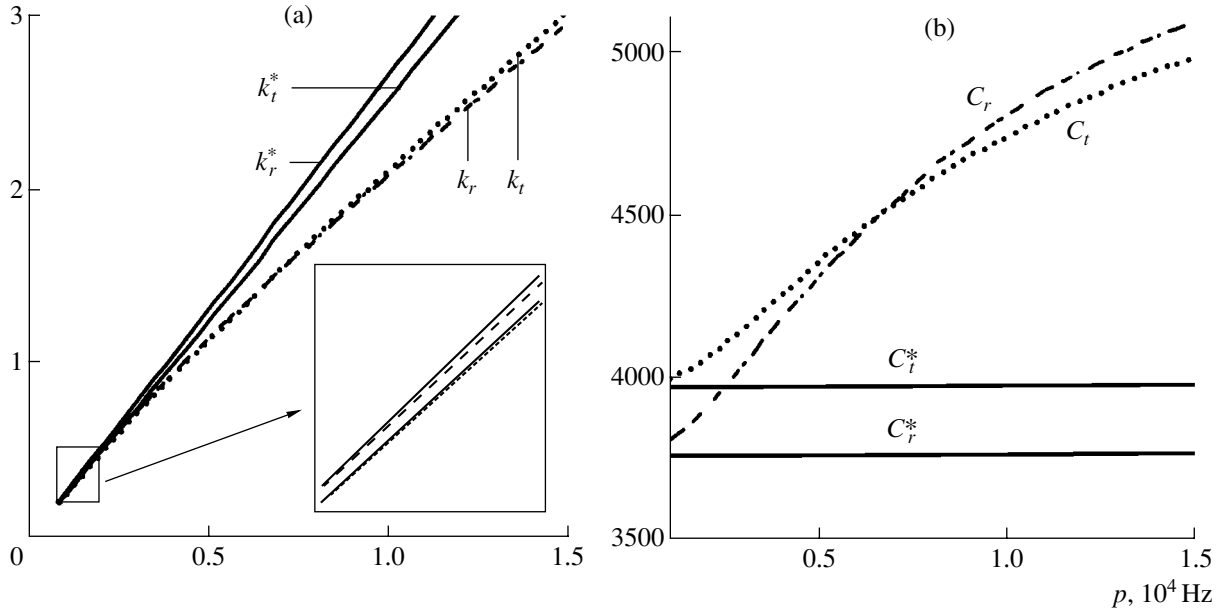

Fig. 1. Comparison of (a) wave numbers and (b) phase velocities for classical and asymmetric media.

(ii) The equation $\det M_2 = 0$ describes the transverse wave with the components u_y, ω_x, and ω_z:

$$M_2 = \begin{bmatrix} \dfrac{2ik}{1-B} & \left(2 + \dfrac{a_1C_4^2 - f^2}{2A^2C_4^2}\right)\xi_1 & \left(2 + \dfrac{a_2C_4^2 - f^2}{2A^2C_4^2}\right)\xi_2 \\ ik(1+C)\xi_0 & k^2C + \xi_1^2 & k^2C + \xi_2^2 \\ \left(\dfrac{2C_5^2}{(1+C)C_4^2} - 1\right)(k^2 - \xi_0^2) - 4\xi_0^2 & 4ik\xi_1 & 4ik\xi_2 \end{bmatrix}.$$

The dependences of the wave numbers and phase velocities on the physical frequency p measured in Hertz are presented in Fig. 1, where k_r^*, C_r^* is the solution for the Rayleigh wave in the classical case; k_t^*, C_t^* is the solution for the bulk transverse wave in the classical case; k_r, C_r is the solution for the Rayleigh wave in the Cosserat medium; and k_t, C_t is the solution for the surface transverse wave in the Cosserat medium.

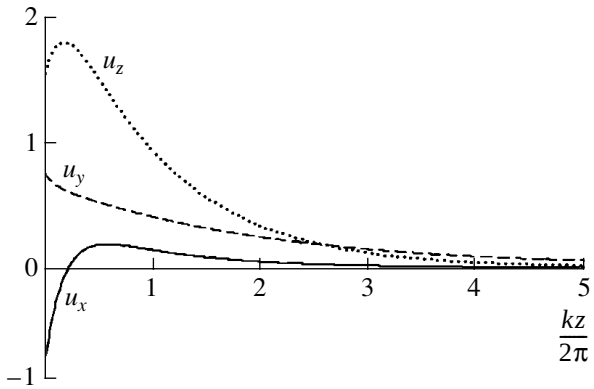

Fig. 2. Displacement components as functions of depth.

Figure 2 shows the displacement components of the solution obtained as a function of the depth normalized to the wavelength. This dependence illustrates that the transverse wave is a typical surface wave, the localization-layer thickness being dependent on the frequency.

CONCLUSIONS

The fundamental result obtained in the present study is the following. In addition to the surface elliptical Rayleigh wave, in a half-space whose dynamic behavior is described by the model of the Cosserat medium, a surface wave having one transverse displacement

component can also exist. From the geometric standpoint, this wave is similar to the Love wave. However, in the classical elasticity theory, the existence of a Love wave is determined by the presence of a certain layer on the half-space. When the layer thickness tends to zero, the Love wave transforms into a bulk wave. Thus, a qualitatively new wave mode is observed in the Cosserat medium. There is no analog of this mode in the classical elasticity theory.

The second result is the existence of a frequency that depends only on the material properties. For this frequency, the propagation velocities in the half-space of the Rayleigh wave and of the transverse surface wave coincide.

REFERENCES

1. W. Nowacki, *Teoria sprézystósci* (PWN, Warszawa, 1970; Mir, Moscow, 1975).
2. V. A. Pal'mov, Prikl. Mat. Mekh. **28**, 401 (1964).
3. V. I. Erofeev, *Wave Processes in Solids Exhibiting Microstructure* (Mosk. Gos. Univ., Moscow, 1999) [in Russian].
4. A. C. Eringen, *Microcontinuum Field Theories*, Vol. 1: *Foundation and Solids* (Springer, New York, 1999), p. 319.
5. A. E. Lyalin, V. A. Pirozhkov, and R. D. Stepanov, Akust. Zh. **28**, 838 (1982).
6. S. Nath, P. R. Sengupta, and L. Debnath, Comput. Math. Appl. **35** (3), 47 (1998).

Translated by G. Merzon

Doklady Physics, Vol. 50, No. 11, 2005, pp. 605–609. Translated from Doklady Akademii Nauk, Vol. 405, No. 3, 2005, pp. 338–342.

MECHANICS

Shape Optimization for Membrane Shells of Revolution

N. V. Banichuk

Presented by Academician I.G. Goryacheva June 7, 2005

Received June 21, 2005

The problems discussed in this paper are concerned with the design of quasi-brittle axisymmetric shells of minimal mass. The considered optimization problems consist in finding the optimal geometry together with the optimal distribution of the shell thickness while giving due account to the constraint imposed on the shell volume. We present the results of the analytic investigation and the exact solution to the problem of the optimal design of the closed shells of revolution exposed to an internal pressure.

STATEMENT OF THE OPTIMIZATION PROBLEM

Consider a shell that has the shape of a surface of revolution and is exposed to axisymmetric actions. The orientation of the meridian plane is determined by angle Θ as calculated from a specified meridian plane, and the orientation of the parallel disk is determined by angle φ between the normal to the surface and the axis of rotation. The radius of the parallel disk, which determines the distance from a point on the neutral shell surface to its axis of rotation, is denoted by $r = r(x)$ (see Fig. 1), where $0 \le x \le L$, $L > 0$, is a given length of the shell. The meridian plane and the plane orthogonal to the meridian are the planes of principal curvatures at the considered point of the shell surface. The corresponding radii of curvature are denoted by r_φ and r_Θ. The thickness distribution $h = h(x)$ is assumed to satisfy the known condition from the theory of thin-walled elastic shells of variable thickness:

$$h(x) \le h_m = \max_x h(x) \ll r_m, \tag{1}$$

$$r_m = \min\{\min_x r_\varphi(x), \min_x r_\Theta(x)\}. \tag{2}$$

In (1) and (2), the minima in x are taken over the closed interval $[0, L]$ and the outer min in (2) denotes the minimum of the two quantities in the braces.

The shell is exposed to a constant internal pressure q and to distributed forces applied to the shell edge and acting parallel to the x-axis. The resulting force applied to the edge is denoted by R. The shell equilibrium equations, which are employed in the determination of the values of normal membrane forces N_φ and N_Θ, have the form [1, 2]

$$\frac{N_\varphi}{r_\varphi} + \frac{N_\Theta}{r_\Theta} = q, \tag{3}$$

$$\frac{2\pi r}{\sqrt{1 + \left(\frac{dr}{dx}\right)^2}} N_\varphi = R + 2\pi q \int_0^x r\left(\frac{dr}{dx}\right) dx = R + \pi q(r^2 - r_1^2), \tag{4}$$

where $r_1 = r(0)$. The internal shearing force $N_{\varphi\Theta}$ is identically zero. The radii of curvature r_φ and r_Θ are calcu-

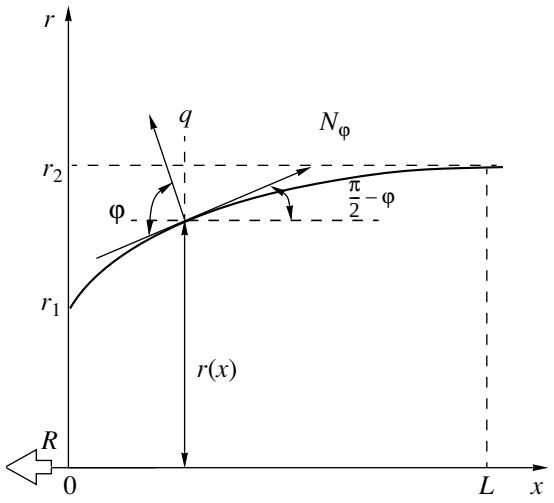

Fig. 1.

Institute for Problems in Mechanics,
Russian Academy of Sciences,
pr. Vernadskogo 101, Moscow, 117526 Russia

1028-3358/05/5011-0605$26.00

lated by the formulae

$$r_\Theta = r\sqrt{1+\left(\frac{dr}{dx}\right)^2},$$
$$r_\varphi = -\left(1+\left(\frac{dr}{dx}\right)^2\right)^{3/2}\left(\frac{d^2r}{dx^2}\right)^{-1}. \quad (5)$$

It follows from (3)–(5) that the corresponding stresses satisfy the following relations:

$$\sigma_\varphi = \frac{N_\varphi}{h} = \frac{R+\pi q(r^2-r_1^2)}{2\pi rh}\sqrt{1+\left(\frac{dr}{dx}\right)^2}, \quad (6)$$

$$\sigma_\Theta = \frac{N_\Theta}{h} = \frac{qr}{h}\sqrt{1+\left(\frac{dr}{dx}\right)^2} + \frac{R+\pi q(r^2-r_1^2)}{2\pi h\sqrt{1+\left(\frac{dr}{dx}\right)^2}}\left(\frac{d^2r}{dx^2}\right). \quad (7)$$

The considered optimization problem consists in finding a shape $r = r(x)$ and a distribution of the shell thickness $h = h(x)$ that afford a minimum to the volume of the shell material

$$J = 2\pi\int_0^L rh\sqrt{1+\left(\frac{dr}{dx}\right)^2}dx \quad (8)$$

and satisfy the strength condition [3–6]

$$\max\{\sigma_\varphi, \sigma_\Theta\} \le \sigma_*, \quad (9)$$

the boundary conditions imposed on function $r(x)$

$$r(0) = r_1, \quad r(L) = r_2 \quad (10)$$

and an additional geometric constraint imposed on the shell volume

$$V = \pi\int_0^L r^2dx = V_0, \quad (11)$$

where σ_*, r_1, r_2, and V_0 are given positive constants. The strength condition may be written in the form of (9) in the case of brittle or quasi-brittle axisymmetric shells. Here, the material strength constant σ_* (the reduced critical stress) is determined by the known values of the material quasi-brittle strength constant K_{1c} and by the maximum allowed values of the initial cracks of a normal fracture l_m arising in the process of the production of the shell or in the process of its exploitation [5, 6].

SOME PROPERTIES OF THE OPTIMAL SOLUTION

In the construction of the optimal solution, we assume that, throughout the whole interval $x \in [0, L]$, inequality (9) turns into an equality, i.e., either

$$\sigma_\varphi = \frac{N_\varphi}{h} = \sigma_*, \quad \sigma_\Theta \le \sigma_* \quad (12)$$

or

$$\sigma_\Theta = \frac{N_\Theta}{h} = \sigma_*, \quad \sigma_\varphi \le \sigma_*. \quad (13)$$

Let us justify this assumption and demonstrate that, for the optimal shell, there are no fragments of the closed interval $[0, L]$ where the strict inequality in (9) is realized. Suppose, by contradiction, that, on a certain segment $[x_1, x_2]$ $(0 \le x_1 < x_2 \le L)$, the optimal solution $(r_0^*(x), h^*(x))$ satisfies the strict inequality in (9), i.e.,

$$h^* > \frac{N_\varphi}{\sigma_*}, \quad h^* > \frac{N_\Theta}{\sigma_*}.$$

On the other segments $0 \le x < x_1$ and $x_2 < x \le L$ of the closed interval $[0, L]$, it is assumed that the considered optimal solution $(r^*(x), h^*(x))$ will satisfy either (12) or (13); i.e., it is assumed that inequality (9) will turn into an equality. In this case, we can construct an admissible design $(\hat r(x), \hat h(x))$ in the following way:

$$\hat r = r^*, \quad \hat h = h^*, \quad \text{if} \quad 0 \le x \le x_1,$$
$$x_2 < x \le L,$$
$$\hat r = r^*, \quad \hat h = \frac{N_\varphi(r^*)}{\sigma_*} < h^* \quad \text{or} \quad (14)$$
$$\hat h = \frac{N_\Theta(r^*)}{\sigma_*} < h^*, \quad x_1 \le x \le x_2.$$

This design $(\hat r_0, \hat h)$ is admissible because the above distributions $\hat r(x)$ and $\hat h(x)$ satisfy the strength condition (9) and the isoperimetric constraint (11) imposed on the shell volume. Note that the admissible design (14) satisfies the equality in (9) throughout the entire closed interval $[0, L]$. Thus, the constructed admissible solu-

tion is a full-strength design and, for this solution, we have

$$\begin{aligned} J(\hat{r}, \hat{h}) &= 2\pi\int_0^{x_1} r^* h^* \sqrt{1+\left(\frac{dr^*}{dx}\right)^2}\,dx \\ &+ 2\pi\int_{x_1}^{x_2} r^* \hat{h} \sqrt{1+\left(\frac{dr^*}{dx}\right)^2}\,dx \\ &+ 2\pi\int_{x_2}^{L} r^* h^* \sqrt{1+\left(\frac{dr^*}{dx}\right)^2}\,dx \\ &< 2\pi\int_0^{L} r^* h^* \sqrt{1+\left(\frac{dr^*}{dx}\right)^2}\,dx = J(r^*, h^*). \end{aligned} \tag{15}$$

The reverse inequality $J(r^*, h^*) > J(\hat{r}, \hat{h})$, established in (15), proves the assertion that, for the optimal solution, the strict equality in (9) is realized throughout the entire closed interval $[0, L]$.

CONSTRUCTION OF THE OPTIMAL SHAPE AND THE OPTIMAL THICKNESS DISTRIBUTION

Consider the problem of the optimal design of a closed shell exposed to an internal pressure: $r(0) = 0$, $r(L) = 0$. Here, we assume that $R = 0$. First, suppose relations (12) to be valid throughout the entire closed interval $[0, L]$. In this case, the optimal thickness distribution and the corresponding optimal shape of the shell are related by the formula

$$h_\varphi = \frac{qr}{2\sigma_*}\sqrt{1+\left(\frac{dr}{dx}\right)^2}. \tag{16}$$

With the use of (16), we come to the following expressions for the mass to be minimized (the functional of the problem) and for the extended Lagrange functional:

$$\begin{aligned} J &= 2\pi\int_0^{L} r h_\varphi \sqrt{1+\left(\frac{dr}{dx}\right)^2}\,dx \\ &= \frac{\pi q}{\sigma_*}\int_0^{L} r^2\left[1+\left(\frac{dr}{dx}\right)^2\right]dx, \end{aligned} \tag{17}$$

$$J^a = J - \lambda V = \frac{\pi q}{\sigma_*}\int_0^{L}\left\{r^2\left[1+\left(\frac{dr}{dx}\right)^2\right] - \frac{\lambda\sigma_*}{q}r^2\right\}dx. \tag{18}$$

Under the assumption that $r(x) \neq 0$, the necessary condition of extremum for the Lagrange functional (18) (the Euler equation) can be written for $x \in (0, L)$ as

$$r\frac{d^2r}{dx^2} + \left(\frac{dr}{dx}\right)^2 - \frac{\beta}{2} = 0, \quad \beta = 2\left(1 - \frac{\lambda\sigma_*}{q}\right). \tag{19}$$

Here, determination of the shape of an optimal closed shell reduces to the solution of the following boundary-value problem:

$$\frac{d^2}{dx^2}(r^2) = \beta, \quad r(0) = r(L) = 0. \tag{20}$$

By virtue of (20), we have

$$r = r(x) = \alpha L\sqrt{\frac{x}{L}\left(1-\frac{x}{L}\right)}, \quad \alpha = \sqrt{-\frac{\beta}{2}}. \tag{21}$$

The Lagrange multiplier λ can be found from the isoperimetric constraint (11) imposed on the shell volume. We have

$$\lambda = \frac{q}{\sigma_*}\left(1+\frac{6V_0}{\pi L^3}\right), \quad \beta = -\frac{12V_0}{\pi L^3}, \quad \alpha = \sqrt{\frac{6V_0}{\pi L^3}}. \tag{22}$$

The optimal thickness distribution $h_\varphi(x)$ that corresponds to the obtained optimal shape (21), (22) is determined by relation (16) and can be written in the form

$$h_\varphi = \frac{q\alpha L}{4\sigma_*}\sqrt{\alpha^2 + 4(1-\alpha^2)\frac{x}{L}\left(1-\frac{x}{L}\right)}. \tag{23}$$

For this design, the minimal mass of the shell is given by the formula

$$J = \frac{\pi q L^3}{12\sigma_*}\alpha^2(1+\alpha^2). \tag{24}$$

The existence domain for the solution of the considered form is determined by the condition $\sigma_\Theta(x) \leq \sigma_\varphi(x) = \sigma_*$ ($x \in [0, L]$). Rearrange this condition in the form of the inequality

$$\sigma_\Theta = \sigma_*\left[2 + \left(\frac{dr}{dx}\right)^2 + \frac{\beta}{2}\right]\left(1+\left(\frac{dr}{dx}\right)^2\right)^{-1} \leq \sigma_*, \quad 0 \leq x \leq L,$$

whose solution yields a constraint on the main dimensionless parameter of the problem

$$\alpha^2 \equiv \frac{6V_0}{\pi L^3} \geq 1. \tag{25}$$

The obtained optimal shapes $r(x)$ and thickness dis-

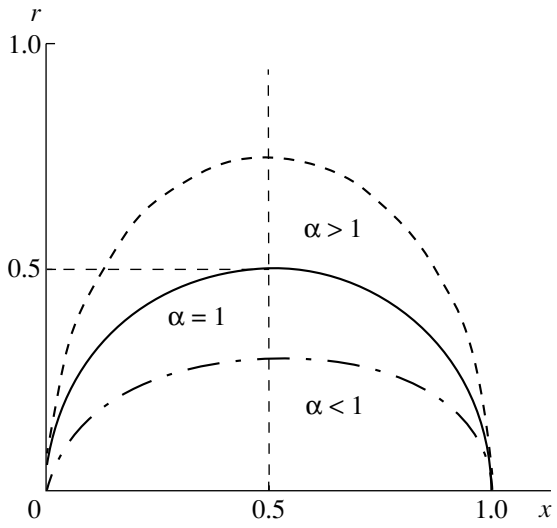

Fig. 2.

tributions $h(x)$ are shown as dashed lines in Figs. 2 and 3, respectively, in dimensionless variables $\tilde{r} = \frac{r}{L}$, $\tilde{h} = h\frac{4\sigma_*}{qL}$, and $\tilde{x} = \frac{x}{L}$. It is seen from these figures that, for $\alpha > 1$, the optimal shell has the shape of an oblate ellipsoid of revolution

$$r^2 + \alpha^2\left(x - \frac{1}{2}\right)^2 = \frac{\alpha^2}{4},$$

and the thickness attains its maximum at the poles of the ellipsoid. As $\alpha \longrightarrow 1$, the shape of the optimal shell tends to a sphere and the distribution of its thickness tends to the uniform one. Figure 4 shows the dimensionless mass of the shell versus parameter α in dimensionless form $\tilde{J} = J\left(\frac{\pi q L^3}{12\sigma_*}\right)^{-1}$ (below, the tilde is omitted) for $\alpha \geq 1$.

Now, consider the case where relations (13) are valid throughout the entire closed interval $[0, L]$. Then, the optimal shape $r = r(x)$ of the shell is related to the corresponding thickness distribution $h = h(x)$ by the expression

$$h_\Theta = \frac{qr}{2\sigma_*}\left\{\frac{r\frac{d^2r}{dx^2} + 2\left(\frac{dr}{dx}\right)^2 + 2}{\sqrt{1 + \left(\frac{dr}{dx}\right)^2}}\right\}. \quad (26)$$

By virtue of this relation, the expression for the shell mass to be minimized and for the extended Lagrange functional may be put in the following form:

$$J = 2\pi\int_0^L rh_\Theta\sqrt{1 + \left(\frac{dr}{dx}\right)^2}\,dx = \frac{\pi q}{\sigma_*}\int_0^L r^2\left[r\frac{d^2r}{dx^2} + 2\left(\frac{dr}{dx}\right)^2 + 2\right]dx, \quad (27)$$

$$J^a = J - \lambda V = \frac{\pi q}{\sigma_*}\int_0^L\left\{r^2\left[r\frac{d^2r}{dx^2} + 2\left(\frac{dr}{dx}\right)^2 + 2\right] - \frac{\lambda\sigma_*}{q}r^2\right\}dx. \quad (28)$$

The Euler equation written for the extended

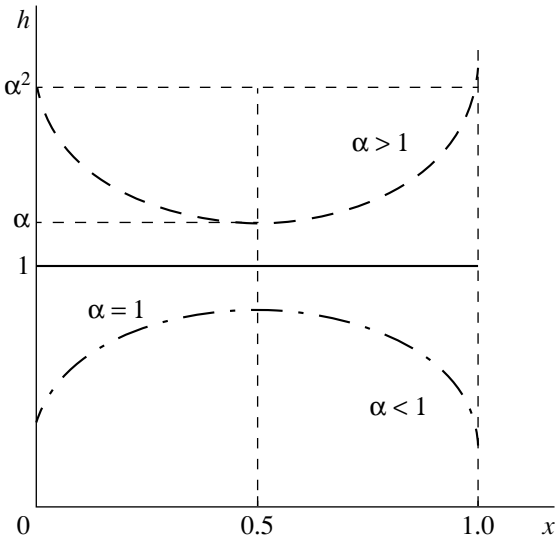

Fig. 3.

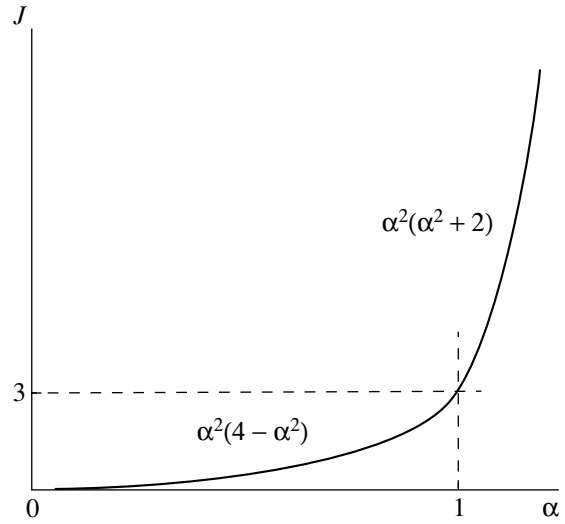

Fig. 4.

Lagrange functional (28) has the form

$$r\frac{d^2r}{dx^2}+\left(\frac{dr}{dx}\right)^2-\frac{\gamma}{2}=0,\quad \gamma=2\left(\frac{\lambda\sigma_*}{q}-2\right). \qquad (29)$$

Together with (10), it sets the following boundary-value problem for the determination of the optimal shape $r(x)$ of the shell:

$$\frac{d^2}{dx^2}(r^2)=\gamma,\quad r(0)=r(L)=0. \qquad (30)$$

The optimal design determined by relations (26) and (30) and isoperimetric constraint (11) intended for finding the Lagrange multiplier λ has the form

$$r=r(x)=\alpha L\sqrt{\frac{x}{L}\left(1-\frac{x}{L}\right)},\quad 0\le x\le L; \qquad (31)$$

$$h_\Theta=\frac{qL}{4\sigma_*}\frac{\alpha^2\left[1+8\left(\frac{1}{\alpha^2}-1\right)\frac{x}{L}\left(1-\frac{x}{L}\right)\right]}{\sqrt{1+4\left(\frac{1}{\alpha^2}-1\right)\frac{x}{L}\left(1-\frac{x}{L}\right)}}; \qquad (32)$$

$$\lambda=2\frac{q}{\sigma_*}\left(1-\frac{3V_0}{\pi L^3}\right),\quad \gamma=-\frac{12V_0}{\pi L^3},\quad \alpha=\sqrt{\frac{6V_0}{\pi L^3}}. \qquad (33)$$

The existence domain for the optimal solution (31)–(33) is found from the strength condition $\sigma_\varphi\le\sigma_\Theta=\sigma_*$ $(0\le x\le L)$. Substituting the expressions for σ_φ and σ_Θ into this condition, we come to the relation $\frac{d^2(r^2)}{dx^2}+2\ge 0$ and establish the following inequality for the main dimensionless parameter of the optimization problem:

$$\alpha^2=\frac{6V_0}{\pi L^3}\le 1. \qquad (34)$$

This inequality guarantees the existence of a solution of the form (31)–(33). For this design, the shell mass depends on the dimensionless parameter α in the following way:

$$J=\frac{\pi qL^3}{12\sigma_*}\alpha^2(4-\alpha^2).$$

This dependence is depicted in Fig. 4 in the dimensionless form $\tilde J=J\left(\frac{\pi qL^3}{12\sigma_*}\right)^{-1}$ for $\alpha\le 1$. The corresponding optimal shapes of the shells and thickness distributions are shown as dot-and-dash lines in Figs. 2 and 3, respectively, in dimensionless variables $\tilde r=\frac{r}{L}$, $\tilde h=h\frac{4\sigma_*}{qL}$, and $\tilde x=\frac{x}{L}$. It is seen from these figures that, for $\alpha<1$, the optimal shell has the shape of an oblong ellipsoid of revolution and the thickness attains its maximum at $x=0.5$. The case of $\alpha=1$ corresponds to a spherical shell with a uniform thickness distribution.

CONCLUSIONS

In this paper, a new problem of the optimal design of a thin-walled axisymmetric shell exposed to an internal pressure with regard for strength constraints has been formulated and solved. The mass of the shell was taken as the functional to be minimized; and the shape of the shell (the meridian equation) and the distribution of the thickness over the meridian were treated as the design variables. The joint use of two control functions made it possible both to significantly diminish the mass of the designed shell and to essentially simplify the analysis of the considered optimization problem. Then, the optimal solution to the problem of shell design was shown to depend on a single dimensionless parameter characterizing the degree of oblateness or oblongness of an axisymmetric shell. The finding of the optimal shape and the optimal thickness distribution of an axisymmetric shell yielded an analytic definition of solutions of two types, namely, oblate lens-shaped shells and oblong cigar-shaped shells. For these types of solutions, the optimal thickness distributions are qualitatively different. However, as the key parameter takes the value that separates the types of solutions, the obtained shapes and thickness distributions continuously change into one another.

ACKNOWLEDGMENTS

This work was supported by the Netherlands Organization for Scientific Research, project NWO no. 047.014.007, and by the Division of Machine Engineering, Mechanics, and Control Processes Problems of the Russian Academy of Sciences, program “Accumulation of Damage, Destruction, Wear Processes and Structural Changes in Materials under Intensive Mechanical, Thermal, and Radiation Effects.”

REFERENCES

1. S. P. Timoshenko and S. Woinowsky-Krieger, *Theory of Plates and Shells*, 2nd ed. (McGraw-Hill, New York, 1959; Nauka, Moscow, 1966).
2. V. V. Novozhilov, K. F. Chernykh, and E. I. Mikhaĭlovskiĭ, *Linear Theory of Fine Shells* (Politekhnika, Leningrad, 1991) [in Russian].
3. M. F. Kanninen and C. H. Popelar, *Advanced Fracture Mechanics* (Oxford Univ. Press, New York, 1985).
4. E. S. Folias, in *Fracture: A Topical Encyclopedia of Current Knowledge* (Krieger, Malabar, 1998), pp. 275–288.
5. N. V. Banichuk, Dokl. Akad. Nauk **358** (1), 40 (1998).
6. N. V. Banichuk, Izv. Ross. Akad. Nauk, Mekh. Tverd. Tela, No. 5, 99 (2002).

Translated by A. Pankrat’ev

Doklady Physics, Vol. 50, No. 11, 2005, pp. 610–612. Translated from Doklady Akademii Nauk, Vol. 405, No. 3, 2005, pp. 343–345.

MECHANICS

Integral Equations in Inverse Problems of the Determination of the Coefficients of Differential Operators in the Theory of Elasticity

A. O. Vatul'yan

Presented by Academician V.A. Babeshko April 28, 2005

Received May 24, 2005

In recent years, inverse problems related to the determination of the coefficients of differential operators have more and more often come to the attention of researchers in connection with the identification and refinement of models in various areas of the natural sciences. In some cases, the model of homogeneous isotropic elasticity theory, which plays a key role in the modern practice of structure integrity analysis, is in need of refinement: the assumption of the homogeneity of the medium should be rejected (in geophysics and nanotechnologies). Moreover, determination of the moduli of elasticity as functions of the coordinates based on experimental data necessitates the solution of inverse problems. By now, rather extensive experience has been acquired in the investigation into the inverse problems of the theory of elasticity. This experience has mainly been based on models for the half-space in a nonstationary statement, which lead to the solution of nonlinear integral Volterra equations [1–3]. In this paper, we suggest new integral equations to which the inverse problems for finite bodies can be reduced by the linearization procedure in the case of steady-state vibrations. Some examples are considered.

RECIPROCITY RELATIONS

Consider the problem of steady-state vibrations at frequency ω of a simply connected bounded domain V with boundary $S = S_u \cup S_\sigma$. Here, we distinguish between two states: the first state corresponds to the elastic constant tensor $C^{(1)}_{ijkl}(x)$, translation vector components $u^{(1)}_i$, and stress tensor $\sigma^{(1)}_{ij}$; the second, to $C^{(2)}_{ijkl}(x)$, $u^{(2)}_i$, and $\sigma^{(2)}_{ij}$, respectively. Within domain V, each state satisfies the equations of motion and Hooke's law:

$$\begin{aligned} \sigma^{(m)}_{ij,\,j} + \rho\omega^2 u^{(m)}_i &= 0, \quad i = 1, 2, 3, \\ \sigma^{(m)}_{ij} &= C^{(m)}_{ijkl} u^{(m)}_{k,\,l}, \quad m = 1, 2. \end{aligned} \tag{1}$$

The boundary conditions are the same for both states:

$$u_i\big|_{S_u} = 0, \quad \sigma_{ij} n_j\big|_{S_\sigma} = p_i. \tag{2}$$

Theorem 1. *Reciprocal states that meet conditions* (1) *and* (2) *satisfy the relation*

$$\int_V (C^{(2)}_{ijkl} - C^{(1)}_{ijkl}) u^{(2)}_{k,\,l} u^{(1)}_{i,\,j}\, dV + \int_{S_\sigma} p_i (u^{(2)}_i - u^{(1)}_i)\, dS = 0. \tag{3}$$

In the case where $C^{(1)}_{ijkl}(x) = C^{(2)}_{ijkl}(x)$, the volume integral in (3) vanishes and we come to the known Betti relation in the absence of body forces [4].

Relation (3) enables us to formulate operator expressions that relate the elastic characteristics of domain V to the boundary fields of translations and stresses on S.

INVERSE COEFFICIENT PROBLEM

Let us formulate the problem for the determination of the moduli of elasticity as functions of the coordinates by the information

$$u_i\big|_{S_\sigma} = f_i(x, \omega), \quad \omega \in [\omega_1, \omega_2], \tag{4}$$

which corresponds to the measurement of the translation field over part S_σ of the boundary exposed to the load and simulates the echo regime in acoustic methods for nondestructive testing. Note that, in the statement of inverse problems, the translation field on the unloaded part of the boundary is generally assumed to be known. However, in this case, the system of resulting equations contains intermediate unknown functions.

Rostov State University,
pr. Stachki 194/3, Rostov-on-Don, 344104 Russia

1028-3358/05/5011-0610$26.00

The problem of the determination of the moduli of elasticity is nonlinear [2, 3]. It may be solved by a certain iterative process, each stage of which solves a linear problem. Assuming

$$u_i^{(1)} = u_i^{(0)}, \quad u_i^{(2)} = u_i^{(0)} + \nu_i, \quad C_{ijkl}^{(1)} = C_{ijkl}^{(0)},$$
$$C_{ijkl}^{(2)} = C_{ijkl}^{(0)} + R_{ijkl}$$

and retaining the linear (in ν_i and R_{ijkl}) terms in (3), with due account taken of the additional condition (4), we obtain

$$\int_V R_{ijkl} u_{k,l}^{(0)} u_{i,j}^{(0)} dV + \int_{S_\sigma} p_i (f_i - u_i^{(0)}) dS = 0, \qquad (5)$$
$$\omega \in [\omega_1, \omega_2].$$

Relation (5) may be treated as an integral equation in components $R_{ijkl}(x)$ provided that the direct problem of the distribution of the translation field within domain V and on its boundary S with elastic characteristics $C_{ijkl}^{(0)}(x)$ (the reference field) is solved beforehand. In the isotropic case, the elastic constant tensor is expressed in terms of two Lamé functions $\lambda(x)$ and $\mu(x)$ and Eq. (5) takes the form

$$\int_V \Big[\lambda^{(1)}(x)(u_{k,k}^{(0)})^2 + \frac{1}{2}\mu^{(1)}(x)(u_{i,j}^{(0)} + u_{j,i}^{(0)}) \times (u_{i,j}^{(0)} + u_{j,i}^{(0)})\Big] dV + \int_{S_\sigma} p_i [f_i - u_i^{(0)}] dS = 0, \qquad (6)$$
$$\omega \in [\omega_1, \omega_2].$$

Functions $\lambda^{(1)}(x)$ and $\mu^{(1)}(x)$ are determined from integral equation (6) by the regularizing procedure [5] given the prior information that they are positive and depend on a single coordinate. Note that, in shape, the volume integrand in (5) and (6) is an analog of the doubled modulus of resilience, where the deformations correspond to the reference field and the moduli, to the other field. The surface integral characterizes the work of the given load on the additional fields of translations, which indicate the difference on the boundary S_σ between the components of the reference field of translations and the translations specified in the inverse problem. The discretization of the integral operator on the basis of the simplest quadrature formulas gives a system of linear algebraic equations in nodal values of functions $\lambda^{(1)}(x)$ and $\mu^{(1)}(x)$. This system turns out to be ill-conditioned and regularizing algorithms must be applied if it is to be used.

Remark. One can obtain additional integral relations in the form of (5), (6) for determination of the elastic characteristics when the load shape or domain is changed. In this case, $u_i^{(0)}$ and $f_i(x, \omega)$ in relations (5) and (6), respectively, are changed.

Examples

1. *Antiplane vibrations of a bar of cross-section S*, $\partial S = l = l_1 \cup l_2$, $\mu = \mu(x_1)$, are described by the following boundary-value problem:

$$\frac{\partial}{\partial x_1}\Big(\mu \frac{\partial u}{\partial x_1}\Big) + \frac{\partial}{\partial x_2}\Big(\mu \frac{\partial u}{\partial x_2}\Big) + \rho\omega^2 u = 0,$$
$$u|_{l_1} = 0, \quad \mu \frac{\partial u}{\partial n}\Big|_{l_2} = p. \qquad (7)$$

Under an additional condition of the form (4), the corresponding integral equation in the inverse problem $u|_{l_2} = f(x, \omega)$ has the form

$$\int_S \mu^{(1)} \Big[\Big(\frac{\partial u^{(0)}}{\partial x_1}\Big)^2 + \Big(\frac{\partial u^{(0)}}{\partial x_2}\Big)^2\Big] dS$$
$$+ \int_{l_2} p(f - u^{(0)}) dl_x = 0, \quad \omega \in [\omega_1, \omega_2]. \qquad (8)$$

2. *Longitudinal vibrations of a rod of length l with a variable Young modulus E = E(x)*. The boundary value-problem for the longitudinal vibrations of a rod has the form

$$(E(x)u')' + \rho\omega^2 u = 0, \quad u(0) = 0,$$
$$E(l)u'(l) = p, \qquad (9)$$

while, in the inverse problem, $u(l, \omega) = f(\omega)$, $\omega \in [\omega_1, \omega_2]$, is specified. Then, Eq. (5) reduces to

$$\int_0^l E_1(x)(u_0')^2 dx + p(-u_0(l, \omega) + f(\omega)) = 0,$$
$$\omega \in [\omega_1, \omega_2], \qquad (10)$$

where $u_0(x, \omega)$ is the solution to problem (9) with the known Young modulus $E_0(x)$. In the particular case of $E_0 = \text{const}$, we have

$$u_0(x, \omega) = p_0 \frac{\sin kx}{k \cos kl}, \quad k = \omega\sqrt{\frac{\rho}{E_0}}, \quad p_0 = \frac{p}{E_0}$$

and Eq. (10) assumes the form of the first kind Fredholm integral equation with a smooth kernel

$$\int_0^l E_1(x) \cos^2 kx dx = F(k), \quad k \in [k_1, k_2]. \qquad (11)$$

The following assertion is valid.

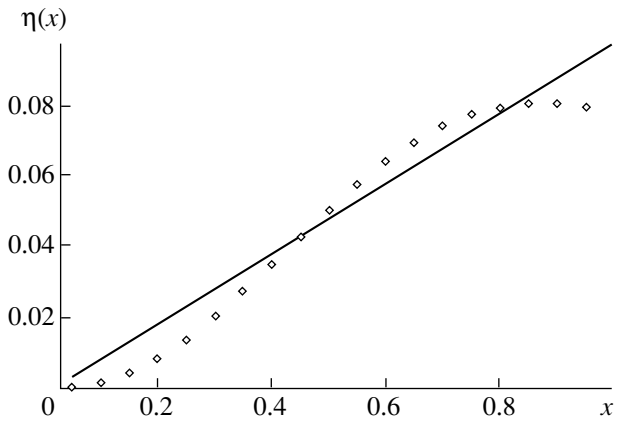

(Solid line) exact and (dotted line) reconstructed solutions.

Theorem 2. *Equation* (11) *has a unique solution in* $E_1(x) \in L_2[0, l]$ *provided that there are no resonance wave numbers of problem* (9) *within the closed interval* $[k_1, k_2]$.

The figure presents the results of the model numerical experiment on the reconstruction of function $E(x) = E_0(1 + \eta(x))$, $\eta(x) = \frac{x}{10}$, $l = 1$. The solid line shows function $\eta(x)$; the dotted line depicts the solution obtained by Tikhonov's regularization method applied to the integral equation (11). The range of wave numbers has been varied: below the first wave number and between the first and second wave numbers. The reconstruction error is within 15%; moreover, the deviation of the obtained solution from the exact one attains its maximum on the loose end of the rod.

ACKNOWLEDGMENTS

This work was supported by the Russian Foundation for Basic Research, project no. 05-01-00734, and by the Council of the President of the Russian Federation for the Support of Young Russian Scientists and Leading Scientific Schools (project no. NSh-2113.2003).

REFERENCES

1. V. G. Romanov, *Inverse Problems of Mathematical Physics* (Nauka, Moscow, 1984; VNU Science Press, Utrecht, 1987).
2. V. G. Yakhno, *Inverse Problems for Differential Equations of Elasticity* (Nauka, Novosibirsk, 1990) [in Russian].
3. H. D. Bui, *Inverse Problems in the Mechanics of Materials: An Introduction* (CRC, Boca Raton, 1994).
4. W. Nowacki, *Teoria sprézystoósci* (PWN, Warszawa, 1970; Mir, Moscow, 1975).
5. A. N. Tikhonov and V. Ya. Arsenin, *Solutions of Ill-Posed Problems*, 2nd ed. (Halsted, New York, 1977; Nauka, Moscow, 1986).

Translated by A. Pankrat'ev

Doklady Physics, Vol. 50, No. 11, 2005, pp. 613–617. Translated from Doklady Akademii Nauk, Vol. 405, No. 3, 2005, pp. 346–350.

MECHANICS

Dynamically Equilibrium Shapes of Ocean-Flow Rings

I. P. Semenova and L. N. Slezkin

Presented by Academician S.S. Grigoryan November 26, 2004

Received November 29, 2004

Rings are near-surface mesoscale vortex forms (with horizontal sizes on the order of ~10^2 km) that arise as a result of meandering ocean flows [1, 2]. These flows propagate along frontal zones separating water masses that substantially differ in terms of their temperature, salinity, density, and other characteristic properties. Among them, rings of the Gulf Stream and Kurosio are the most well known.

The generation of rings by meandering ocean flows is the basic mechanism by which water masses are transferred across frontal zones. Rings similar to flooded lens vortices [3, 4] are vortex forms of an intrusive nature. Full-scale observations show that for the Gulf Stream and Kurosio rings formed to the north and south of the flows rotate in the anticyclonic and cyclonic directions, respectively. Anticyclonic Gulf-Stream rings have a significant warm and salt core containing captured water of the Sargasso Sea; cyclonic rings contain a cold and fresher core of subarctic water captured to the north–west of the flow [2]. In this study, we determine dynamically equilibrium shapes of a density-homogeneous rotating mass of liquid (of a ring) in the near-surface layer of a quiescent stratified ocean residing on the rotating Earth. Our analysis allows for the vertical and horizontal projections of the Earth's angular velocity. For a linearly stratified ocean, the exact solution is obtained for shapes of the interface that separates water masses and ring-free boundaries. For real parameters of the phenomenon, the separation surface of the anticyclonic ring is part of a three-axis ellipsoid, whereas the separation surface of a cyclonic ring is part of a two-sheeted elliptic hyperboloid or elliptic cone, which is also inclined to the horizon. The free surface of the anticyclonic ring is part of an elliptic paraboloid that elevates over the unperturbed oceanic surface. At the same time, the free surface of the cyclonic ring is part of an elliptic paraboloid (funnel) that is located below the ocean surface, which corresponds to ring-surface observations based on data obtained with artificial satellites. The inclinations of the principal axes of boundary surfaces for cyclonic and anticyclonic vortices differ in both their sign and magnitude.

Similar to flooded vortices, i.e., lenses [4, 5], near-surface rings can be considered as full-scale liquid gyroscopes residing on the rotating base. A water mass rotating with respect to the Earth has a proper moment of momentum whose vector rotates (precesses) together with the Earth and, thus, changes its orientation in absolute space. This variation is possible only under the action of the moment of external forces. The moment of forces exists even in the absence of the translational motion of a rotating mass as a whole with respect to the Earth. Ignoring friction (in the approximation of an idealized model), the only moment of forces that can be responsible for the indicated change of the orientation is the moment of hydrostatic forces in the stratified ocean. This moment acts upon the dynamically equilibrium shape of the rotating liquid mass that has arisen.

The rings exist for a sufficiently long time, from several months (anticyclonic rings) to two years (cyclonic rings). Moving in the ocean, preferably to the southwest, they propagate for hundreds of kilometers [6]. In the opinion of the authors of [6], the long lifespan of these rings is, in particular, explained by the existence under actual conditions of a shape that is close to the dynamically equilibrium shape of the idealized model.

We now formulate the hydrodynamic problem. A rotating ideal incompressible liquid of finite volume, which has the homogeneous density ρ, is immersed into a stratified ocean. The ocean is quiescent with respect to the Earth, which rotates at an angular velocity $\mathbf{\Omega}$. By virtue of the smallness of the characteristic size of the phenomenon under study compared to the Earth's radius, the non-sphericity of the Earth is not taken into account. We perform our consideration in the plane layer of a stratified perfect liquid, which is tangent to the Earth's surface and is placed in the plane-parallel gravity field. Based on the condition of the equality of pressures at the interface of the flooded part and the pressure steadiness (pressure is assumed to be zero) at the free boundary separating the ring from the atmosphere, we construct a dynamically equilibrium shape of the water-mass separation surface.

We introduce the Cartesian coordinate system x, y, z, the z axis being directed upward. The plane $z = 0$ is

Institute of Mechanics, Moscow State University, Michurinskiĭ pr. 1, Moscow, 119192 Russia

1028-3358/05/5011-0613$26.00

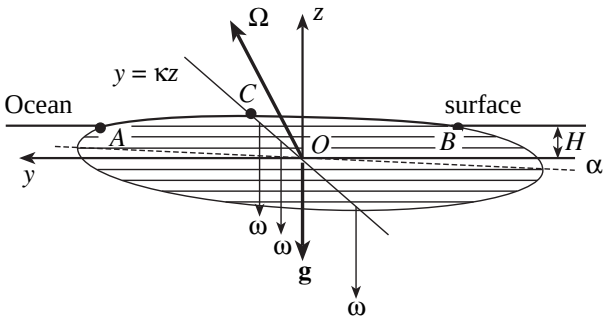

Fig. 1.

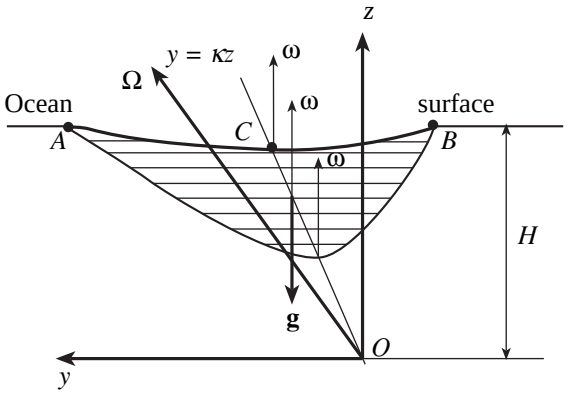

Fig. 2.

located at a depth corresponding to the density of the homogeneous formation. The *x* and *y* axes are directed to the east and north, respectively.

In order to describe the motion within a ring, we exploit hydrodynamic equations written in the Gromeka–Lamb form in the coordinate system associated with the rotating Earth:

$$\begin{gathered}\mathrm{div}\mathbf{V} = 0,\\ (2\boldsymbol{\Omega} + \mathrm{curl}\mathbf{V}) \times \mathbf{V} = -\frac{1}{\rho}\mathrm{grad}\Phi,\ \Phi = p + 0.5\rho\mathbf{V}^2 + \rho g z.\end{gathered} \tag{1}$$

Here, **V** is the vector of the relative velocity for the liquid, ρ is its density, *p* is pressure, and **Ω** is the vector of the Earth's angular velocity.

We write the relative velocities within the ring as

$$u = -\omega(y - \kappa z), \quad v = \omega x, \quad w = 0, \quad \omega = \text{const}. \tag{2}$$

This velocity field corresponds to the plane circular motion with respect to the Earth, with the centers of the circles being located in the straight line $y = \kappa z$ lying in the meridian plane. The angular velocity ω for the motion is identical for all horizontal cross sections. The point *O* of the intersection of this straight line with the plane $z = 0$ is taken as the origin. The meridian cross sections passing through the point *O* are schematically shown in Figs. 1 and 2 for anticyclonic and cyclonic rings, respectively.

Based on a direct verification, we are easily convinced of the validity of the continuity equation.

The set of Eqs. (1), written in projections onto the coordinate axes, takes the form (ρ_r is the ring density)

$$\begin{gathered}x\omega(2\Omega_z + 2\omega) = \frac{1}{\rho_r}\frac{\partial\Phi}{\partial x},\\ \omega(y - \kappa z)(2\Omega_z + 2\omega) = \frac{1}{\rho_r}\frac{\partial\Phi}{\partial y},\\ -\omega(y - \kappa z)(2\Omega_y + \kappa\omega) = \frac{1}{\rho_r}\frac{\partial\Phi}{\partial z}.\end{gathered} \tag{3}$$

The projections with respect to the vortex are (0, ωκ, 2ω); the planetary-vortex projections are (0, $2\Omega_y$, $2\Omega_z$); and the absolute-vortex projections are (0, $2\Omega_y + \kappa\omega$, $2\Omega_z + 2\omega$).

From the compatibility requirements for Eqs. (3), there follows the condition for the tangent κ of the inclination angle (with respect to the vertical line) of the rotation centerline, which should satisfy the relationship

$$\kappa = \frac{2\Omega_y}{2\Omega_z + \omega}. \tag{4}$$

It is worth noting that the parameter κ, introduced as a characteristic of the locus for centers of circular cross sections, is closely related to the absolute-vortex vector; namely, the tangent of the inclination angle of the absolute-vortex vector to the local vertical line is exactly equal to κ.

Integrating the set of Eqs. (3) by making use of the boundary condition $p_r = p_f = 0$ at the free boundary, as well as of the condition for the equality of pressures at the flooded part of the interface between the ring water masses and the background

$$\begin{gathered}p_r = p_f(z_b) = \rho_r g(H - z_b) + \frac{d\rho_f}{dz} g\frac{H^2 - z_b^2}{2},\\ \rho_f = \rho_r + \left.\frac{d\rho_f}{dz}\right|_{z=0} z\end{gathered} \tag{5}$$

we arrive at the equation for the ring perturbed free surface:

$$\begin{gathered}\frac{\rho_r\omega}{2}(\omega + 2\Omega_z)(x_u^2 + y_u^2 - R^2) + \rho_r\omega\frac{2\Omega_y^2}{\omega + 2\Omega_z}z_u^2\\ - 2\Omega_y\rho_r\omega y_u z_u - \rho_r g(z_u - H) = 0\end{gathered} \tag{6}$$

and at the equation for the water-mass interface:

$$\frac{\omega}{2}(\omega + 2\Omega_z)(x_b^2 + y_b^2) + \left(\omega\frac{2\Omega_y^2}{2\Omega_z + \omega} - \frac{1}{2}N^2\right)z_b^2$$

$$- 2\Omega_y\omega y_b z_b = -\frac{\Delta}{\rho_r}, \qquad (7)$$

$$\Delta = 0.5\rho_r[N^2H^2 - \omega(\omega + 2\Omega_z)R^2],$$

$$N^2 = -\frac{d\rho_f}{dz}\frac{g}{\rho_r}.$$

Here, ρ_f and p_f are the density and pressure in the linearly stratified background; ρ_r and p_r are the density and pressure in the ring; $z = H$ is the equation for the unperturbed ocean surface; x_u, y_u, and z_u are the coordinates of the ring perturbed surface (zero isobar); x_b, y_b, and z_b are the coordinates of points on the separation surface; R is the ring radius on the ocean surface; and N is the Brunt–Vãisãlã frequency. For a stably stratified ocean, $\frac{d\rho_f}{dz} < 0$.

Analysis of the quadratic-form invariants shows that, in the case of $\omega \neq 0$, the surface described by relationship (6) is the elliptic paraboloid.

There exist three possibilities for the paraboloid positions:

(i) The case $\omega < 0$, $\omega + 2\Omega_z > 0$ corresponds to a weak ($|\omega| < 2\Omega_z$) anticyclone. In this case, $z_u > H$; i.e., points of the perturbed free boundary are located higher than the unperturbed ocean surface (elevation).

(ii) The case $\omega < 0$, $\omega + 2\Omega_z < 0$ corresponds to a strong ($|\omega| > 2\Omega_z$) anticyclone. In this case, $z_u < H$; i.e., points of the perturbed free boundary are located lower than the unperturbed ocean surface (funnel).

(iii) The case $\omega > 0$ corresponds to a cyclone. In this case, $z_u < H$; i.e., points of the perturbed free boundary are located lower than the unperturbed ocean surface (funnel).

The quantity $\frac{\omega}{2g}(\omega + 2\Omega_z)R^2$ determines the funnel depth or the elevation height. It is found for rings that the values $R \sim 50$–100 km and circumferential velocities $v \sim 1$ m s^{-1} are such that $\omega \sim 2 \times 10^{-5}$ s^{-1}. At latitudes of about 35°, at which the Gulf-Stream rings exist, $\Omega_z \sim 4 \times 10^{-5}$ s^{-1}. At the indicated values of the parameter, the funnel depth for cyclonic rings is ~25 cm, and the elevation height for anticyclonic rings is ~15 cm. The case separating strong and weak anticyclones corresponds to the condition $|\omega| = 2\Omega_z$. In this case, the circumferential velocity for characteristic sizes and latitudes of the ring locations would be $v_r \approx 2$ m s^{-1}. Apparently, strong anticyclonic rings are not observed in the ocean.

Observations based on artificial satellites with the application of altimeters measuring distances from a satellite to the ocean surface show that the anticyclonic rings have elevations on the order of 10 cm [6] and higher, whereas cyclonic rings have funnel depths of the same order of magnitude. There are data on the Internet (http://users.erols.com/gulfstrm/) according to which elevations and funnels attain heights of 50 cm and depths of 55 cm, respectively. Thus, the proposed ring model does explain these observation results.

The analysis of invariants of quadratic form (7) shows that for weak ($\omega < 0$, $|\omega| < 2\Omega_z$) anticyclonic rings, the water-mass interface is of the ellipsoidal shape.

For cyclonic rings ($\omega > 0$) under the condition

$$\left[1 - \frac{\omega(\omega + 2\Omega_z)}{N^2}\frac{R^2}{H^2}\right] > 0 \qquad (8)$$

and

$$\left[\frac{2\omega\Omega_y^2}{\omega + 2\Omega_z} + \frac{\omega(\omega + 2\Omega_z)}{2} - N^2\right] > 0$$

or

$$\left[\frac{2\omega\Omega_y^2}{\omega + 2\Omega_z} + \omega(\omega + 2\Omega_z) - N^2\right] < 0 \qquad (9)$$

the water-mass interface is the two-sheeted hyperboloid. At latitudes of $\varphi \approx 35°$, at which Gulf-Stream rings are present, and for real parameters of their formation and at their average depths of about 3×10^2 m (see [7]), the background parameters are the following: $\rho_f \sim 27$ arb. units; $\frac{d\rho}{dz} \sim 10^{-3}$ arb. units; $N^2 \sim 3.6 \times 10^{-4}$ s^{-2}; $\omega \sim 2 \times 10^{-5}$ s^{-1}; $\Omega_z \approx 4 \times 10^{-5}$ s^{-1}; and $R/H \sim 2.5 \times 10^{-2}$. In this case, condition (8) is fulfilled, and the second condition of (9) is surely fulfilled, insofar as the last term standing in brackets exceeds by three orders of magnitude the preceding terms.

When inequality (8) has the inverse sign, the surface has the shape of the one-sheeted hyperboloid, while at $H^2R^{-2} = \omega(\omega + 2\Omega_z)N^{-2}$, the surface separating the ring and background water masses is a cone.

We now roughly estimate the parameters of an atmospheric typhoon. The altitude of the troposphere in which typhoons propagate is close to 10 km; the density distribution over the altitude we may roughly consider to be a linear one; and $N \sim 10^{-2}$ s^{-1} [2, 8]. We also assume the pressure at the troposphere upper boundary to be zero. The circumferential velocities in a typhoon are of about 50 m s^{-1}, and $R \sim 100$ km. As a result, we obtain $\omega \sim 5 \times 10^{-4}$ s^{-1}, which exceeds by an order of

magnitude the frequency Ω_z. We take the density of the typhoon homogeneous core to be equal to the average density of the troposphere, which corresponds to an altitude of ~5 km, so that $H \sim 5$ km, and, thus, inequality (8) changes its sign. The second inequality of (9) is surely fulfilled. The analysis of the invariants testifies to the fact that the lateral boundary of the typhoon core is a one-sheeted hyperboloid. This corresponds to the schematic typhoon model developed in [8, 9]. At the latitude $\varphi \sim 25°$ and for the indicated typhoon parameters, the centerline of circular cross sections deviates in the meridian plane by an angle of about 13° from the vertical line.

For the ring-free boundary, we obtain the following canonical-form equation of the elliptic paraboloid in the variables x_u, y_u'', z_u'':

$$\frac{x_u^2}{a^2} + \frac{(y_u'')^2}{b^2} = \pm z_u'', \quad a^2 = \frac{2g\kappa}{|\omega|\Omega_y(1+\kappa^2)^{1/2}}, \qquad b^2 = \frac{g\kappa}{2|\omega|\Omega_y(1+\kappa^2)^{3/2}}. \tag{10}$$

The signs plus or minus are taken for cyclonic and anticyclonic rings, respectively.

The paraboloid axis is parallel to the straight line $y = kz$, the variables y_u'', z_u'' being linked with the variables y_u, z_u by the relationships

$$y_u = y_u'\cos\gamma - z_u'\sin\gamma, \quad z_u = y_u'\sin\gamma + z_u'\cos\gamma,$$

$$\tan\gamma = -\kappa, \quad y_u'' = y_u' + l, \quad z_u'' = z_u' + m,$$

$$l = -\frac{g\kappa^2}{2\omega\Omega_y(1+\kappa^2)^{3/2}}, \tag{11}$$

$$m = \frac{g\kappa^3}{4\omega\Omega_y(1+\kappa^2)^{3/2}} + H(1+\kappa^2)^{1/2} - \frac{R^2\omega\Omega_y(1+\kappa^2)^{1/2}}{g\kappa}.$$

The numerical estimates obtained for the above-indicated parameters yield $a \approx 120$ km, $b \approx 27$ km, $\kappa \approx 2$, $\arctan\kappa \approx 63°$ for the anticyclonic ring and $a \approx 110$ km, $b \approx 36$ km, $\kappa \approx 1.2$, $\arctan\kappa \approx 50°$ for the cyclonic ring.

Rotating the coordinate axes by the angle α, we can reduce the quadratic form standing in the left-hand side of relationship (7) to the canonical form:

$$\tan 2\alpha = \frac{2\kappa}{\kappa^2 - 1 - N^2\kappa(2\Omega_y\omega)^{-1}}. \tag{12}$$

The last term in the denominator of formula (12) exceeds the first two terms by five orders of magnitude since $4\Omega_y\omega \ll N^2$, and the angle α is small:

$$\alpha \approx -\frac{2\Omega_y\omega}{N^2}. \tag{13}$$

It is a rather complicated matter to express in the canonical form, in terms of defining parameters, the exact relationships for the coefficients standing at $(x_b)^2$, $(y_b')^2$, and $(z_b')^2$. Therefore, we make use of the fact that the angle α is small. Omitting cumbersome calculations, we present the equation for the separation surface in the principal axes with approximate coefficients [of the terms $R^2 - N^2H^2\kappa(2\Omega_y\omega)^{-1} \neq 0$]:

$$\frac{x_b^2 + (y_b')^2}{R^2 - N^2H^2\kappa(2\Omega_y\omega)^{-1}} + \frac{(z_b')^2}{H^2 - R^2 2\Omega_y\omega(N^2\kappa)^{-1}} = 1. \tag{14}$$

For the anticyclonic ring ($\omega < 0$), the exact equation of the separation surface is the equation for the three-axis ellipsoid, and approximate surface (14) is the ellipsoid of revolution whose principal axes are inclined at a small angle α in the meridian plane in such a manner that the Southern edge of the ellipsoid is flooded. For real ring parameters, $\alpha \approx 5''$.

For the cyclonic ring ($\omega > 0$), the exact equation of the separation surface is the equation for the three-axis hyperboloid, and approximate surface (14) is the hyperboloid of revolution with the principal axes inclined to the north in the meridian plane at a small angle α. For

$$\left[1 - N^2\left(\frac{H}{R}\right)^2\kappa(2\Omega_y\omega)^{-1}\right] < 0,$$

the hyperboloid is two-sheeted; for

$$\left[1 - N^2\left(\frac{H}{R}\right)^2\kappa(2\Omega_y\omega)^{-1}\right] > 0,$$

the hyperboloid is one-sheeted; and for

$$N^2\left(\frac{H}{R}\right)^2\kappa(2\Omega_y\omega)^{-1} = 1,$$

it is reduced to a cone with its apex coincided with the origin. For real parameters of cyclonic rings, usually, the first of the three inequalities holds, and the interface between the ring water and background water is the upper part of the two-sheeted hyperboloid (Fig. 2).

Thus, we have obtained a hydrodynamic solution to the problem of the equilibrium shape of a homogeneous rotating liquid mass in the stratified rotating ocean with a free boundary. In the framework of our formulation of the problem, this solution is exact, as the use of the con-

tinuity condition for pressures makes it possible to match two exact solutions for perfect liquids at the separation surface. This spatial solution is non-axisymmetric and discontinuous, because the density and the velocity tangent to the separation surface of the liquids have a break, which is quite admissible in the perfect-liquid model. The problem of the structure of the discontinuity surface requires additional analysis.

ACKNOWLEDGMENTS

This work was supported by the Russian Foundation for Basic Research, project nos. 04-01-00387 and 02-05-65150.

REFERENCES

1. *Oceanology. Physics of the Ocean*, Ed. by V. M. Kamenkovich and A. S. Monin (Nauka, Moscow, 1978) [in Russian].
2. A. S. Monin and G. M. Zhikharev, Usp. Fiz. Nauk **160**, 1 (1990) [Sov. Phys. Usp. **33**, 313 (1990)].
3. É. K. Lavrovskiĭ, I. P. Semenova, L. N. Slezkin, and V. V. Fominykh, Dokl. Akad. Nauk **375**, 42 (2000) [Dokl. Phys. **45**, 606 (2000)].
4. I. P. Semenova and L. N. Slezkin, Izv. Akad. Nauk, Mekh. Zhidk. Gaza, No. 5, 3 (2003).
5. P. Richardson, A. Strong, and J. Knauss, J. Phys. Oceanogr. **3**, 297 (1973).
6. K. A. Rogachev and L. V. Gogina, Priroda, No. 12, 36 (2001).
7. *Density Field of the Northern Part of the Atlantic Ocean*, Ed. by A. S. Monin and V. N. Stepanov (Gidrometeoizdat, Moscow, 1985) [in Russian].
8. A. Gill, *Atmosphere–Ocean Dynamics* (Academic, New York, 1982; Mir, Moscow, 1986).
9. E. Palmen and C. W. Newton, *Atmospheric Circulation Systems: Their Structure and Interpretation* (Academic, New York, 1969; Gidrometeoizdat, Leningrad, 1973).
10. É. S. Mamedov and N. I. Pavlov, *Typhoons* (Gidrometeoizdat, Leningrad, 1974) [in Russian].

Translated by G. Merzon